

IMPLEMENTATION OF DIFFERENT FLUX EVALUATION SCHEMES INTO A
TWO-DIMENSIONAL EULER SOLVER

A THESIS SUBMITTED TO
THE GRADUATE SCHOOL OF NATURAL AND APPLIED SCIENCES
OF
MIDDLE EAST TECHNICAL UNIVERSITY

BY

ELVAN ERASLAN

IN PARTIAL FULFILLMENT OF THE REQUIREMENTS
FOR
THE DEGREE OF MASTER OF SCIENCE
IN
MECHANICAL ENGINEERING

SEPTEMBER 2006

Approval of the Graduate School of Natural and Applied Sciences

Prof. Dr. Canan ÖZGEN
Director

I certify that this thesis satisfies all the requirements as a thesis for the degree of Master of Science.

Prof. Dr. Kemal İDER
Head of Department

This is to certify that we have read this thesis and that in our opinion it is fully adequate, in scope and quality, as a thesis for the degree of Master of Science.

Prof. Dr. Haluk AKSEL
Supervisor

Examining Committee Members

Prof. Dr. Zafer DURSUNKAYA	(METU, ME)	_____
Prof. Dr. M. Haluk AKSEL	(METU, ME)	_____
Asst. Prof. Dr. Cüneyt SERT	(METU, ME)	_____
Instructor Dr. Tahsin ÇETİNKAYA	(METU, ME)	_____
Dr. Ali Ruhşen ÇETE	(TURBOTEK)	_____

I hereby declare that all information in this document has been obtained and presented in accordance with academic rules and ethical conduct. I also declare that, as required by these rules and conduct, I have fully cited and referenced all material and results that are not original to this work.

Elvan ERASLAN

ABSTRACT

IMPLEMENTATION OF DIFFERENT FLUX EVALUATION SCHEMES INTO A TWO-DIMENSIONAL EULER SOLVER

ERASLAN, Elvan

M.Sc., Department of Mechanical Engineering

Supervisor: Prof. Dr. M. Haluk AKSEL

September 2006, 139 pages

This study investigates the accuracy and efficiency of several flux splitting methods for the compressible, two-dimensional Euler equations. Steger-Warming flux vector splitting method, Van Leer flux vector splitting method, The Advection Upstream Splitting Method (AUSM), Artificially Upstream Flux Vector Splitting Scheme (AUFS) and Roe's flux difference splitting schemes were implemented using the first- and second-order reconstruction methods. Limiter functions were embedded to the second-order reconstruction methods. The flux splitting methods are applied to subsonic, transonic and supersonic flows over NACA0012 airfoil, as well as subsonic, transonic and supersonic flows in a channel. The comparison of the obtained results with each other and the ones in the literature is presented. The advantages and disadvantages of each scheme among others are identified.

Keywords: Two-dimensional Euler Equations, Flux Splitting Schemes, Reconstruction Methods, Limiter Functions

ÖZ

İKİ BOYUTLU EULER ÇÖZÜCÜSÜNE DEĞİŞİK AKI HESAPLAMA YÖNTEMLERİNİN EKLENMESİ

ERASLAN, Elvan

Yüksek Lisans, Makina Mühendisliği Bölümü

Tez Yöneticisi: Prof. Dr. M. Haluk AKSEL

Eylül 2006, 139 sayfa

Bu çalışmada sıkıştırılabilir, iki boyutlu Euler denklemleri için, akı ayrıştırma yöntemleri hassasiyet ve verimlilik açısından incelenmiştir. Birinci ve ikinci dereceden yeniden yapılandırma yöntemleri kullanılarak Steger-Warming akı vektörü ayrıklaştırma yöntemi, Van Leer akı vektörü ayrıklaştırma yöntemi, yukarı iletimli ayrıştırma yöntemi (AUSM), ileri yönlü yapay akı vektörü ayrıştırma yöntemi (AUFS) ve Roe akı farkı ayrıklaştırma yöntemi uygulanmıştır. İkinci dereceden yeniden yapılandırma yöntemlerine sınırlayıcı fonksiyonlar eklenmiştir. Akı ayrıştırma yöntemleri ses-altı, ses seviyesi ve ses-üstü hızlarda NACA0012 kanat etrafında ve ses-altı, ses seviyesi ve ses-üstü hızlarda kanal içinde denenmiştir. Elde edilen sonuçlar birbirleriyle ve literatürdeki sonuçlarla karşılaştırılmıştır. Kullanılan yöntemlerin birbirlerine göre avantaj ve dezavantajları incelenmiştir.

Anahtar Kelimeler: İki-boyutlu Euler Denklemleri, Akı Ayrıştırma Yöntemleri, Yeniden Yapılandırma Yöntemleri, Sınırlayıcı Fonksiyonlar

To my family

To Sertel KONALI

ACKNOWLEDGEMENTS

I would like to thank my thesis supervisor Prof. Dr. M. Haluk AKSEL for his understanding, support and guidance throughout this study.

I also want to thank Tahsin Çağrı ŞIŞMAN and Enver Doruk ÖZDEMİR for sharing their code and providing a starting point for my thesis. Moreover, they warned me for the possible difficulties that may arise during the implementation of the code and in the development period of my thesis. They shared their experiences for overcoming these problems. This guidance of theirs helped me greatly in my study.

With his suggestions, Onur BAŞ showed me a way to find a solution where I got stuck.

I offer my sincere appreciation to my friend, Emre GÜRDAMAR who supported me with his enthusiasm.

My special thanks are for Sertel KONALI, the one with the greatest share in my life. He has always encouraged me to keep on, no matter what the problem was. His presence helped me to cope with the difficulties here and everywhere. Without him, this work couldn't be completed and life would be unbearable.

Last, but of course not the least, I would like to thank my ever-loving parents and sister. Elif has been much more than a sister for my entire life with whom I shared everything. My parents' attitude towards us helped us to become individuals who follow their dreams and wills with great enthusiasm. My family has always been there for me in times of trouble and weakness as well as moments of pleasure.

TABLE OF CONTENTS

PLAGIARISM.....	iii
ABSTRACT	iv
ÖZ	v
DEDICATION	vi
ACKNOWLEDGEMENTS.....	vii
TABLE OF CONTENTS	viii
LIST OF TABLES	xii
LIST OF FIGURES	xiii
LIST OF SYMBOLS.....	xxiii
CHAPTERS	
1 INTRODUCTION	1
1.1 General	1
1.2 Computational Fluid Dynamics	1
1.2.1 Pre-processor	2
1.2.2 Solver.....	2
1.2.3 Post-processor.....	12
1.3 Present Study	13
2 GOVERNING EQUATIONS.....	15
2.1 Conservation Law	15
2.1.1 General Conservation Law	15
2.1.2 Conservation of Mass	18

2.1.3	Conservation of Momentum	19
2.1.4	Conservation of Energy	20
2.2	Complete System of the Euler Equations	22
3	PRINCIPLES OF SOLUTION	26
3.1	Euler Equations	27
3.2	Spatial Discretisation	29
3.2.1	Physical Space	30
3.2.2	Geometrical Quantities	32
3.3	Temporal Discretisation	33
3.4	Initial Conditions	36
3.5	Boundary Conditions	36
3.5.1	Farfield Boundary Condition	37
3.5.2	Solid Wall Boundary Condition	37
4	FLUX EVALUATION SCHEMES	38
4.1	The Quasi-Linear Formulation of the Euler Equations.....	39
4.1.1	The Jacobian Matrices.....	39
4.1.2	Eigenvalues of Euler Equations.....	43
4.2	Upwind Schemes.....	44
4.2.1	Flux Vector Splitting.....	45
4.2.1.1	Steger-Warming Flux Vector Splitting.....	45
4.2.1.2	Van-Leer Flux Vector Splitting	50
4.2.1.3	Advection Upstream Splitting Method (AUSM)	53
4.2.1.4	Artificially Upstream Flux Vector Splitting Scheme (AUFS)	56
4.2.2	Flux Difference Splitting.....	60

4.2.2.1	Riemann Problem or Shock Tube Problem.....	61
4.2.2.2	Godunov Approach	63
4.2.2.3	Roe's Approximate Solver.....	64
4.3	Solution Reconstruction	68
4.4	Limiters	72
5	RESULTS AND DISCUSSION	74
5.1	External Flow	75
5.1.1	First Order Calculations	75
5.1.1.1	Subsonic Flow.....	75
5.1.1.2	Transonic Flow.....	81
5.1.1.3	Supersonic Flow.....	85
5.1.2	Second order calculations.....	90
5.1.2.1	Second order calculations without a limiter function	90
5.1.2.1.1	Subsonic Flow	90
5.1.2.1.2	Transonic Flow	95
5.1.2.1.3	Supersonic Flow.....	102
5.1.2.2	Second order calculations with a limiter function	106
5.1.2.2.1	Subsonic flow	106
5.1.2.2.2	Transonic Flow	107
5.1.2.2.3	Supersonic Flow.....	109
5.2	Internal Flow	112
5.2.1	First-order Calculations.....	113
5.2.1.1	Subsonic Flow.....	113
5.2.1.2	Transonic Flow.....	116

5.2.1.3	Supersonic Flow.....	119
5.2.2	Second-order Calculations.....	122
5.2.2.1	Second-order calculations without a limiter function.....	122
5.2.2.1.1	Subsonic Flow.....	122
5.2.2.1.2	Transonic Flow.....	123
5.2.2.1.3	Supersonic Flow.....	124
5.2.2.2	Second-order calculations with a limiter function.....	125
5.2.2.2.1	Subsonic Flow.....	125
5.2.2.2.2	Transonic Flow.....	126
5.2.2.2.3	Supersonic Flow.....	127
6	CONCLUSION.....	129
	REFERENCES.....	131
	APPENDIX	
	A. CALCULATION OF RESIDUALS.....	138

LIST OF TABLES

Table 5.1: Maximum Allowable CFL number for $M_\infty = 0.6$ $\alpha = 0^\circ$	81
---	----

LIST OF FIGURES

Figure 3.1: Control volume in a 2-D space	30
Figure 3.2: Body-fitted structured grid	31
Figure 3.3: Mesh structure of control volume (I, J)	31
Figure 4.1: Shock Tube	62
Figure 4.2: Piecewise constant distribution	64
Figure 4.3: Exact solution of Riemann problem at cell interfaces	64
Figure 4.4: Typical face and cell-center within a body-fitted structured grid	71
Figure 5.1: 129x65 O-grid over NACA0012 airfoil	75
Figure 5.2: Detailed view of 129x65 O-grid over NACA0012 airfoil	76
Figure 5.3: 97x65 O-grid over NACA0012 airfoil	76
Figure 5.4: Detailed view of 97x65 O-grid over NACA0012 airfoil	77
Figure 5.5: Distribution of pressure coefficient over NACA0012 airfoil at $M_\infty = 0.6 \alpha = 0^\circ$ using 97x65 O-grid with first-order reconstruction	78
Figure 5.6: Distribution of pressure coefficient over NACA0012 airfoil at $M_\infty = 0.6 \alpha = 0^\circ$ using 129x65 O-grid with first-order reconstruction	79
Figure 5.7: Convergence history of Steger-Warming FVS Scheme for first-order subsonic flow using 129x65 O-grid	80

Figure 5.8: Convergence history of Van Leer FVS Scheme for first-order subsonic flow using 129x65 O-grid	80
Figure 5.9: Convergence history of AUFS for first-order subsonic flow using 129x65 O-grid	80
Figure 5.10: Convergence history of AUSM for first-order subsonic flow using 129x65 O-grid	80
Figure 5.11: Convergence history of Roe's FDS Scheme for first-order subsonic flow using 129x65 O-grid	81
Figure 5.12: 185x60 O-grid over NACA0012 airfoil for $M_\infty = 0.8 \alpha = 0^\circ$ flow	82
Figure 5.13: Detailed view of 185x60 O-grid over NACA0012 airfoil for $M_\infty = 0.8 \alpha = 0^\circ$ flow	83
Figure 5.14: Distribution of pressure coefficient over NACA0012 airfoil at $M_\infty = 0.8 \alpha = 0^\circ$ using 185x60 O-grid with first-order reconstruction	83
Figure 5.15: Convergence history of Steger-Warming FVS Scheme for first-order transonic flow using 185x60 O-grid	84
Figure 5.16: Convergence history of Van Leer FVS Scheme for first-order transonic flow using 185x60 O-grid	84
Figure 5.17: Convergence history of AUFS for first-order transonic flow using 185x60 O-grid	84
Figure 5.18: Convergence history of AUSM for first-order transonic flow using 185x60 O-grid	84
Figure 5.19: Convergence history of Roe's FDS Scheme for first-order transonic flow using 185x60 O-grid	85

Figure 5.20: Pressure contours around NACA0012 at $M_\infty = 1.2 \alpha = 0^\circ$ by AUSM [22]	86
Figure 5.21: Pressure contours around NACA0012 at $M_\infty = 1.2 \alpha = 0^\circ$ by Steger-Warming FVS Scheme using 129x65 O-grid with first-order reconstruction	86
Figure 5.22: Pressure contours around NACA0012 at $M_\infty = 1.2 \alpha = 0^\circ$ by Van Leer FVS Scheme using 129x65 O-grid with first-order reconstruction	87
Figure 5.23: Pressure contours around NACA0012 at $M_\infty = 1.2 \alpha = 0^\circ$ by AUSM using 129x65 O-grid with first-order reconstruction	87
Figure 5.24: Pressure contours around NACA0012 at $M_\infty = 1.2 \alpha = 0^\circ$ by AUFS using 129x65 O-grid with first-order reconstruction.	88
Figure 5.25: Pressure contours around NACA0012 at $M_\infty = 1.2 \alpha = 0^\circ$ by Roe's FDS Scheme using 129x65 O-grid with first-order reconstruction	88
Figure 5.26: Convergence history of Steger-Warming FVS Scheme for first-order supersonic flow using 129x65 O-grid	89
Figure 5.27: Convergence history of Van Leer FVS Scheme for first-order supersonic flow using 129x65 O-grid	89
Figure 5.28: Convergence history of AUFS for first-order supersonic flow using 129x65 O-grid	89
Figure 5.29: Convergence history of AUSM for first-order supersonic flow using 129x65 O-grid	89
Figure 5.30: Convergence history of Roe's FDS Scheme for first-order supersonic flow using 129x65 O-grid	90
Figure 5.31: Distribution of pressure coefficient over NACA0012 airfoil at	

$M_\infty = 0.63 \alpha = 2^\circ$ using Steger-Warming FVS Scheme with second-order reconstruction by 129x65 O-grid	91
Figure 5.32: Distribution of pressure coefficient over NACA0012 airfoil at $M_\infty = 0.63 \alpha = 2^\circ$ using Van Leer FVS Scheme with second-order reconstruction by 129x65 O-grid	91
Figure 5.33: Distribution of pressure coefficient over NACA0012 airfoil at $M_\infty = 0.63 \alpha = 2^\circ$ using 129x65 O-grid with second-order reconstruction	92
Figure 5.34: Distribution of pressure coefficient over NACA0012 airfoil at $M_\infty = 0.6 \alpha = 0^\circ$ using 129x65 O-grid with second-order reconstruction	93
Figure 5.35: Convergence history of Steger-Warming FVS Scheme for second-order subsonic flow using 129x65 O-grid	94
Figure 5.36: Convergence history of Van Leer FVS Scheme for second-order subsonic flow using 129x65 O-grid	94
Figure 5.37: Convergence history of AUFS for second-order subsonic flow using 129x65 O-grid	94
Figure 5.38: Convergence history of AUSM for second-order subsonic flow using 129x65 O-grid	94
Figure 5.39: Convergence history of Roe's FDS Scheme for second-order subsonic flow using 129x65 O-grid	95
Figure 5.40: Distribution of pressure coefficient over NACA0012 airfoil at $M_\infty = 0.85 \alpha = 1^\circ$ using AUSM with second-order reconstruction by 97x65 O-grid.....	96
Figure 5.41: Distribution of pressure coefficient over NACA0012 airfoil at $M_\infty = 0.85 \alpha = 1^\circ$ using AUSM with second-order reconstruction by 257x65	

O-grid.....	97
Figure 5.42: Distribution of pressure coefficient over NACA0012 airfoil at $M_\infty = 0.85 \alpha = 1^\circ$ using Roe's FDS Scheme with second-order reconstruction by 257x65 O-grid	98
Figure 5.43: Distribution of pressure coefficient over NACA0012 airfoil at $M_\infty = 0.85 \alpha = 1^\circ$ using Roe's FDS Scheme with second-order reconstruction by 317x60 shock-adapted O-grid	98
Figure 5.44: Distribution of pressure coefficient over NACA0012 airfoil at $M_\infty = 0.85 \alpha = 1^\circ$ using Roe's FDS Scheme with second-order reconstruction by 513x65 O-grid	99
Figure 5.45: Distribution of pressure coefficient over NACA0012 airfoil at $M_\infty = 0.8 \alpha = 1.25^\circ$ using Steger-Warming FVS Scheme with second-order reconstruction by 257x65 O-grid	100
Figure 5.46: Distribution of pressure coefficient over NACA0012 airfoil at $M_\infty = 0.8 \alpha = 1.25^\circ$ using Van Leer FVS Scheme with second-order reconstruction by 257x65 O-grid	100
Figure 5.47: Distribution of pressure coefficient over NACA0012 airfoil at $M_\infty = 0.8 \alpha = 0^\circ$ using 185x60 shock-adapted O-grid with second-order reconstruction	101
Figure 5.48: Distribution of pressure coefficient over NACA0012 airfoil at $M_\infty = 1.2 \alpha = 0^\circ$ using 129x65 O-grid with second-order reconstruction	103
Figure 5.49: Pressure contours around NACA0012 at $M_\infty = 1.2 \alpha = 0^\circ$ by AUSM [22]	103

Figure 5.50: Pressure contours around NACA0012 at $M_\infty = 1.2 \alpha = 0^\circ$ by Steger-Warming FVS Scheme using 129x65 O-grid with second-order reconstruction.....	104
Figure 5.51: Pressure contours around NACA0012 at $M_\infty = 1.2 \alpha = 0^\circ$ by Van Leer FVS Scheme using 129x65 O-grid with second-order reconstruction	104
Figure 5.52: Pressure contours around NACA0012 at $M_\infty = 1.2 \alpha = 0^\circ$ by Roe's FDS Scheme using 129x65 O-grid with second-order reconstruction	105
Figure 5.53: Pressure contours around NACA0012 at $M_\infty = 1.2 \alpha = 0^\circ$ by AUSM using 129x65 O-grid with second-order reconstruction	105
Figure 5.54: Pressure contours around NACA0012 at $M_\infty = 1.2 \alpha = 0^\circ$ by AUFS using 129x65 O-grid with second-order reconstruction	106
Figure 5.55: Distribution of pressure coefficient over NACA0012 airfoil at $M_\infty = 0.6 \alpha = 0^\circ$ using 129x65 O-grid with second-order reconstruction with limiter function	107
Figure 5.56: Distribution of pressure coefficient over NACA0012 airfoil at $M_\infty = 0.8 \alpha = 0^\circ$ using 185x60 shock-adapted O-grid with second-order reconstruction with limiter function	108
Figure 5.57: Pressure contours around NACA0012 at $M_\infty = 1.2 \alpha = 0^\circ$ by AUSM [22]	109
Figure 5.58: Pressure contours around NACA0012 at $M_\infty = 1.2 \alpha = 0^\circ$ by Steger-Warming FVS Scheme using 129x65 O-grid with second-order reconstruction with limiter function	110
Figure 5.59: Pressure contours around NACA0012 at $M_\infty = 1.2 \alpha = 0^\circ$ by Van	

Leer FVS Scheme using 129x65 O-grid with second-order reconstruction with limiter function	110
Figure 5.60: Pressure contours around NACA0012 at $M_\infty = 1.2 \alpha = 0^\circ$ by Roe's FDS Scheme using 129x65 O-grid with second-order reconstruction with limiter function	111
Figure 5.61: Pressure contours around NACA0012 at $M_\infty = 1.2 \alpha = 0^\circ$ by AUSM using 129x65 O-grid with second-order reconstruction with limiter function	111
Figure 5.62: Pressure contours around NACA0012 at $M_\infty = 1.2 \alpha = 0^\circ$ by AUFS using 129x65 O-grid with second-order reconstruction with limiter function	112
Figure 5.63: 129x33 grid for a channel having a circular arc	113
Figure 5.64: Mach contours in the channel having a circular bump at $M_\infty = 0.5 \alpha = 0^\circ$ by Ni [60]	114
Figure 5.65: Mach contours in the channel having a circular bump at $M_\infty = 0.5 \alpha = 0^\circ$ obtained by Steger-Warming flux vector splitting scheme using first-order reconstruction	114
Figure 5.66: Mach contours in the channel having a circular bump at $M_\infty = 0.5 \alpha = 0^\circ$ obtained by Van Leer flux vector splitting scheme using first-order reconstruction	114
Figure 5.67: Mach contours in the channel having a circular bump at $M_\infty = 0.5 \alpha = 0^\circ$ obtained by Roe's flux difference splitting scheme using first-order reconstruction	115
Figure 5.68: Mach contours in the channel having a circular bump at $M_\infty = 0.5 \alpha = 0^\circ$ obtained by AUSM using first-order reconstruction	115
Figure 5.69: Mach contours in the channel having a circular bump at	

$M_\infty = 0.5 \alpha = 0^\circ$ obtained by AUFS using first-order reconstruction	115
5.70: Distribution of Mach number in the channel having a circular bump at $M_\infty = 0.5$ using first-order reconstruction	116
Figure 5.71: Mach contours in the channel having a circular bump at $M_\infty = 0.675 \alpha = 0^\circ$ by Ni [60]	117
Figure 5.72: Mach contours in the channel having a circular bump at $M_\infty = 0.675 \alpha = 0^\circ$ obtained by Steger-Warming flux vector splitting scheme using first-order reconstruction	117
Figure 5.73: Mach contours in the channel having a circular bump at $M_\infty = 0.675 \alpha = 0^\circ$ obtained by Van Leer flux vector splitting scheme using first-order reconstruction	117
Figure 5.74: Mach contours in the channel having a circular bump at $M_\infty = 0.675 \alpha = 0^\circ$ obtained by Roe's flux difference splitting scheme using first-order reconstruction	118
Figure 5.75: Mach contours in the channel having a circular bump at $M_\infty = 0.675 \alpha = 0^\circ$ obtained by AUSM using first-order reconstruction	118
Figure 5.76: Mach contours in the channel having a circular bump at $M_\infty = 0.675 \alpha = 0^\circ$ obtained by AUFS using first-order reconstruction	118
Figure 5.77: Distribution of Mach number in the channel having a circular bump at $M_\infty = 0.675 \alpha = 0^\circ$ using first-order reconstruction	119
Figure 5.78: Mach contours in the channel having a circular bump at $M_\infty = 1.4 \alpha = 0^\circ$ by Ni [60]	120

Figure 5.79: Mach contours in the channel having a circular bump at $M_\infty = 1.4 \alpha = 0^\circ$ obtained by Steger-Warming flux vector splitting scheme using first-order reconstruction	120
Figure 5.80: Mach contours in the channel having a circular bump at $M_\infty = 1.4 \alpha = 0^\circ$ obtained by Van Leer flux vector splitting scheme using first-order reconstruction	120
Figure 5.81: Mach contours in the channel having a circular bump at $M_\infty = 1.4 \alpha = 0^\circ$ obtained by Roe's flux difference splitting scheme using first-order reconstruction	121
Figure 5.82: Mach contours in the channel having a circular bump at $M_\infty = 1.4 \alpha = 0^\circ$ obtained by AUSM using first-order reconstruction	121
Figure 5.83: Mach contours in the channel having a circular bump at $M_\infty = 1.4 \alpha = 0^\circ$ obtained by AUFS using first-order reconstruction	121
Figure 5.84: Distribution of Mach number in the channel having a circular bump at $M_\infty = 1.4 \alpha = 0^\circ$ using first-order reconstruction	122
Figure 5.85: Distribution of Mach number in the channel having a circular bump at $M_\infty = 0.5 \alpha = 0^\circ$ obtained using second-order reconstruction without a limiter function	123
Figure 5.86: Distribution of Mach number in the channel having a circular bump at $M_\infty = 0.675 \alpha = 0^\circ$ obtained using second-order reconstruction without a limiter function	124
Figure 5.87: Distribution of Mach number in the channel having a circular bump at $M_\infty = 1.4 \alpha = 0^\circ$ obtained using second-order reconstruction without a limiter function	125

Figure 5.88: Distribution of Mach number in the channel having a circular bump at $M_\infty = 0.5$ $\alpha = 0^\circ$ obtained using second-order reconstruction with a limiter function.....126

Figure 5.89: Distribution of Mach number in the channel having a circular bump at $M_\infty = 0.675$ $\alpha = 0^\circ$ obtained using second-order reconstruction with a limiter function.....127

Figure 5.90: Distribution of Mach number in the channel having a circular bump at $M_\infty = 1.4$ $\alpha = 0^\circ$ obtained using second-order reconstruction with a limiter function.....128

LIST OF SYMBOLS

A	Jacobian of flux function in x -direction
a	Jacobian of flux function
B	Jacobian of flux function in y -direction
c	speed of sound
c_p	Specific heat coefficient under constant pressure
c_v	Specific heat coefficient under constant volume
E	Total energy per unit mass
e	Internal energy per unit mass
\vec{f}	Flux vector in x -direction
\vec{f}_b	Body force per unit mass
\vec{f}_c	Convective part of flux vector in x -direction
\vec{f}_p	Pressure part of flux vector in x -direction
\vec{F}	Flux vector
\vec{F}_c	Convective flux vector
\vec{F}_d	Diffusive flux vector
$\vec{\vec{F}}_c$	Convective flux tensor
$\vec{\vec{F}}_d$	Diffusive flux tensor
\vec{g}	Flux vector in y -direction
H	Total enthalpy per unit mass

$\vec{\vec{I}}$	Identity tensor
k	Thermal conductivity coefficient
M	Mach number
\vec{n}	Normal vector
p	Pressure
p_o	Stagnation pressure
q_h	Heat sources other than conduction
Q	Scalar quantity
\vec{Q}	Vector quantity
Q_v	Volume sources
\vec{Q}_s	Vector of surface sources
\vec{Q}_{sc}	Vector of sources
$\vec{\vec{Q}}_s$	Tensor of surface sources
\vec{Q}_v	Vector of volume sources
\vec{r}	Direction vector
R	Universal gas constant per unit mass
\vec{R}	Residual term
\overrightarrow{RR}	Ratio of residuals
s_1, s_2	Artificial wave speeds
ΔS	Length of a face
S	Surface
\vec{S}	Surface vector

Δt	Time step
T	Absolute temperature
T_o	Stagnation temperature
\bar{U}	Contravariant velocity vector
\bar{V}	Velocity vector
x, y, z	Cartesian coordinates

Greek Letters

α	Stage coefficient
κ	thermal diffusivity constant
γ	Ratio of specific heats
ρ	Density
Ω	Volume
$\overset{=}{\sigma}$	Stress tensor
$\overset{=}{\tau}$	Shear stress tensor
Ψ	Limiter function

Subscripts

k	Individual faces of the control volume
I, J	Cell center locations in x, y directions
i, j	Nodal point locations in x, y directions
L	Left of a face
R	Right of a face

Superscripts

n Time level

Symbols

\otimes Tensor product of two vectors

CHAPTER 1

INTRODUCTION

1.1 General

In science, there exist three distinct ways to obtain information about physical phenomena. First of them is the analytical method which involves the solution of the governing partial differential equations that describes the physical phenomena. The advantage of this method is that if these equations can be solved, they give the exact behaviour of the phenomena. The drawback is, however, these equations are very cumbersome and even impossible to solve since most of the time they contain non-linear terms. The second method to explain the physical phenomena is to perform experiments. When properly conducted, these experiments can give very good results despite the small disturbances that occur during the data acquisition session. On the other hand, these experiments can be very costly or even impossible to perform. Moreover, some of these experiments shall not be feasible to perform. The last tool to examine physical phenomena is the computational method, which involves computers to simulate the phenomena and provide the desired information. Nevertheless, the advantage of being simple is confronted by the need of a powerful system in order to analyze complex situations. However, with the developments in the computer technology, they are used widely by scientists and engineers.

1.2 Computational Fluid Dynamics

In fluid mechanics, the area in which computers are used to simulate the problems is called Computational Fluid Dynamics (CFD). As Malalasekera [1]

stated, “*CFD is the analysis of systems involving fluid flow, heat transfer and associated phenomena such as chemical reactions by means of computer based simulation*”. A CFD code is made up of three main elements which are (i) pre-processor, (ii) solver and (iii) post-processor.

1.2.1 Pre-processor

The procedure of solving the problem starts with the definition of the computational domain. After this step, the computational domain is divided into a number of sub-domains which are known as a grid or mesh. Then, the fluid properties are defined. Finally, the appropriate boundary conditions at cells which coincide with or touch the domain boundary are specified at pre-processing step. [1]

1.2.2 Solver

There exist four different techniques for numerical solution of partial differential equations: finite difference method, finite element method, spectral methods and finite volume method. This latter technique is firstly developed as a special finite difference formulation, but being more physically based, this method distinguished among the other techniques.

Finite difference method (FDM) is based on expanding the derivatives in partial differential equations. There are two approaches to calculate the derivatives of the functions. First one is to use Taylor series approximations. An alternative approach for this method is to use polynomials of degree n to expand functions. [2] In Taylor series approximation approach; there exist three schemes to calculate the derivatives. The first one is the forward differentiation, which uses the point under consideration and succeeding points to calculate derivative at any point. The next scheme is backward differentiation method, which calculates the derivative of the function using the desired point and previous points. The last scheme is the central differentiation method, which uses the previous and succeeding points both, to calculate the value of derivative at any point. In Taylor

series approach, the generated error is due to the truncation of higher order terms. Although this method is easy to apply, it requires a highly regular grid, hence limiting the application of the formulation to simple geometries. [3, 4]

The second formulation technique is the finite element method (FEM). It was initially developed for structural stress analysis, however during the last two or three decades this technique is extended to several other disciplines. [1, 2] The advantage of this system over FDM is that it can be applied with the use of unstructured grids, i.e. with complex geometries. The idea behind this technique is that it develops local element equations on each element. Then, the technique minimizes the errors of the solution based on an optimization technique. Lastly, all the element equations are combined to form a system of linear algebraic equations [2].

Spectral methods (SM) are based on the idea to approximate the unknowns by using truncated Fourier series or series of Chebyshev polynomials. The approximations are valid throughout the computational domain. [1]

Finite volume method (FVM) originated from FDM. FVM uses the conservative form of the conservation equations. In this discretisation technique, the conservation statement of the property Φ is applied in a form that is applicable to a region in space. This enables the formal integration of the governing equations of the flow over all the control volumes of the computational domain [1-5]. The above statement provides that the independent values are integrated directly on the physical domain. Thus, the domain needs only to be discretised successfully, i.e. structured grids are not mandatory. Once the unknowns in each control volume are obtained by an initial condition, the equations are solved iteratively to obtain the final result. Although, it is difficult to implement second and higher order methods in three-dimensional domains, it gained much popularity among engineers. This is due to the physical basis of the terms that are approximated. [4]

Finite volume method is used in this study in order to solve the conservation equations. Once the surface and volume integrals in the conservative form of the

equations are approximated by using suitable quadrature formulas, differential equations in time and space are obtained. The conservative variables appear as unknowns in these equations. Time derivative of these unknowns are approximated by temporal discretisation methods, and the space derivatives are approximated by spatial discretisation methods. Applying separate discretisation in space and time is named as method of lines. Handling the space and time terms separately allows approximating the corresponding terms at different levels. The above procedure is repeated for the whole domain and by iteration the steady-state result is obtained. The solution domain consists of cells formed by the grids and there are mainly two types of grids [3, 6].

The grid cells in structured grids are quadrilaterals in 2-D and hexahedra in 3-D and are ordered as the name implies. The nodes or the cell centres are uniquely defined by the indices i, j, k in an order. The neighbor of the cell (i, j, k) in the x -direction is the cell indicated by $(i+1, j, k)$. The structured grids can be formed by following the geometry contour and it is named as the body-fitted (curvilinear) grid. On the other hand, the grid can be formed in the Cartesian coordinates without taking care of the geometry in the domain. If the grid is formed in such a manner then it is named as the Cartesian grid. The second type of the grids is the unstructured grids. Unstructured grids usually consist of a mixture of quadrilaterals and triangles in 2D and of hexahedra, tetrahedra, prisms and pyramids in 3D. They are not ordered and the definition of the neighbor cells in unstructured grids is little more complicated than that in the structured grids. Although implementation of the solver is rather easy in structured grids, the unstructured grids are preferred for complex geometries for more accurate results. In simple geometries such as single element airfoils, structured grids are used, whereas the domain with a multi-element airfoil is meshed by unstructured grids [3, 6].

Temporal discretisation methods are distinguished into two; explicit and implicit methods. When a direct computation of the dependent variables can be made in terms of known quantities, the computation is said to be explicit. Hence, explicit methods make use of the known data at the current time step in order to find the

unknown data at the next time step. The unknown conservative variables can be found by using a single-stage time-stepping; however this method is only applicable for first-order upwind schemes. On the other hand, the multistage time-stepping schemes, called Runge-Kutta schemes, introduced by Jameson et al. [7] are very popular since the solution is advanced in several stages. The obtained residuals are weighted by the specified coefficients. By changing the weight coefficients and expanding the number of stages, the order of temporal discretisation can be increased. Although the explicit multistage time-stepping schemes are very cheap and easy to implement, the drawback of this method is the restrictions of the permissible time step due to stability conditions. In this study, local time-stepping, which is based on the determination of the maximum permissible time step for each control volume, is used. In order to have a stable explicit time-stepping scheme, time step, should fulfill Courant-Friedrichs-Lewy (CFL) criteria. This condition is satisfied when the time step is equal to or smaller than time required for transforming information across the stencil. In this case, it is guaranteed that the associated error remains in the order of the truncation error [3]. In contrast to the explicit schemes, when the dependent variables are defined by coupled sets of equations and either a matrix or iterative technique is needed to obtain the solution, the numerical method is said to be implicit. The advantage of the implicit methods over the explicit methods is that, implicit methods do not limit time steps and which lead to a faster convergence [3, 6]. In this study, three-stage Runge-Kutta time-stepping scheme, one of the explicit time-stepping methods, is used.

The residual terms used in the temporal discretisation, are the differences obtained from the spatial discretisation. The spatial discretisation techniques are used to approximate the convective and viscous terms. There are varieties of spatial discretisation schemes in the literature, and researches still continue to find more accurate, robust and cheap schemes. These techniques actually apply for the convective terms, since the viscous terms are handled by central differencing due to their physical nature.

Schemes for handling the convective terms in the Euler equations are mainly

divided into two categories.

Before giving information about the discretisation schemes, it would be convenient to give broad information about the definition of control volumes and the storage points of the flow data. There exist three major methodologies of discretisation which are the cell-centered scheme, cell vertex scheme with overlapping control volumes and cell vertex scheme with dual control volumes. Cell-centered scheme, which is used in this study, uses the cells defined by the grid as control volumes. The flow variables are stored at the centroid of each control volume, whereas the cell-vertex schemes store the flow data at the vertices of each control volume as the name implies. Overlapping control volumes are the cells formed by the grid, just as in the case of cell-centered schemes, but the data obtained for a vertex is influenced by the neighboring cells. Dual control volumes are formed by connecting the midpoints of the cells surrounding a vertex. [6]

First one of the spatial discretisation schemes is the group of central difference schemes. The basic idea of the central scheme is finding the conservative variables at the face of a control volume, by arithmetically averaging the corresponding values at the left and right of the cell face. This may lead to odd-even decoupling of the solution, meaning that there may be more than one solution to an equation, and solution may overshoot at discontinuities. Numerical dissipation models are also included in the schemes in order to prevent these oscillations at shock waves, and to make the scheme more stable [8]. Although the central scheme is less accurate in handling the discontinuities, researchers have spent too much time on improving the basic scheme, because it is computationally cheaper. The central difference schemes are of mainly two types, the first type handles the space and time integration together, and the second type approximates the space and time integrals separately. The first of the former type was introduced by Lax in 1954 [9], which was a first order and explicit scheme. In 1960, Lax-Wendroff introduced a second-order, explicit scheme of the same kind [10]. Two-step explicit central difference schemes were presented by MacCormack [11], LeRat -Peyret [12], and an implicit scheme of this type was

presented by LeRat [13]. Central difference schemes of the second type have both implicit and explicit examples in the literature. Beam and Warming [14] introduced an implicit scheme, and Jameson et al. introduced an explicit scheme using a multi-stage Runge-Kutta scheme in 1981 [7] as stated in [15]. On top of these, Swanson and Turkel introduced matrix dissipation schemes, which use the diagonalized Jacobian matrix using the absolute values of the eigenvalues for each conservation equation separately, to scale the dissipation [8]. The scheme which applies the idea of limiters for overcoming the problem at discontinuities, switches from second-order to first-order accuracy. Another central-difference scheme which uses the limiter idea for each conservation equation is the Symmetric Limited Positive scheme introduced by Jameson et al. [16].

The second type of spatial discretisation schemes is the upwind schemes, which are the most widely used ones. Upwind schemes use the concept of the characteristic theory for determining the direction of spatial differencing. Characteristic theory predicts that all information flows from upstream to downstream, for supersonic flow. For subsonic flow, however, information is propagated in such a way that waves can travel in both directions i.e. upstream to downstream and downstream to upstream. Upwind schemes handle both of these cases successfully by calculating the flux at a given cell boundary based on the direction of the eigenvalues. Moreover, contrary to central difference schemes, the dissipative terms are embedded in the upwind schemes providing the terms to be scaled by the appropriate eigenvalue. Upwind schemes are divided into four sub-categories. These are:

1. Flux vector splitting schemes
2. Flux-difference splitting schemes
3. Total variation diminishing schemes

4. Fluctuation-splitting schemes

The flux vector splitting schemes, the first level of upwind schemes, only takes the direction of eigenvalues into consideration. The split fluxes in each direction are handled separately as if the flow is one-dimensional. One class of flux vector splitting schemes decomposes the flux vector according to the sign of the eigenvalues and the other type splits the flux term into convective and pressure parts. Some of the flux vector splitting schemes will be introduced briefly.

Steger-Warming (SW) flux vector splitting scheme is developed as an implicit scheme, and splits the flux vector into non-positive and non-negative parts, each associated with the signal propagation direction using the homogeneity property of the Euler equations. [17] The split fluxes are handled by the use of backward and forward differences which leads to the occurrence of sudden, unphysical changes in the flow around sonic points. Although the presented algorithm is implicit, there are many explicit applications in the literature. [3, 6, 18, 19, 20]

Due to the deficiencies in the Steger-Warming scheme, Van Leer [21] introduced an alternative flux vector splitting scheme which is good in handling the sonic points. The Van Leer (VL) splitting approximates the split Mach number using a second order polynomial, which offers the first and second derivatives to be continuous. This continuity corrects the oscillation problem through sonic and stagnation points. Van Leer flux vector splitting also provides standard upwinding in the supersonic region and also the uniqueness of the solution by adding some restrictions to the split fluxes. Large errors at the viscous region are identified by some researchers and Van Leer himself recognized that the scheme fails to capture the contact discontinuities which lead the scheme to be improved [5].

Liou and Steffen [22] states that the SW and VL schemes are simple and useful in some cases but are not accurate enough due to the high numerical diffusion. As it will be explained flux difference splitting schemes are at the expense of high calculation time. Liou and Steffen [22] aimed to develop a new flux splitting scheme, which has the efficiency of the flux vector splitting schemes on top of the

accuracy of the flux difference splitting schemes. The Advection Upstream Splitting Method (AUSM) basically differs from the introduced flux vector splitting methods by the splitting methodology. AUSM splits the flux vector into a pressure and a convective part. The scheme handles the convective terms by the face velocity obtained by the Van Leer's Mach number splitting, and pressure terms are governed by the acoustic wave speeds. The flow variables at the interfaces are calculated according to the sign of the velocity at the face. The split pressure is weighted by the Mach number. It is stated in [22] that, the AUSM gives as accurate results as the Roe's flux difference splitting scheme, and overcome the weaknesses of VL scheme. But, the scheme generates oscillations at shocks where the flow is aligned with the grid [6]. Liou [23] presented AUSM+ as an improvement on the pre-existing AUSM scheme, by modifying the definition of the Mach and pressure splittings. Liou and Wada [24] proposed AUSMDV that shows high-resolution for contact discontinuities, conservation of enthalpy for steady flows, numerical efficiency and applicability to chemically reacting flows. AUSM+ up scheme is again introduced by Liou [25] which is capable of handling the low Mach number flows. In [26] it is stated that "*Typical symptoms appearing in the application of AUSM type schemes for high-speed flows, such as pressure wiggles near a wall and overshoots across a strong shock, are cured by introducing weighting functions based on pressure (AUSMPW)*", and a new AUSM type scheme overcoming the difficulties observed in hypersonic flows is introduced and named as AUSMPW+. A robust and more accurate multidimensional compressible flow scheme by redefining the prediction of the interface states is introduced by Kim and Kim [27]. Liou published a comparison of the AUSM type schemes. [28]

Jameson [16, 29] introduced an AUSM like scheme, named Convective Upwind Split Pressure (CUSP), which is the remedy for the flow alignment case. CUSP approximates the convective flux by simple arithmetic averaging, and subtracts a diffusion term which includes the pressure flux. The definition of the diffusion term makes the scheme similar to AUSM, with the difference is that it is not weighted by Mach number. E-CUSP scheme is introduced [30] aiming to remove the temperature oscillations. Comparison between CUSP and the matrix dissipation

scheme is undertaken, and it is concluded that the matrix dissipation scheme leads to more accurate results than CUSP in coarse meshes for transonic airfoil flows [31].

A newly proposed flux vector splitting scheme, Artificially Upstream Flux Vector Splitting Scheme (AUFS), is developed to overcome all deficiencies of flux vector splitting schemes and flux difference splitting schemes in resolving shock waves, computation efficiency and time. AUFS introduces two artificial wave speeds such that one flux vector has either non-positive or non-negative eigenvalues. This allows the fluxes to be approximated by one-side differencing. Extensions of the scheme to multi-dimensions and higher orders are also presented. The scheme serves more accurate results than the compared schemes, Roe's flux difference splitting scheme and SW flux vector splitting scheme. It resolves the shocks sharper, and does not create oscillations at the sonic points. [32]

The schemes like the AUSM, CUSP, and AUFS can be named as hybrid flux-splitting scheme since they combine the superior parts of the flux vector and flux difference splitting schemes. Their goal is to reach the accuracy of the Roe's flux splitting scheme with low computational cost. Another hybrid flux-splitting scheme is introduced by Rossow for compressible flows, Mach number-based advection pressure splitting, MAPS [33]. He expanded introduced scheme with the capability of solving incompressible flow by using the Roe's flux splitting scheme in the low Mach number regions and named it as MAPS+ [34]. Both of the schemes show comparable accuracy with the Roe's flux splitting scheme and MAPS+ do not show any superiority on the MAPS for compressible flows. The convergence of both schemes is proved to be independent of the Mach number.

Extensions of the flux vector splitting schemes to real gas flows are available in the literature [35, 36].

After introducing the well-known flux vector splitting schemes, a step further can be taken. Flux difference splitting schemes are based on the solution of the local Riemann problem at each interface. The first exact Riemann solver was

developed by Godunov [37]. He proposed that the non-linear superposition of the Riemann problems lead to the general initial value problem. Thus the exact solution of Riemann problem gives almost the exact results. But this method is computationally expensive, and to reduce excessive the computational time, approximate Riemann solvers are developed. The well-known approximate Riemann solvers are developed by Roe [38] and Osher [39]. Roe found that a properly selected approximate problem does the job just as well in most cases and saves on calculation complexity. Roe's approximate Riemann solver resolves the boundary layers and shocks with a high accuracy however it does not recognize the sonic point leading the carbuncle problem. Harten's entropy correction overcomes this problem. The disadvantage of the Roe's solver is that, the extension to real gas flows is very difficult. Extension of Roe's flux difference splitting scheme to real gas flow can be found in [35]. Dick [40] developed a flux-difference splitting scheme based on the scheme of Lombard [41], the tests made lead to very accurate results. Hybrid implicit-explicit Godunov type schemes can be found in [42] and the references cited therein.

TVD (total variation diminishing) schemes are based on the concept of avoiding the creation of new extreme points in the solution. TVD schemes are monotonicity preserving schemes, meaning that the local minimum and the local maximum in the solution are non-decreasing and non-increasing, respectively, and with no change in the number of local extreme points. This property allows the TVD schemes to capture the shocks more accurately. Although the scheme serves superior properties in handling the flow, the extension to higher order accuracies is not very easy [3, 6, 43].

The last type of flux splitting schemes is the fluctuation splitting schemes. All the flux-splitting schemes introduced so far, splits the fluxes according to the orientation of the grid. The advantage of the scheme is the elimination of the grid alignment problem. The fluctuation splitting schemes are developed for cell vertex schemes. Although the fluctuation splitting schemes are said to be accurate, due to the complexity of implementation they are not widely used. Detailed information about the fluctuation splitting schemes can be found in [44, 45] and the references

cited therein.

Researches, aiming to increase the accuracy of the above presented schemes, lead to higher-order schemes. The higher-order schemes obtain at least second order truncation errors, but lead to oscillations. The well-known higher order reconstruction scheme MUSCL (Monotone Upstream-Centered Schemes for Conservation Laws), presented by Van Leer [46], is based on the Taylor series expansion. The general formula given for MUSCL in the literature [46, 6, 47] serves for the uniform structured grids. The formula can be applied to structured grids in general coordinates only by transforming the physical domain to the computational domain, and there is no way of using the general formula in unstructured tetrahedral grids without modification. Since the complex geometries need the grid to be body-fitted structured or unstructured, researchers worked on the extension of the MUSCL scheme on these types of grids. The higher-order scheme for reconstruction logic for these grids is the summation of the corresponding data with the gradient of that data over the control volume. The detailed information of the higher-order methods for unstructured and body-fitted structured grids can be found in [6, 47-55]. The use of higher order schemes makes the use of limiters compulsory. As Berger and Aftosmis states "*Limiters suppress the oscillations, and maintain the monotonicity condition, whereas they reduce accuracy and hamper convergence*" [56]. Limiters pass to first-order from second-order in the vicinity of discontinuities. Two types of limiters are used; flux limiters and slope limiters. It is stated that these two types are equivalent, and they are related to each other with a simple equation. [56] All the publications on the higher-order schemes give detailed information on the limiter functions. The reader may refer to the references on higher-order schemes, for the limiter functions.

1.2.3 Post-processor

The last part of a CFD study is to visualization of the problem itself and the proposed solution. This is taken care of by the post-processor part. In this part, the geometry and grids are displayed and the examined properties are plotted as

vectors or line and shaded contours. The developments in this field are also continuing as in the pre-processor and solver fields and recently the post-processor facilities may include dynamic result display and even data export capabilities for further manipulation to the code [1].

1.3 Present Study

The aim of this study is to develop a two-dimensional Euler solver that enables to make a comparison between different flux evaluation schemes on the basis of effectiveness and accuracy.

As a starting point, the two-dimensional Euler solver developed by Şişman [58] and Özdemir [61] using first order, cell-centered scheme with Roe's flux difference splitting for external flows, is investigated. The code is rewritten and afterwards, the code is improved by adding necessary arrangements that can offer an option to impose different flux evaluation schemes and higher-order reconstruction schemes. Moreover, the redeveloped code is aimed at an efficient use of computer memory resources and to satisfy the convergence criteria much faster compared to the original code.

Following the embodiment of the code, different flux evaluation schemes which are explained briefly in the preceding sections, are embedded in the code by using the corresponding references for each scheme as a basis. [17, 21, 22, 32, 38, 57]

In order to improve the accuracies of the results for various schemes, a second-order reconstruction scheme is set in the code. The basis for this higher-order accuracy reconstruction method is presented in [6]. A limiter function is added to the code, in order to suppress spurious oscillations occurring due to higher-order reconstruction.

Following the study for external flows, the two-dimensional Euler solver for internal flows, developed by Şişman [58] is investigated. The prewritten

external flow solver is modified by changing the boundary conditions, and it is made capable of handling internal flows.

After obtaining the results of these different flux evaluation schemes, a comparison between the obtained results and the ones presented in the literature are performed. With this step, the strengths and weaknesses are studied and the limits of the code is tried to be assessed.

This thesis consists of six chapters. The first chapter reviews the literature. The second chapter gives the derivation of the governing equations and the Euler equations. Chapter 3 explains the general solution principle of the flow, gives a detailed description of the geometrical quantities that should be used during the solution. Moreover, the used boundary conditions are explained in this chapter. In Chapter 4, the flux evaluation schemes used in this study are given in detail with the necessary references. Results obtained from the two-dimensional Euler solver are given and discussed by comparing with the results in the literature in Chapter 5. The last chapter consists of the summary of the results and recommendations for the improvement of the present code.

CHAPTER 2

GOVERNING EQUATIONS

2.1 Conservation Law

The conservation of a certain physical quantity in an arbitrary control volume Ω bounded by a control surface, S , states that the total time variation of the quantity is due to fluxes, amount of the quantity being transported across the boundary, external sources acting on the control volume, and internal sources. [3, 6]

2.1.1 General Conservation Law

The variation of a certain scalar quantity Q , in the control volume Ω , per unit time;

$$\frac{\partial}{\partial t} \int_{\Omega} Q d\Omega \quad (2.1)$$

should be equal to the net contribution from the fluxes, and volume and surface sources;

$$-\oint_S \vec{F} \cdot d\vec{S} + \int_{\Omega} Q_v d\Omega + \oint_S \vec{Q}_s \cdot d\vec{S} \quad (2.2)$$

The first term in Equation (2.2) represents the net contribution due to the incoming fluxes across the surface S , which consists of the diffusive and convective terms.

$$\vec{F} = \vec{F}_c + \vec{F}_d \quad (2.3)$$

Convective flux is due to the transport of the scalar quantity in consideration across the surface S , with the velocity \vec{V} ;

$$\vec{F}_c = -\oint_S Q(\vec{V} \cdot \vec{n}) d\vec{S} \quad (2.4)$$

on the other hand, diffusive flux, which is due to the molecular motion of the fluid particles even at rest, is defined by the Fick's gradient law. [6]

$$\vec{F}_d = \oint_S \kappa \rho \left[\nabla(Q/\rho) \cdot \vec{n} \right] d\vec{S} \quad (2.5)$$

where κ is the diffusivity constant of the transported quantity. As stated in Equation (2.5) diffusive flux is proportional to the gradient of the quantity considered and it will vanish for a homogenous flow.

General form of conservation law for a certain scalar quantity Q is;

$$\frac{\partial}{\partial t} \int_{\Omega} Q d\Omega + \oint_S \left\{ Q(\vec{v} \cdot \vec{n}) - \kappa \rho \left[\nabla(Q/\rho) \cdot \vec{n} \right] \right\} d\vec{S} = \int_{\Omega} Q_v d\Omega + \oint_S \vec{Q}_s \cdot d\vec{S} \quad (2.6)$$

Applying the Gauss's theorem to Equation (2.6), by assuming that the volume Ω is fixed, and the fluxes and sources are continuous, conservation law takes the following form;

$$\int_{\Omega} \frac{\partial Q}{\partial t} d\Omega + \int_{\Omega} \vec{V} \cdot \vec{F} d\Omega = \int_{\Omega} Q_v d\Omega + \int_{\Omega} \vec{V} \cdot \vec{Q}_s d\Omega \quad (2.7)$$

Equation (2.7) leads to the differential form of conservation law for an arbitrary control volume Ω ;

$$\frac{\partial \bar{Q}}{\partial t} + \bar{\nabla} \cdot \bar{F} = Q_v + \bar{\nabla} \cdot \bar{Q}_s \quad (2.8)$$

If the conserved quantity is not a scalar but a vector, the principle of the conservation law is still applicable. In this case, the vector variables, flux and the surface forces, become tensors, and the scalar variables, the volume sources become vectors which is given by the following equation; [3, 6]

$$\frac{\partial}{\partial t} \int_{\Omega} \vec{Q} d\Omega + \oint_S \left[\left(\bar{\bar{F}}_C - \bar{\bar{F}}_D \right) \cdot \vec{n} \right] d\vec{S} = \int_{\Omega} \bar{Q}_v d\Omega + \oint_S \left(\bar{\bar{Q}}_s \cdot \vec{n} \right) d\vec{S} \quad (2.9)$$

Applying Gauss's theorem and assuming that the sources and the fluxes are continuous for a fixed control volume, Equation (2.9) takes the form

$$\frac{\partial}{\partial t} \int_{\Omega} \bar{Q} d\Omega + \int_{\Omega} \bar{\nabla} \cdot \bar{F} d\Omega = \int_{\Omega} \bar{Q}_v d\Omega + \int_{\Omega} \bar{\nabla} \cdot \bar{\bar{Q}}_s d\Omega \quad (2.10)$$

for an arbitrary control volume, which can be expressed in the differential form as

$$\frac{\partial \bar{Q}}{\partial t} + \bar{\nabla} \cdot \left(\bar{\bar{F}} - \bar{\bar{Q}}_s \right) = \bar{Q}_v \quad (2.11)$$

The convective and diffusive flux terms in Equation (2.9), which are the parts of the total flux term in Equations (2.10) and (2.11), can be defined as [3]

$$\bar{\bar{F}}_C = \bar{V} \otimes \bar{Q} \quad (2.12)$$

$$\bar{\bar{F}}_{D_{ij}} = -\rho\kappa \frac{\partial q_j}{\partial x_j} \quad (2.13)$$

where

$$q_j = \frac{Q_j}{\rho} \quad (2.14)$$

2.1.2 Conservation of Mass

Mass can neither be created nor destroyed in a system unless a nuclear reaction exists within the system. This fact is governed by the conservation of mass. The general law of conservation applies for the kinematic property mass, with mass per unit volume, density, ρ , as the scalar quantity Q . [3]

As stated above, diffusive flux identifies the molecular motion of fluids. Since any flux created by the specific mass implies the displacement of particles, which is known as the convective flux, there is no diffusive flux contribution to the conservation of mass.

In this study, single phase fluid flow is examined, ensuring that there is no chemical reaction possibility for the fluid. Chemical reactions are the only sources, when mass is considered. So, in the absence of chemical reactions, the source term in the conservation of law drops. [3, 6, 58]

Using Equation (2.6), the conservation of mass is represented in integral form as;

$$\frac{\partial}{\partial t} \int_{\Omega} \rho d\Omega + \oint_S \rho (\bar{V} \cdot \bar{n}) d\bar{S} = 0 \quad (2.15)$$

Equation (2.15) can be stated in differential form as

$$\frac{\partial \rho}{\partial t} + \bar{\nabla} \cdot (\rho \bar{V}) = 0 \quad (2.16)$$

2.1.3 Conservation of Momentum

Momentum is a vector quantity, thus conservation law for the vector quantities given by Equation (2.9) will be used. The conserved quantity, momentum per unit volume $\rho \vec{V}$ will replace the vector quantity \vec{Q} .

Variation of momentum is due to the net force acting on the system, as stated in the Newton's second law. In other words, if no force is applied on the system, momentum of the system does not change. [6]

Some external sources of volume or body forces acting on the control volume are gravitational, buoyancy, centrifugal forces. Internal sources cancel in the volume, and they act as surface forces. [6]

Body force per unit volume, $\rho \vec{f}_b$ contributes to the conservation law as; [3, 6]

$$\int_{\Omega} \rho \vec{f}_b d\Omega \quad (2.17)$$

Pressure imposed by the surrounding fluid on the control volume and the normal & shear force caused by friction between fluid and the surface are the sources that create surface force. Surface force is expressed with the stress tensor, $\vec{\sigma}$, which is defined as; [3, 6]

$$\vec{\sigma} = -p\vec{I} + \vec{\tau} \quad (2.18)$$

where \vec{I} is the identity tensor and $\vec{\tau}$ is the viscous shear stress tensor.

Coming to the flux term, no diffusive flux contribution to the conservation of momentum since no diffusion of a fluid at rest is possible. The convective flux term consists of three components in x , y , and z -direction Cartesian coordinate

system [3]

Using conservation law for a vector quantity, conservation of momentum is written in integral form as;

$$\frac{\partial}{\partial t} \int_{\Omega} \rho \bar{V} d\Omega + \oint_S \rho \bar{V} (\bar{V} \cdot \bar{n}) d\bar{S} = \int_{\Omega} \rho \bar{f}_b d\Omega - \oint_S p \bar{n} d\bar{S} + \oint_S (\bar{\tau} \cdot \bar{n}) d\bar{S} \quad (2.19)$$

Applying Gauss's theorem to Equation (2.19), the following equation can be obtained

$$\int_{\Omega} \frac{\partial}{\partial t} \rho \bar{V} d\Omega + \int_{\Omega} \bar{\nabla} \cdot (\rho \bar{V} \otimes \bar{V}) d\Omega = \int_{\Omega} \rho \bar{f}_b d\Omega + \int_{\Omega} \bar{\nabla} \cdot \bar{\sigma} d\Omega \quad (2.20)$$

Equation (2.20) can be stated in differential form as;

$$\frac{\partial}{\partial t} (\rho \bar{V}) + \bar{\nabla} \cdot (\rho \bar{V} \otimes \bar{V} + p \bar{I} - \bar{\tau}) = \rho \bar{f}_b \quad (2.21)$$

2.1.4 Conservation of Energy

The first law of thermodynamics states that total variation of energy is equal to the net heat transferred into the system and the net work is done on it by the surrounding sources. It means that energy is conserved in case no work done on the system and no heat transfer occurred between the system and the surrounding medium. [6]

Total energy per unit mass, E , in a fluid system is the sum of the internal energy per unit mass, e , and the kinetic energy per unit mass.

$$E = e + \frac{V^2}{2} \quad (2.22)$$

Volume source terms for the conservation of energy consist of the work done by volume forces on the system, and the heat transferred to or from the system. [3, 6]

$$Q_v = \rho \vec{f}_b \cdot \vec{V} + q_h \quad (2.23)$$

Surface forces are due to the work done on the system by pressure and viscous forces. [3, 6]

$$\vec{Q}_s = \vec{\sigma} \cdot \vec{V} = -p \vec{V} + \vec{\tau} \cdot \vec{V} \quad (2.24)$$

Diffusive flux is only contributed by the internal energy, since, by definition, there is no diffusive flux associated with the motion. [3]

$$\vec{F}_d = -\gamma \rho \kappa \vec{\nabla} e \quad (2.25)$$

where γ is the ratio of specific heat coefficients under constant pressure and constant volume. Diffusive flux term in conservation of energy defines the diffusion of heat. Due to the nature of diffusion, it is by the molecular motion and molecular motion means conduction in case of heat transfer. So, diffusive flux can be expressed by Fourier's law of conduction

$$\vec{F}_d = -k \nabla T \quad (2.26)$$

where T is the absolute temperature and k is the thermal conductivity, which is

$$k = \rho c_p \kappa \quad (2.27)$$

Defining all the terms in the conservation law, Equation (2.6) can be rewritten as;

$$\frac{\partial}{\partial t} \int_{\Omega} \rho E d\Omega + \oint_S \rho E \bar{V} \cdot d\bar{S} = \oint_S k \bar{\nabla} T \cdot d\bar{S} + \int_{\Omega} (\rho \bar{f}_b \cdot \bar{V} + q_h) d\Omega + \oint_S (\bar{\sigma} \cdot \bar{V}) d\bar{S} \quad (2.28)$$

And in differential form;

$$\frac{\partial}{\partial t} (\rho E) + \bar{\nabla} \cdot (\rho \bar{V} E) = \bar{\nabla} \cdot (k \bar{\nabla} T) + \bar{\nabla} \cdot (\bar{\sigma} \cdot \bar{V}) + \rho \bar{f}_b \cdot \bar{V} + q_h \quad (2.29)$$

2.2 Complete System of the Euler Equations

In the previous section, conservation laws for mass, momentum and energy are derived separately. In this section, they are to be combined into a complete system of equations to have a better understanding of the flow variables.

Complete system of equations can be written in a compact form using the conservation of mass (2.15), conservation momentum (2.19), and conservation of energy (2.28) as;

$$\frac{\partial}{\partial t} \int_{\Omega} \bar{Q} d\Omega + \oint_S \bar{F} dS = \oint_S \bar{Q}_{sc} dS \quad (2.30)$$

In Equation (2.30) \bar{Q} represents the vector of conservative variables, and have five components for three dimensions.

$$\bar{Q} = \begin{bmatrix} \rho \\ \rho u \\ \rho v \\ \rho w \\ \rho E \end{bmatrix} \quad (2.31)$$

The second term on the left hand side of Equation (2.30) represents the convective fluxes. Flux vector, \bar{F} , represents the convective flux vector. It is due to

the convective transport of flow variables is given as;

$$\vec{F} = \begin{bmatrix} \rho \\ \rho u \\ \rho v \\ \rho w \\ \rho E \end{bmatrix} \vec{U} \quad (2.32)$$

\vec{U} is the contravariant velocity, which is the perpendicular velocity to the control volume surface, and is defined as

$$\vec{U} = \vec{V} \cdot \vec{n} \quad (2.33)$$

The term on the right hand side of Equation (2.30), represents the volume and surface source terms, and can be defined as,

$$\vec{Q}_{sc} = \begin{bmatrix} 0 \\ \rho \vec{f}_b - p \hat{i} + \vec{\tau} \cdot \hat{i} \\ \rho \vec{f}_b - p \hat{j} + \vec{\tau} \cdot \hat{j} \\ \rho \vec{f}_b - p \hat{k} + \vec{\tau} \cdot \hat{k} \\ \rho \vec{f}_b + q_h - p \vec{V} + \vec{\tau} \cdot \vec{V} + k \vec{\nabla} T \end{bmatrix} \quad (2.34)$$

The pressure terms in Equation (2.34) can be included in the convective flux term, after rearranging accordingly, Equations (2.32) and (2.34) become

$$\vec{F} = \begin{bmatrix} \rho \\ \rho u \\ \rho v \\ \rho w \\ \rho E \end{bmatrix} \vec{U} + \begin{bmatrix} 0 \\ \hat{i} \\ \hat{j} \\ \hat{k} \\ \vec{V} \end{bmatrix} p \quad (2.35)$$

$$\vec{Q}_{sc} = \begin{bmatrix} 0 \\ \rho \vec{f}_b + \vec{\tau} \cdot \hat{i} \\ \rho \vec{f}_b + \vec{\tau} \cdot \hat{j} \\ \rho \vec{f}_b + \vec{\tau} \cdot \hat{k} \\ \rho \vec{f}_b + q_h + \vec{\tau} \cdot \vec{V} + k \vec{\nabla} T \end{bmatrix} \quad (2.36)$$

Euler equations represent the pure convection properties of inviscid and non-heat-conducting flow. The system of equations is still represented in Equation (2.30) for Euler equations, \vec{F} is still defined by Equation (2.35) but definition of \vec{Q}_{sc} changes as:[3]

$$\vec{Q}_{sc} = \begin{bmatrix} 0 \\ \rho \vec{f}_b \\ \rho \vec{f}_b \\ \rho \vec{f}_b \\ \rho \vec{f}_b + q_h \end{bmatrix} \quad (2.37)$$

Investigating the system of Euler equations, it is seen that there are six physical variables, three of which are thermodynamic variables being the density, ρ ; pressure, p ; internal energy, e and the other three kinematical variables being the velocity components u , v and w . However, in the above system of equations, there exist five equations to be used to determine these six variables. It is obvious that there is a need for an additional equation in order to determine the variables. A relation for the thermodynamic variables, relating one of them to the other two, will be solution to this problem. [58]

In many cases, compressible fluid can be assumed to be a perfect gas. Equation of state is written as;

$$p = \rho RT \quad (2.38)$$

where, R is the universal gas constant per unit mass. Internal energy, is defined as

$$e = c_v T \quad (2.39)$$

where c_v is the constant volume specific heat for a thermally perfect gas, and represented as; [58, 59]

$$c_v = R/(\gamma - 1) \quad (2.40)$$

Using Equations (2.39) and (2.40), Equation (2.38) becomes

$$p = \rho e (\gamma - 1) \quad (2.41)$$

However, energy of a fluid flow is defined as the total energy, which is the sum of the internal energy and the kinetic energy. For consistency, internal energy in the pressure definition should be expressed in terms of the total energy. Then Equation (2.41) becomes

$$p = (\gamma - 1) \rho \left(E - \frac{V^2}{2} \right) \quad (2.42)$$

CHAPTER 3

PRINCIPLES OF SOLUTION

In Chapter 2, complete system of Euler equations is obtained and thermodynamic relations for a perfect gas are introduced. In this chapter, methodologies for solving this set of equations will be introduced, other than the analytical methods which have a very limited range application.

The overwhelming number of numerical schemes employs separate discretisation in space and time for the solution of Euler equations, which is called the method of lines. Dependent on the numerical method chosen, grid is used to construct the control volumes and evaluate the fluxes on the control volume faces. Resulting time dependent equations are advanced in time by the use of appropriate time discretisation method, starting with an initial solution. [3, 6]

Firstly, the assumptions used in this study will be introduced and the Euler equations will be rewritten.

Secondly, the spatial discretisation techniques used to evaluate flux term of the Euler equations will be explained broadly, which will be explained in detail in Chapter 3. Two important concepts, the physical space used to solve the flow and the geometrical quantities of the domain will be introduced under the heading of spatial discretisation. Advantages of the grid used over the other types of grids will be explained. More information on grids can be found in Chapter 1.

Having introduced the spatial discretisation techniques, the flux terms are handled and only time derivatives are to be handled. The temporal discretisation technique

used in this study will be introduced next to handle the term remaining.

Finally, the initial and boundary conditions will be explained in order to examine the flow completely.

3.1 Euler Equations

In this study, two dimensional, compressible, adiabatic, inviscid flow of ideal gases is investigated under no body forces.

The flow characteristics of this study leads to the use of Euler equations with additional assumptions. The properties of the fluid in consideration lead to some simplifications in the conservation equations. Inviscid flow assumption removes the viscous terms, adiabatic flow assumption yields the removal of heat transfer terms, and no body force assumption removes the body forces from the momentum and energy conservation equations. Considering all simplifications, \vec{Q}_{sc} term cancels in Equation (2.30), and becomes

$$\frac{\partial}{\partial t} \int_{\Omega} \vec{Q} d\Omega + \oint_S \vec{F} dS = 0 \quad (3.1)$$

Applying Gauss's theorem to (3.1),

$$\frac{\partial}{\partial t} \int_{\Omega} \vec{Q} d\Omega + \int_{\Omega} \vec{\nabla} \cdot \vec{F} d\Omega = 0 \quad (3.2)$$

\vec{Q} and \vec{F} are defined as;

$$\bar{\mathbf{Q}} = \begin{bmatrix} \rho \\ \rho u \\ \rho v \\ \rho E \end{bmatrix} \quad (3.3)$$

$$\bar{\mathbf{F}} = \begin{bmatrix} \rho \\ \rho u \\ \rho v \\ \rho E \end{bmatrix} \bar{\mathbf{U}} + \begin{bmatrix} 0 \\ \hat{i} \\ \hat{j} \\ \bar{\mathbf{V}} \end{bmatrix} p \quad (3.4)$$

Equation (3.2) is rewritten in the following form, in order to show the contents of the flux term in x and y directions.

$$\frac{\partial \bar{\mathbf{Q}}}{\partial t} + \frac{\partial \bar{\mathbf{f}}}{\partial x} + \frac{\partial \bar{\mathbf{g}}}{\partial y} = 0 \quad (3.5)$$

Although $\bar{\mathbf{Q}}$ is still defined by Equation (3.3), $\bar{\mathbf{f}}$ and $\bar{\mathbf{g}}$ being the vector of conserved fluxes in the x and y directions, respectively, are defined by;

$$\bar{\mathbf{f}} = \begin{bmatrix} \rho u \\ \rho u^2 + p \\ \rho uv \\ \rho uE + up \end{bmatrix} \quad (3.6)$$

$$\bar{\mathbf{g}} = \begin{bmatrix} \rho v \\ \rho uv \\ \rho v^2 + p \\ \rho vE + vp \end{bmatrix} \quad (3.7)$$

3.2 Spatial Discretisation

Having generated the grid, and defined the geometrical quantities the next step is to discretise the governing equations.

Spatial discretisation is a numerical approximation to the convective and viscous fluxes as well as of the source terms.

In this study, finite volume method is used as the spatial discretisation scheme. The finite volume method (FVM) is a technique introduced in the early 70's by McDonald and Mac-Cormack & Paullay to solve two-dimensional, time-dependent Euler equations. FVM takes the advantage of arbitrary mesh and doesn't need the physical domain to be converted to the computational domain. Discretisizing the conservation laws directly in the physical domain leads the conservation of basic quantities mass, momentum and energy by the numerical scheme also. [3, 6]

The conservation law for an arbitrary control volume is expressed by (3.1) in integral form.

$$\frac{\partial}{\partial t} \int_{\Omega} \bar{Q} d\Omega + \oint_S \bar{F} dS = 0 \quad (3.8)$$

The surface integral in Equation (3.8) is approximated by the sum of fluxes crossing each face of the control volume. The conservation law for an arbitrary control volume shown in Figure 3.1 is defined as;

$$\Omega_{I,J} \left(\frac{\partial \bar{Q}}{\partial t} \right)_{I,J} + \sum_{k=1}^4 \bar{F}_{I,J,k} \cdot \vec{S}_{I,J,k} = 0 \quad (3.9)$$

In the above equation k represents the individual faces of the control volume (I, J), and $\vec{S}_{I,J,k}$ stands for the face vector of the corresponding face.

The integration is based on the assumption that the fluxes are constant on the face in consideration. The conserved variables are taken to be uniform in the control volume, and the basis is taken at the centroid in this study, which is named as cell-centered as stated in Section 3.2.1.

There are a number of numerical schemes for evaluating the convective fluxes. The schemes used in this study will be explained in detail in Chapter 4. Broad information about the flux evaluation schemes can be found in Chapter 1.

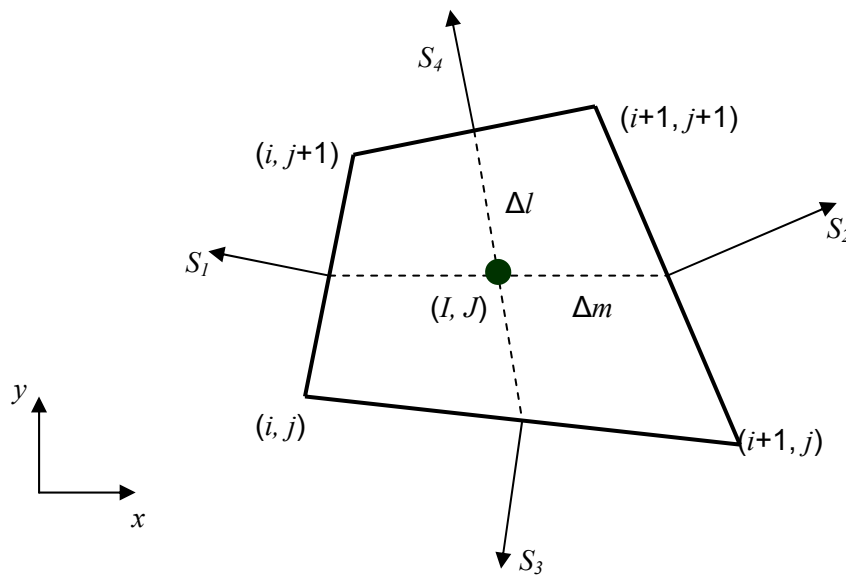


Figure 3.1: Control volume in a 2-D space

3.2.1 Physical Space

The physical space where the flow is examined is divided into a number of geometric elements, called grids. Types and properties of the grids are described in detail in Chapter 1.

Body-fitted structured O-grid is used in this study to analyze external flow over an airfoil. Figure 3.2 is a sample of body-fitted structured grid. Outer boundary of the

flow domain is a circle as the name implies. Outer boundary is taken at a 20 chord length distance from the airfoil in order to avoid reflections, in the absence of characteristic boundary conditions.

Based on the grid, control volumes are determined. The possibilities of assigning the control volumes are explained in Chapter 1. Control volume is selected to be the region surrounded by the lines connecting the nodes as shown by the hatched area in Figure 3.3, meaning that the control volume is identical to the grid cells. This is named as cell-centered scheme. Lowercase letters in the figure represent the cell vertices, while capital letters represent the cell centers.

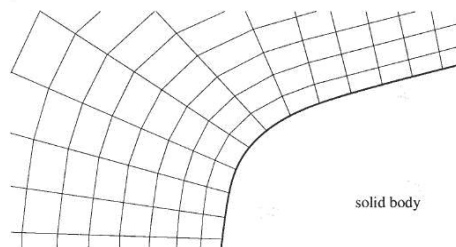


Figure 3.2: Body-fitted structured grid

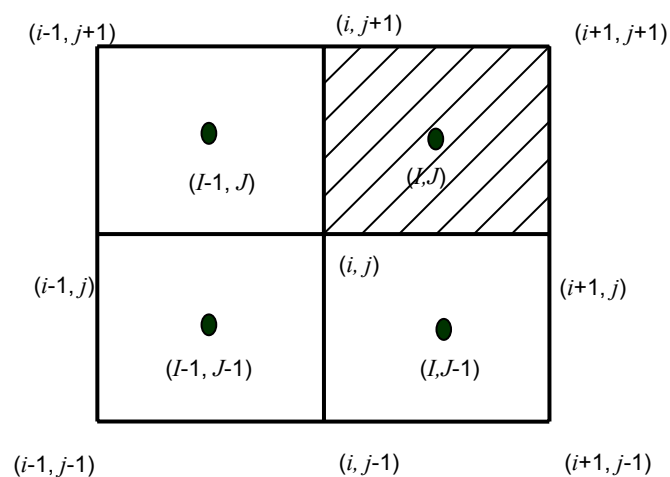


Figure 3.3: Mesh structure of control volume (I, J)

Evaluation of fluxes at cell faces in body-fitted grids is somewhat difficult than the evaluation in Cartesian grids. Despite this complexity, the difficulty of handling the boundaries in the Cartesian grids make body-fitted structured grids preferable.

3.2.2 Geometrical Quantities

Solving Euler equations by using finite volume method requires the use of unit normal vector, surface area of the cell faces and volume of the control volume in consideration.

While calculating the volume of the control volume and the area of the cell face a dept of unity for the control volume is assumed, representing the third dimension, in order to have consistent units.

The volume of an arbitrary control volume is the product of its area and its depth. Since the depth is unity, the volume of the quadrilateral control volume is numerically equal to its area. The volume can be calculated by taking the cross product of the diagonals of the control volume as represented by the following equation referring to Figure 3.1 [60]

$$\Omega_{I,J} = \frac{1}{2} \left[(x_{i,j} - x_{i+1,j+1})(y_{i+1,j} - y_{i,j+1}) + (x_{i,j+1} - x_{i+1,j})(y_{i,j} - y_{i+1,j+1}) \right] \quad (3.10)$$

The area of a surface is simply the length of the face as long as the dept is unity. As an example the area, ΔS , of face 2, in Figure 3.1 is;

$$\Delta S_2 = \sqrt{(x_{i+1,j+1} - x_{i+1,j})^2 + (y_{i+1,j+1} - y_{i+1,j})^2} \quad (3.11)$$

The unit normal vector of a face is obtained by using the face vector, \vec{S} , shown in Figure 3.3. The face vector of a control volume shown in Figure 3.1 is represented as; [6]

$$\vec{S}_m = \begin{bmatrix} \vec{S}_{x,m} \\ \vec{S}_{y,m} \end{bmatrix} = \vec{n}_m \cdot \Delta S_m \quad (3.12)$$

where \vec{n}_m is the unit normal vector, and ΔS_m is the face area represented by Equation (3.11). All the face vectors are written in an open form as;

$$\begin{aligned} \vec{S}_1 &= \begin{bmatrix} y_{i,j} - y_{i,j+1} \\ x_{i,j+1} - x_{i,j} \end{bmatrix} \\ \vec{S}_2 &= \begin{bmatrix} y_{i+1,j+1} - y_{i+1,j} \\ x_{i+1,j} - x_{i+1,j+1} \end{bmatrix} \\ \vec{S}_3 &= \begin{bmatrix} y_{i+1,j} - y_{i,j} \\ x_{i,j} - x_{i+1,j} \end{bmatrix} \\ \vec{S}_4 &= \begin{bmatrix} y_{i,j+1} - y_{i+1,j+1} \\ x_{i+1,j+1} - x_{i,j+1} \end{bmatrix} \end{aligned} \quad (3.13)$$

Computing all the face vectors for a control volume is a lack of computational time and memory. Thus, the face vectors \vec{S}_2 & \vec{S}_4 are stored in this study and in the need of face vector \vec{S}_1 , the reverse of \vec{S}_2 from the appropriate neighboring cell is used. The same holds in the case of \vec{S}_3 & \vec{S}_4 also.

3.3 Temporal Discretisation

The use of method of lines leads separate discretisation of flux and time dependent terms. Referring to the separate discretisation, the conservation equations can be written in the following form; [6]

$$\Omega_{I,J} \left(\frac{\partial Q}{\partial t} \right)_{I,J} + \vec{R}_{I,J} = 0 \quad (3.14)$$

where $\vec{R}_{I,J}$ stands for the complete finite volume spatial discretisation, called the residual term, and defined as;

$$\vec{R}_{I,J} = \sum_{k=1}^4 \vec{F}_{I,J_k} \cdot \vec{S}_{I,J_k} \quad (3.15)$$

Explicit multistage time-stepping technique is used in this study. Explicit time-stepping uses the known data at the time level n , in order to calculate the time level $n+1$. The multistage advances the solution in a number of steps, updating the solution at every step. The multistage time-stepping concept is first introduced by Jameson et al. in [7]

The time derivative in Equation (3.14) is discretised as; [6, 58]

$$\frac{Q_{I,J}^{n+1} - Q_{I,J}^n}{\Delta t} + \frac{1}{\Omega_{I,J}} \vec{R}_{I,J}^n = 0 \quad (3.16)$$

The residual term at the time level n is a function of the conservative variables at time level n . Equation (3.16) can be rearranged to obtain $Q_{I,J}^{n+1}$ as;

$$Q_{I,J}^{n+1} = Q_{I,J}^n - \frac{\Delta t}{\Omega_{I,J}} \vec{R}_{I,J}^n \quad (3.17)$$

Applying multistage time-stepping, specifically three-stage Runge-Kutta formulation, it is possible to obtain

$$\begin{aligned}
Q_{I,J}^0 &= Q_{I,J}^n \\
Q_{I,J}^1 &= Q_{I,J}^0 - \alpha_1 \frac{\Delta t_{I,J}}{\Omega_{I,J}} \bar{R}_{I,J}^0 \\
Q_{I,J}^2 &= Q_{I,J}^0 - \alpha_2 \frac{\Delta t_{I,J}}{\Omega_{I,J}} \bar{R}_{I,J}^1 \\
Q_{I,J}^3 &= Q_{I,J}^0 - \alpha_3 \frac{\Delta t_{I,J}}{\Omega_{I,J}} \bar{R}_{I,J}^2 \\
Q_{I,J}^{n+1} &= Q_{I,J}^3
\end{aligned} \tag{3.18}$$

where the stage coefficients, α are used in this study as; [58, 61]

$$\alpha_1 = 1/3 \quad \alpha_2 = 1/2 \quad \alpha_3 = 1 \tag{3.19}$$

Having defined the stage coefficients, the remaining is to define the time step in Equation (3.18). In order to have a stable explicit time-stepping scheme, time step, Δt , should fulfill Courant-Friedrichs-Lewy (CFL) criteria. This condition satisfies the time step to be equal to or smaller than time required for transforming information across the stencil, and guarantees that the associated error remains of the order of truncation error. Referring to Figure 3.1, the CFL condition is expressed as; [60]

$$\begin{aligned}
\Delta t_{I,J} &= CFL \cdot \min \left\{ \frac{\Omega_{I,J}}{\left| u \Delta y_{l_{I,J}} - v \Delta x_{l_{I,J}} \right| + c \Delta l_{I,J}}, \frac{\Omega_{I,J}}{\left| u \Delta y_{m_{I,J}} - v \Delta x_{m_{I,J}} \right| + c \Delta m_{I,J}} \right\} \\
\Delta l_{I,J} &= \sqrt{(\Delta x_{l_{I,J}})^2 + (\Delta y_{l_{I,J}})^2} \\
\Delta m_{I,J} &= \sqrt{(\Delta x_{m_{I,J}})^2 + (\Delta y_{m_{I,J}})^2}
\end{aligned} \tag{3.20}$$

where c is the speed of sound, Δm and Δl are defined in Figure 3.1.

The CFL coefficient should have values between zero and one. As it gets smaller, the information travels smaller distances and increases the convergence time. The CFL coefficient takes different values at different numerical schemes, physical spaces, free stream values etc.

3.4 Initial Conditions

The input flow variables of the study are the freestream values. All the variables in the flow field are set equal to the freestream values as an initial condition. The input variables are the stagnation temperature, T_o , stagnation pressure, P_o , angle of attack, α , and the Mach number, M . Using these input variables, following dependent variables are calculated. [62]

$$T = \frac{T_o}{\left(1 + \frac{\gamma-1}{2} M^2\right)}$$

$$p = \frac{P_o}{\left(\frac{T_o}{T}\right)^{\frac{\gamma}{\gamma-1}}}$$

$$c = \gamma RT \tag{3.21}$$

$$u = Mc \cos(\alpha)$$

$$v = Mc \sin(\alpha)$$

3.5 Boundary Conditions

The applied boundary conditions change according to the considered problem, computational domain and the flow characteristics. Implementation of the boundary conditions to the solver is important as well as the selection of the

boundary conditions.

There are two boundaries in the domain (O-grid is used), which are the solid wall and farfield boundary. The boundary conditions are applied by using the concept of ghost cells. Ghost cells are the artificial cells defined around the physical domain in order to calculate the flow variables at the boundaries. Flow is solved in the whole domain including the ghost cells.

3.5.1 Farfield Boundary Condition

The distance between the boundary of the computational domain and airfoil defines the type of the farfield boundary condition to be applied. This distance determines the effect of the boundary to the flow field. Use of characteristic boundary conditions is a must if the farfield boundary is close to the airfoil. However, if the boundary is located far enough, then it is assumed that the disturbances do not affect the flow field, and the flow variables at the farfield boundary can be set equal to the freestream values.

In this study, the boundary of the computational domain is located at a distance of 20 chord lengths from the airfoil and the flow variables are set equal to the freestream values at the boundary.

3.5.2 Solid Wall Boundary Condition

The flow variables in the ghost cell are determined by using the cell in the flow domain at the boundary. All the flow variables in the ghost cell, except the normal velocity, are taken to be equal to the ones in the boundary cell. The normal velocity in the boundary cell is assigned to the ghost cell with an opposite sign. This leads to zero normal velocity component at the boundary preserving no mass flux through the wall.

CHAPTER 4

FLUX EVALUATION SCHEMES

The majority of numerical schemes employ separate discretisation in space and time, namely method of lines, for the solution of Euler equations as stated in Chapter 2. This separate discretisation allows using different levels of accuracy for approximating the time and space derivatives. The main idea of this chapter is the explanation of the spatial discretisation techniques used in this study and the evaluation of the flux quantities at the left and right cell face boundaries. Since the solution is known and stored only at the cell average points (assumed to be the cell centers), neither the conservative variables nor the fluxes are known at the interface boundaries.

The chapter begins with the quasi-linear formulation of the Euler equations which will lead to the derivation of the Jacobian matrices and the eigenvalues of Euler equations.

Flux evaluation schemes starting with the flux vector splitting schemes will be introduced next. Detailed description of the flux vector splitting schemes such as; Steger-Warming Flux Vector Splitting Scheme, Van-Leer Flux Vector Splitting Scheme, Advection Upstream Splitting Method (AUSM), and Artificially Upstream flux vector splitting (AUFS) scheme will be given.

Having introduced the flux vector splitting schemes, flux difference splitting schemes is left as flux evaluation schemes used in this study. Basis of the flux difference splitting schemes, Riemann problem and the Godunov approach will be explained as an introduction. These will be followed by the description of the

Roe's approximate Riemann solver.

Finally, reconstruction techniques that should be used to evaluate the face fluxes and limiter functions used to eliminate non-physical oscillations will be defined.

4.1 The Quasi-Linear Formulation of the Euler Equations

The Euler equations should be written in a quasi-linear form in order to investigate its mathematical properties. Euler equations defined by Equation (3.5) are of first order in the variables \bar{Q} , and are written in a quasi-linear form as; [3]

$$\frac{\partial \bar{Q}}{\partial t} + \left(\frac{\partial \bar{F}}{\partial \bar{Q}} \right) \cdot \bar{\nabla} \bar{Q} = 0 \quad (4.1)$$

or

$$\frac{\partial \bar{Q}}{\partial t} + \bar{A} \cdot \bar{\nabla} \bar{Q} = 0 \quad (4.2)$$

or explicitly,

$$\frac{\partial \bar{Q}}{\partial t} + \frac{\partial \bar{f}}{\partial \bar{Q}} \frac{\partial \bar{Q}}{\partial x} + \frac{\partial \bar{g}}{\partial \bar{Q}} \frac{\partial \bar{Q}}{\partial y} = 0 \quad (4.3)$$

4.1.1 The Jacobian Matrices

Equation (4.2) includes the Jacobian matrix, \bar{a} , of flux vector \bar{F} . Equation (4.2) is written explicitly in Equation (4.3) to show the components of the Jacobian matrix due to the x and y components of the flux vector. From Equation (4.3) it can be written that

$$[A] = \frac{\partial \vec{f}}{\partial \vec{Q}} \quad \text{and} \quad [B] = \frac{\partial \vec{g}}{\partial \vec{Q}} \quad (4.4)$$

Expressing the conservative variables, \vec{Q} (3.3) in the following form: [3]

$$\vec{Q} = \begin{bmatrix} \rho \\ \rho u \\ \rho v \\ \rho E \end{bmatrix} = \begin{bmatrix} \rho \\ m \\ n \\ \varepsilon \end{bmatrix} \quad (4.5)$$

The flux vector components can be written in the form,

$$\vec{f} = \begin{bmatrix} m \\ \frac{m^2}{\rho} + p \\ \frac{mn}{\rho} \\ \frac{m}{\rho}(\varepsilon + p) \end{bmatrix} \quad \text{and} \quad \vec{g} = \begin{bmatrix} n \\ \frac{mn}{\rho} \\ \frac{n^2}{\rho} + p \\ \frac{n}{\rho}(\varepsilon + p) \end{bmatrix} \quad (4.6)$$

where,

$$\varepsilon = \rho e + \frac{m^2 + n^2}{2\rho} \quad \text{and} \quad p = (\gamma - 1) \left(\varepsilon - \frac{m^2 + n^2}{2\rho} \right) \quad (4.7)$$

Then the components of the Jacobian matrix due to the x and y components of the flux vector are written as follows:

$$[A] = \frac{\partial \bar{f}}{\partial \bar{Q}} = \begin{bmatrix} \frac{\partial f}{\partial \rho} \\ \frac{\partial f}{\partial m} \\ \frac{\partial f}{\partial n} \\ \frac{\partial f}{\partial \varepsilon} \end{bmatrix} \quad \text{and} \quad [B] = \frac{\partial \bar{g}}{\partial \bar{Q}} = \begin{bmatrix} \frac{\partial g}{\partial \rho} \\ \frac{\partial g}{\partial m} \\ \frac{\partial g}{\partial n} \\ \frac{\partial g}{\partial \varepsilon} \end{bmatrix} \quad (4.8)$$

Derivation of the derivatives constructing [A] matrix leads to,

$$\frac{\partial \bar{f}}{\partial \rho} = \begin{bmatrix} 0 \\ -\frac{m^2}{\rho^2} + \frac{\partial p}{\partial \rho} \\ -\frac{mn}{\rho^2} \\ -\frac{m}{\rho^2}(\varepsilon + p) + \frac{m}{\rho} \frac{\partial p}{\partial \rho} \end{bmatrix} \quad (4.9)$$

$$\frac{\partial \bar{f}}{\partial m} = \begin{bmatrix} 1 \\ 2\frac{m}{\rho} - (\gamma - 1)\frac{m}{\rho} \\ \frac{n}{\rho} \\ \frac{\gamma\varepsilon}{\rho} - \frac{(\gamma - 1)}{2\rho^2}(3m^2 + n^2) \end{bmatrix} \quad (4.10)$$

$$\frac{\partial \bar{f}}{\partial n} = \begin{bmatrix} 0 \\ -(\gamma - 1)\frac{n}{\rho} \\ \frac{m}{\rho} \\ -(\gamma - 1)\frac{mn}{\rho^2} \end{bmatrix} \quad (4.11)$$

$$\frac{\partial \vec{f}}{\partial \varepsilon} = \begin{bmatrix} 0 \\ (\gamma-1) \\ 0 \\ \gamma u \end{bmatrix} \quad (4.12)$$

Combining Equations (4.9), (4.10), (4.11), and (4.12) leads to the general form of the Jacobian matrix [A] of a 2-D Euler equation. [A] matrix in the explicit form can be written as follows, [3]

$$[A] = \begin{bmatrix} 0 & 1 & 0 & 0 \\ \frac{\gamma-3}{2}u^2 + \frac{\gamma-1}{2}v^2 & (3-\gamma)u & -(\gamma-1)v & \gamma-1 \\ -uv & v & u & 0 \\ -\gamma uE + (\gamma-1)u(u^2+v^2) & \gamma E - \frac{\gamma-1}{2}(3u^2+v^2) & -(\gamma-1)uv & \gamma u \end{bmatrix} \quad (4.13)$$

The derivation of the [A] matrix is complete. [B] matrix is derived in the same manner as, [3]

$$[B] = \begin{bmatrix} 0 & 1 & 0 & 0 \\ -uv & v & u & \gamma-1 \\ \frac{\gamma-1}{2}u^2 + \frac{\gamma-3}{2}v^2 & -(\gamma-1)u & (3-\gamma)u & 0 \\ -\gamma vE + (\gamma-1)v(u^2+v^2) & -(\gamma-1)uv & \gamma E - \frac{\gamma-1}{2}(u^2+3v^2) & \gamma v \end{bmatrix} \quad (4.14)$$

Further details on the Jacobian matrix evaluation can be found in Rohde [63], Hirsch[3] and Toro [18].

The Euler equations (3.3), with Equations (3.5), (3.6) and (3.7) are homogenous in the case of a perfect gas, (2.38). [3, 17, 18] this implies that

$$\vec{F}(\lambda Q) = \lambda \vec{F}(Q) \quad \text{for any } \lambda \quad (4.15)$$

Meaning that

$$F(Q) = \frac{\partial \vec{F}}{\partial \vec{Q}} \vec{Q} = [a] \vec{Q} \quad (4.16)$$

$$\vec{f} = [A] \vec{Q} \quad \vec{g} = [B] \vec{Q}$$

To prove this property, one can multiply the Jacobian matrix (4.13) or (4.14) by matrix \vec{Q} (4.5) to obtain \vec{f} , (3.6) and \vec{g} , (3.7) matrices, respectively. This property forms the basis of flux vector splitting schemes. [17, 18]

4.1.2 Eigenvalues of Euler Equations

The eigenvalues of the Jacobian matrix, $[a]$, are the roots λ_i of the characteristic equation,

$$\det(a - \lambda I) = 0 \quad (4.17)$$

where $[I]$ is the identity matrix. It turns out four eigenvalues, three of which are distinct and one is repeated.

$$[\Lambda] = \lambda_k = \{u_n, u_n + c, u_n - c, \} \quad (4.18)$$

The homogeneity property of the hyperbolic Euler equations leads to,

$$[T]^{-1} [a] [T] = [\Lambda] \quad (4.19)$$

where $[T]$ is the matrix of whose columns are the right eigenvectors, $[T]^{-1}$ is the inverse of matrix $[T]$, which is the matrix whose rows are the left eigenvectors and $[\Lambda]$ is the diagonal matrix of eigenvalues. The matrices of the left and right

eigenvectors can be found in the literature. [3, 63]

The i^{th} equation of one dimensional quasi-linear Euler equations (4.20),

$$\frac{\partial \bar{Q}_i}{\partial t} + \lambda_i \frac{\partial \bar{Q}_i}{\partial x} = 0 \quad (4.20)$$

has a wave solution represented by

$$\bar{Q}_i = \text{constant for } \frac{dx}{dt} = \lambda_i \quad (4.21)$$

Curves represented by Equation (4.21) are the characteristic curves and λ_i are the eigenvalues or characteristic speeds. Information is carried along the characteristic curves with the characteristic speed. Referring to (4.21) it can be said that, i^{th} characteristic variable is constant along the corresponding characteristic curve. [3, 17, 64]

4.2 Upwind Schemes

Eigenvalues of Euler equations, as stated in the previous section; represent the velocity thus the direction of propagation of information in the flow field. The central difference schemes, as stated in Chapter 1; does not distinguish upstream from downstream influences. Although central schemes can be applied at any order of accuracy in the smooth flow regions, these schemes are not good for handling shock waves without artificial dissipation terms. Artificial dissipation terms leads to excessive numerical dissipation, which needs to be limited even in the smooth flow regions. The numerical dissipation model is improved with the assistance of upwind schemes. Upwind schemes numerically simulate the direction of propagation of information in the flow field. [3, 8, 20]

For supersonic flows, characteristic theory predicts that all information

transmission flows from upstream to downstream. For subsonic flow, however, information is propagated in such a way that waves can travel both upstream to downstream and downstream to upstream. Thus, a flux calculation algorithm must be of such a form that it calculates the flux at a given cell boundary based on cell values only to the upstream side of the boundary for supersonic flows, and from both sides of the boundary for subsonic flows. This procedure is further complicated by the fact that a shock wave will create a situation where supersonic flow is present on one side of the shock and subsonic flow is on the other side. The presence of the shock must be correctly admitted by the conservative flux scheme as well. [3, 8]

Following subsections will introduce the upwind discretisation techniques used in this study.

4.2.1 Flux Vector Splitting

The flux vector splitting methods are considered as the first level of upwind schemes. They only account for the sign of the eigenvalues, namely the wave propagation direction. The well-known splitting schemes presented by Steger-Warming [17], and Van Leer [21] splits the fluxes into two, according to the sign of the eigenvalues. Schemes offered by Liou et al. [22]; Advection Upstream Splitting Method (AUSM) and Jameson et al. [29]; Convective Upwind Split Pressure (CUSP) splits the flux into a convective and a pressure part.

4.2.1.1 Steger-Warming Flux Vector Splitting

Steger-Warming aimed to extend the class of spatial differencing schemes for more robust algorithms and improve the efficiency of implicit methods by developing a new flux splitting method. Although the method is developed for implicit schemes, there are many applications of explicit schemes even presented in the publication of Steger-Warming. [17]

Steger-Warming states that the flux vector \bar{F} is homogenous of degree one in \bar{Q}

if the equation of state is of the form; [17]

$$p = \rho f(e) \quad (4.22)$$

Since equation of state in the set of Euler equations is written as shown by Equation (2.42), the inviscid flux vector in the set of Euler equations are homogenous of degree one in \bar{Q} . [17]

Steger-Warming flux vector splitting scheme uses the property of inviscid flux vectors being homogenous of degree one and splits the flux vectors \bar{f} and \bar{g} into subvectors; a positive and a negative part according to the sign of the eigenvalues. [17]

As previously shown, the homogeneity lets the flux vector written in the form;

$$\bar{F} = [a]\bar{Q} \quad (4.23)$$

and the system of Euler equations, which are hyperbolic, lets the matrix of real eigenvalues written in the form

$$[T]^{-1}[a][T] = [\Lambda] \quad (4.24)$$

Combining Equations (4.23) and (4.24), \bar{F} is written as

$$\bar{F} = [a]\bar{Q} = [T][\Lambda][T]^{-1}\bar{Q} \quad (4.25)$$

Splitting the eigenvalues according to their signs [a] matrix is written as follows

$$[\mathbf{a}] = [\mathbf{a}^+] + [\mathbf{a}^-] = [\mathbf{T}][\Lambda^+][\mathbf{T}]^{-1} + [\mathbf{T}][\Lambda^-][\mathbf{T}]^{-1} \quad (4.26)$$

Inserting the above equation into \vec{F} equation

$$\vec{F} = \vec{F}^+ + \vec{F}^- = [\mathbf{T}][\Lambda^+][\mathbf{T}]^{-1}\vec{Q} + [\mathbf{T}][\Lambda^-][\mathbf{T}]^{-1}\vec{Q} \quad (4.27)$$

As stated in Section 3.1, inviscid flux vector \vec{F} has components \vec{f} and \vec{g} in x and y directions, respectively. The subvectors of the inviscid flux vector also have Jacobian, $[\mathbf{A}]$ and $[\mathbf{B}]$ respectively, and eigenvalue matrices of each Jacobian is $[\Lambda_1]$ and $[\Lambda_2]$ respectively. [3]

$$[\mathbf{T}_1]^{-1}[\mathbf{A}][\mathbf{T}_1] = [\Lambda_1] = \begin{bmatrix} u & 0 & 0 & 0 \\ 0 & u & 0 & 0 \\ 0 & 0 & u+c & 0 \\ 0 & 0 & 0 & u-c \end{bmatrix} \quad (4.28)$$

$$[\mathbf{T}_2]^{-1}[\mathbf{B}][\mathbf{T}_2] = [\Lambda_2] = \begin{bmatrix} v & 0 & 0 & 0 \\ 0 & v & 0 & 0 \\ 0 & 0 & v+c & 0 \\ 0 & 0 & 0 & v-c \end{bmatrix} \quad (4.29)$$

The relations written above for the flux vector \vec{F} are also applicable for the x - and y - components, \vec{f} and \vec{g} respectively, of the flux vector \vec{F} .

$$\vec{f} = \vec{f}^+ + \vec{f}^- = [\mathbf{A}^+]\vec{Q} + [\mathbf{A}^-]\vec{Q} = [\mathbf{T}_1][\Lambda_1^+][\mathbf{T}_1]^{-1}\vec{Q} + [\mathbf{T}_1][\Lambda_1^-][\mathbf{T}_1]^{-1}\vec{Q} \quad (4.30)$$

$$\vec{g} = \vec{g}^+ + \vec{g}^- = [\mathbf{B}^+]\vec{Q} + [\mathbf{B}^-]\vec{Q} = [\mathbf{T}_2][\Lambda_2^+][\mathbf{T}_2]^{-1}\vec{Q} + [\mathbf{T}_2][\Lambda_2^-][\mathbf{T}_2]^{-1}\vec{Q} \quad (4.31)$$

The split fluxes \vec{f}^+ , \vec{f}^- , \vec{g}^+ and \vec{g}^- are also homogenous functions of degree one

in \bar{Q} . $[\Lambda_1^+]$ represents the eigenvalues matrix of the Jacobian of \bar{f} with only positive elements, $[\Lambda_1^-]$ represents the eigenvalues matrix of the Jacobian of \bar{f} with only negative elements, $[\Lambda_2^+]$ represents the eigenvalues matrix of the Jacobian of \bar{g} with only positive elements, $[\Lambda_2^-]$ represents the eigenvalues matrix of the Jacobian of \bar{g} with only negative elements such that, [3, 17]

$$[\Lambda] = [\Lambda]^+ + [\Lambda]^- \quad [\Lambda] = [\Lambda]^+ - [\Lambda]^- \quad (4.32)$$

or

$$\lambda = \lambda^+ + \lambda^- \quad \lambda = \lambda^+ - \lambda^- \quad (4.33)$$

The positive and negative eigenvalues are defined as

$$\lambda_k^+ = \frac{\lambda_k + |\lambda_k|}{2} \quad \lambda_k^- = \frac{\lambda_k - |\lambda_k|}{2} \quad (4.34)$$

The conservative form of Euler equations using the split-fluxes is written as

$$\frac{\partial \bar{Q}}{\partial t} + \frac{\partial \bar{f}^+}{\partial x} + \frac{\partial \bar{f}^-}{\partial x} + \frac{\partial \bar{g}^+}{\partial y} + \frac{\partial \bar{g}^-}{\partial y} = 0 \quad (4.35)$$

where the plus and minus signs designate the flux components due to the waves propagating in the positive and negative directions, respectively.

a) Subsonic flow

For subsonic flow, $u_n < c$ meaning that the fourth eigenvalue, $u_n - c$, both in $[\Lambda_1]$ and $[\Lambda_2]$ are negative, and the other three are positive with u_n being positive.

Consequently, for the general eigenvalue matrix

$$[\Lambda]^+ = \begin{bmatrix} u_n & 0 & 0 & 0 \\ 0 & u_n & 0 & 0 \\ 0 & 0 & u_n + c & 0 \\ 0 & 0 & 0 & 0 \end{bmatrix} \quad (4.36)$$

$$[\Lambda]^- = \begin{bmatrix} 0 & 0 & 0 & 0 \\ 0 & 0 & 0 & 0 \\ 0 & 0 & 0 & 0 \\ 0 & 0 & 0 & u_n - c \end{bmatrix} \quad (4.37)$$

The corresponding Jacobians are found using Equations (4.28) and (4.29), for \vec{f} and \vec{g} , respectively, with $[T]$ and $[T]^{-1}$ defined by Equation (4.19). These will lead to the split fluxes, with λ_1^\mp and λ_2^\mp being the same for Euler equations,

$$\vec{f}^\mp = \frac{\rho}{2\gamma} \begin{bmatrix} \alpha \\ \alpha u + c(\lambda_3^\mp + \lambda_4^\mp) \\ \alpha v \\ \alpha \frac{u^2 + v^2}{2} + uc(\lambda_3^\mp + \lambda_4^\mp) + c^2 \frac{(\lambda_3^\mp + \lambda_4^\mp)}{\gamma - 1} \end{bmatrix} \quad (4.38)$$

$$\vec{g}^\mp = \frac{\rho}{2\gamma} \begin{bmatrix} \alpha \\ \alpha u \\ \alpha v + c(\lambda_3^\mp - \lambda_4^\mp) \\ \alpha \frac{u^2 + v^2}{2} + vc(\lambda_3^\mp - \lambda_4^\mp) + c^2 \frac{(\lambda_3^\mp + \lambda_4^\mp)}{\gamma - 1} \end{bmatrix} \quad (4.39)$$

where

$$\alpha = 2(\gamma - 1)\lambda_1^{\mp} + \lambda_3^{\mp} + \lambda_4^{\mp} \quad (4.40)$$

b) Supersonic flow

For supersonic flow, $u_n > c$ meaning that all the eigenvalues are in the same direction. With u_n being positive, all the eigenvalues are positive. Then,

$$\vec{F}^+ = \vec{F} \quad \text{and} \quad \vec{F}^- = 0 \quad (4.41)$$

or

$$\vec{f}^+ = \vec{f} \quad \text{and} \quad \vec{f}^- = 0 \quad (4.42)$$

$$\vec{g}^+ = \vec{g} \quad \text{and} \quad \vec{g}^- = 0 \quad (4.43)$$

4.2.1.2 Van-Leer Flux Vector Splitting

The Van Leer (1979) flux vector splitting is one of a large body of similar techniques. Since a general fluid flow contains wave speeds that are both positive and negative (so that eigenvalue information can pass both upstream and downstream), the basic idea behind all of these techniques is that the flux can be split into two components so that each may be properly discretised using relatively upwind stencils to maintain stability and accuracy.

As Anderson, Thomas and Van Leer [20] stated the split fluxes of Steger-Warming are not continuously differentiable at sonic and stationary points, where an eigenvalue changes sign. This leads to the occurrence of small glitches or oscillations in the corresponding regions. The Van Leer flux splitting sought to correct some problems found at sonic and stagnation points in order to lead smoother solutions at those points, for an earlier splitting called Steger-Warming. [5]

Van Leer bases his flux vector splitting on Mach number splitting and imposed number of conditions on the split fluxes, namely.

The first recommendation is that, the split Jacobian matrices

$$\begin{aligned}
 [A]^+ &= \frac{\partial \bar{f}^+}{\partial \bar{Q}} \quad \text{and} \quad [A]^- = \frac{\partial \bar{f}^-}{\partial \bar{Q}} \\
 [B]^+ &= \frac{\partial \bar{g}^+}{\partial \bar{Q}} \quad \text{and} \quad [B]^- = \frac{\partial \bar{g}^-}{\partial \bar{Q}}
 \end{aligned}
 \tag{4.44}$$

should be continuous functions of Mach number and expressed as lowest possible order. The second one is that the split Jacobian matrices $[A]^+$ and $[B]^+$ should be formed of positive or zero eigenvalues and $[A]^-$ and $[B]^-$ should be formed of negative or zero eigenvalues, with one eigenvalue equal to zero in the subsonic flow range. [3,18]

Hirsch states that the requirements of the splitting leads the flux components to be proportional to $(M \pm 1)^n$, and the lowest possible order satisfying the above rules is $n=2$. Positive flux components are proportional to $(M+1)^2$ and negative ones are proportional to $(M-1)^2$. The second order approximation of the Mach number insures zero and first order continuity at the sonic points, $M = +1$ and $M = -1$. [3]

The Mach number for supersonic flow is simply the full scalar Mach number in the downwind direction, and zero in the upwind direction. For subsonic flow, the Mach number is slightly more complex.

$$M = M_L^+ + M_R^-
 \tag{4.45}$$

$$M^\pm = \begin{cases} \pm \frac{1}{4}(M \pm 1)^2, & \text{for } |M| \leq 1 \\ \frac{1}{2}(M \pm |M|), & \text{otherwise} \end{cases} \quad (4.46)$$

a) Subsonic Flow

For subsonic flow, $u_n < c$ meaning that the fourth eigenvalue, $u_n - c$, both in $[\Lambda_1]$ and $[\Lambda_2]$ are negative, and the other three are positive with u_n being positive. Consequently the split fluxes of Van Leer are written as;

$$\vec{f}_{VL}^\pm = \vec{f}_{1,VL}^\pm \begin{bmatrix} 1 \\ \frac{(\gamma-1)u \pm 2c}{\gamma} \\ v \\ \frac{v^2}{2} + \frac{[(\gamma-1)u \pm 2c]^2}{2(\gamma^2-1)} \end{bmatrix} \quad (4.47)$$

with

$$\vec{f}_{1,VL}^\pm = \pm \frac{\rho}{4c} (u \pm c)^2 \quad (4.48)$$

Similarly the split flux in the y direction is;

$$\vec{g}_{VL}^\pm = \vec{g}_{1,VL}^\pm \begin{bmatrix} 1 \\ u \\ \frac{(\gamma-1)v \pm 2c}{\gamma} \\ \frac{u^2}{2} + \frac{[(\gamma-1)v \pm 2c]^2}{2(\gamma^2-1)} \end{bmatrix} \quad (4.49)$$

with

$$\vec{g}_{i,VL}^{\pm} = \pm \frac{\rho}{4c} (v \pm c)^2 \quad (4.50)$$

b) Supersonic flow

For supersonic flow, $u_n > c$ meaning that all the eigenvalues are in the same direction. With u_n being positive, all the eigenvalues are positive. Then, as in the Steger-Warming Flux vector splitting;

$$\vec{F}^+ = \vec{F} \quad \text{and} \quad \vec{F}^- = 0 \quad (4.51)$$

or

$$\vec{f}^+ = \vec{f} \quad \text{and} \quad \vec{f}^- = 0 \quad (4.52)$$

$$\vec{g}^+ = \vec{g} \quad \text{and} \quad \vec{g}^- = 0 \quad (4.53)$$

4.2.1.3 Advection Upstream Splitting Method (AUSM)

The Advection Upstream Splitting Method (AUSM) is a method similar in principle to the Van Leer flux splitting and introduced by Liou and Steffen in 1993. Van Leer flux splitting has a significant defect in resolving the stationary contact discontinuities. For this reason Liou and Steffen aimed to develop a scheme that has a satisfactory resolution of stationary contact discontinuities. Liou and Steffen states that their goal is to design a new algorithm which is more accurate and more efficient than other flux vector splitting schemes and simpler than and as accurate as the flux difference schemes. [22]

Since the convective terms in the flux term are “*passive scalar quantities*” convected by the velocity at the cell interface and the pressure flux terms are

governed by the acoustic wave speeds, the flux term is split into these two separate components so that each one may be properly upwind stenciled. The flux term is written as

$$\vec{f} = \vec{f}_c + \vec{f}_p = \begin{bmatrix} \rho \\ \rho u \\ \rho v \\ \rho H \end{bmatrix} u + \begin{bmatrix} 0 \\ p \\ 0 \\ 0 \end{bmatrix} \quad (4.54)$$

where H is the total enthalpy per unit mass, and defined by $H = E + \frac{p}{\rho}$.

The convective flux terms are discretised in purely upwind manner depending on the velocity at the cell interface which carries the “*passive scalar quantities*”.

$$\vec{f}_c = \begin{bmatrix} \rho \\ \rho u \\ \rho v \\ \rho H \end{bmatrix}_{L/R} u = M \begin{bmatrix} \rho a \\ \rho a u \\ \rho a v \\ \rho a H \end{bmatrix}_{L/R} \quad (4.55)$$

where

$$(\cdot)_{L/R} = \begin{cases} (\cdot)_L & \text{if } M \geq 0 \\ (\cdot)_R & \text{otherwise} \end{cases} \quad (4.56)$$

The advection Mach number is evaluated as a sum of the left and right split Mach numbers just as in the Van Leer’s flux vector splitting, according to the relations (4.45) and (4.46).

After defining the method of handling the convective flux term, Liou and Steffen defines the pressure term in the flux. The pressure term is split by using the polynomial expansions of the $(M \pm 1)$. The pressure term can be expressed using

the first or second order polynomials of $(M \pm 1)$. Although it is stated in [22] that both of these two splittings give almost the same results, the second order polynomial of $(M \pm 1)$ is used in this study.

$$p = p_L^+ + p_R^- \quad (4.57)$$

$$p^\pm = \begin{cases} \pm \frac{p}{2} (M \pm 1)^2 (2 \pm M), & \text{for } |M| \leq 1 \\ \frac{p}{2} (M \pm |M|) / M, & \text{otherwise} \end{cases} \quad (4.58)$$

The flux term, using the above definitions, can be expressed as

$$\bar{f} = \frac{1}{2} M \left(\begin{bmatrix} \rho a \\ \rho a u \\ \rho a v \\ \rho a H \end{bmatrix}_L + \begin{bmatrix} \rho a \\ \rho a u \\ \rho a v \\ \rho a H \end{bmatrix}_R \right) - \frac{1}{2} |M| \Delta_{1/2} \begin{bmatrix} \rho a \\ \rho a u \\ \rho a v \\ \rho a H \end{bmatrix} + \begin{bmatrix} 0 \\ p \\ 0 \\ 0 \end{bmatrix} \quad (4.59)$$

where

$$\Delta_{1/2}(\cdot) = (\cdot)_R - (\cdot)_L \quad (4.60)$$

The first term on the right hand side of Equation (4.59) represents the Mach number-weighted average of fluxes, while the second term accounts for the numerical dissipation which has a dissipative character.

The \bar{g} flux term is expressed similarly,

$$\bar{g} = \frac{1}{2} M \left(\begin{bmatrix} \rho a \\ \rho a u \\ \rho a v \\ \rho a H \end{bmatrix}_L + \begin{bmatrix} \rho a \\ \rho a u \\ \rho a v \\ \rho a H \end{bmatrix}_R \right) - \frac{1}{2} |M| \Delta_{1/2} \begin{bmatrix} \rho a \\ \rho a u \\ \rho a v \\ \rho a H \end{bmatrix} + \begin{bmatrix} 0 \\ 0 \\ p \\ 0 \end{bmatrix} \quad (4.61)$$

Although the original AUSM scheme has proven to be robust, accurate and simple, it has some drawbacks such as generating pressure oscillations at shocks where the flow is aligned with the grid [28]. Researchers have been studying on the original scheme for years to overcome the deficiencies of the original AUSM scheme by mainly changing the pressure and Mach splitting, and many versions of the original scheme come into view. Details of these schemes can be found in the cited references. [23, 24, 25, 26, 27, 28]

4.2.1.4 Artificially Upstream Flux Vector Splitting Scheme (AUFS)

Artificially Upstream Flux Vector Splitting Scheme is a newly introduced scheme by Sun and Takayama in 2003. Their aim is to develop a new scheme that overcomes all deficiencies of flux vector splitting schemes and flux difference splitting schemes in resolving shock waves, computation efficiency and time, like Liou and Steffen.

AUFS introduces two artificial wave speeds for splitting the flux vector. The artificial wave speeds are selected such that one flux vector has either non-positive or non-negative eigenvalues, and the other one has two waves and two stationary discontinuities for two dimensional flows. This decomposition of the flux vector leads the flux vector that has unidirectional eigenvalues to be solved by one-side differencing. [32]

The flux term can be splitted as:

$$\vec{f} = (1-M) \left\{ (u-s_1) \begin{bmatrix} \rho \\ \rho u \\ \rho v \\ E \end{bmatrix} + \begin{bmatrix} 0 \\ p \\ 0 \\ \rho u \end{bmatrix} \right\} + M \left\{ (u-s_2) \begin{bmatrix} \rho \\ \rho u \\ \rho v \\ E \end{bmatrix} + \begin{bmatrix} 0 \\ p \\ 0 \\ \rho u \end{bmatrix} \right\} \quad (4.62)$$

Mach number, for consistency, is defined as:

$$M = \frac{s_1}{s_1 - s_2} \quad (4.63)$$

Equation (4.62) can be expressed more clearly in the following form:

$$\vec{f} = (1-M)\vec{f}_1 + M\vec{f}_2 \quad (4.64)$$

where

$$\vec{f}_{1,2} = (u-s_{1,2}) \begin{bmatrix} \rho \\ \rho u \\ \rho v \\ E \end{bmatrix} + \begin{bmatrix} 0 \\ p \\ 0 \\ \rho u \end{bmatrix} \quad (4.65)$$

Since these two flux vectors are different from the original one, their eigenvalues are also different. The eigenvalues of flux vectors $\vec{f}_{1,2}$ are

$$\Lambda_{1,2} = \begin{bmatrix} u-s_{1,2}-c & 0 & 0 & 0 \\ 0 & u-s_{1,2} & 0 & 0 \\ 0 & 0 & u-s_{1,2} & 0 \\ 0 & 0 & 0 & u-s_{1,2}+c \end{bmatrix} \quad (4.66)$$

Sun and Takayama introduces two ways of defining the artificial wave speeds s_1 , and s_2 . The first method introduced in [32] selects s_1 , and s_2 , such that the

eigenvalues in Equation (4.66) are either non-positive or non-negative. The second one on the other hand, selects s_1 , and s_2 , such that one set of eigenvalues is unidirectional and the other one consists of two symmetric sound waves and two stationary contact waves. The latter one is more efficient in resolving contact discontinuities and it is used in this study.

$$s_1 = \frac{(u_L + u_R)}{2}$$

$$s_2 = \begin{cases} \min(0, u_L - c_L, u^* - c^*) & \text{for } s_1 > 0 \\ \max(0, u_R + c_R, u^* + c^*) & \text{for } s_1 \leq 0 \end{cases} \quad (4.67)$$

The speed u^* and speed of sound c^* are obtained by the use of isentropic gas dynamics equations and are defined as follows;

$$u^* = \frac{1}{2}(u_L + u_R) + \frac{(c_L - c_R)}{\gamma - 1} \quad (4.68)$$

$$c^* = \frac{1}{2}(c_L + c_R) + \frac{1}{4}(\gamma - 1)(u_L - u_R) \quad (4.69)$$

Zeros are added to the definition of s_2 , in Equation (4.67), in order to guarantee the one-sided approximation.

The eigenvalues obtained for the first flux vector by using Equation (4.67) become $(-c, 0, 0, +c)$; two symmetric isentropic waves, and two stationary contact waves. Then the first flux vector is written using Equation (4.65) as follows;

$$\vec{f}_1 = \begin{bmatrix} 0 \\ p \\ 0 \\ \rho u \end{bmatrix} = \frac{1}{2} \begin{bmatrix} 0 \\ p_L + p_R \\ 0 \\ p_L u_L + p_R u_R \end{bmatrix} + \delta \bar{Q} \quad (4.70)$$

The first flux vector is evaluated using the Steger-Warming approach [17]. Equation (4.30) is used to obtain the above definition. The second term on the right hand side of Equation (4.70) is the artificial viscosity, and it is expressed as;

$$\delta \bar{Q} = \frac{1}{2\bar{c}} \begin{bmatrix} p_L - p_R \\ (\rho u)_L - (\rho u)_R \\ (\rho v)_L - (\rho v)_R \\ \frac{\bar{c}^{-2}}{\gamma - 1} (p_L - p_R) + \frac{1}{2} [(\rho q^2)_L - (\rho q^2)_R] \end{bmatrix} \quad (4.71)$$

where $q^2 = u^2 + v^2$, \bar{c} is the average of sound speeds and defined as $\bar{c} = \frac{1}{2}(c_L + c_R)$.

Having defined the first flux term, the second term is left. The second flux term has unidirectional eigenvalues, $(0, c, c, 2c)$ when $s_1 > 0$ and $(-2c, -c, -c, 0)$ when $s_1 \leq 0$. Using one-side differencing, the second flux term is obtained.

$$\vec{f}_2 = (u^\alpha - s_2) \begin{bmatrix} \rho \\ \rho u \\ \rho v \\ E \end{bmatrix}^\alpha + \begin{bmatrix} 0 \\ p \\ 0 \\ \rho u \end{bmatrix}^\alpha \quad (4.72)$$

α defines the direction where the information will be taken.

$$\alpha = \begin{cases} L & \text{for } s_1 > 0 \\ R & \text{for } s_1 \leq 0 \end{cases} \quad (4.73)$$

Using Equations (4.71), (4.72) and (4.64), the flux term is obtained as follows:

$$\begin{aligned} \vec{f} = M & \left(\frac{1}{2} \begin{bmatrix} 0 \\ p_L + p_R \\ 0 \\ p_L u_L + p_R u_R \end{bmatrix} + \frac{1}{2c} \begin{bmatrix} p_L - p_R \\ (pu)_L - (pu)_R \\ (pv)_L - (pv)_R \\ \frac{c^{-2}}{\gamma - 1} (p_L - p_R) + \frac{1}{2} [(pq^2)_L - (pq^2)_R] \end{bmatrix} \right) \\ & + (1 - M) \left((u^\alpha - s_2) \begin{bmatrix} \rho \\ \rho u \\ \rho v \\ E \end{bmatrix}^\alpha + \begin{bmatrix} 0 \\ p \\ 0 \\ pu \end{bmatrix}^\alpha \right) \end{aligned} \quad (4.74)$$

The flux in the y -direction, \vec{g} , can be obtained in a similar way.

4.2.2 Flux Difference Splitting

Flux vector splitting schemes presented in the previous section transport the particles according to the characteristic information. Dick [40] states that the flux vector splitting schemes have some shortcomings in the discontinuous shock regions. The appearance of the so-called undifferenced terms in the conservative formulation causes oscillations in the vicinity of shock waves.

The solution of Riemann problem and Godunov's approach are the basis of the flux difference splitting schemes. Splitting the difference flux vectors instead of the flux vectors themselves is a remedy for the shock oscillations. Flux difference splitting schemes take the waves into consideration instead of the direction of the waves. [3, 18]

The exact solution of the Riemann problem is a very tedious calculation. The approximate Riemann solvers like the ones developed by Roe [38] and Osher [39], reduces the computational effort. The Roe's approximate Riemann solver resolves the boundary layers with a high accuracy in addition to its accuracy in handling the shock regions.

Firstly, the Riemann problem and the Godunov approach will be introduced in this section, which are basis of the Roe's approximate Riemann solver. The section will be finalized with the presentation of the Roe's approximate Riemann solver.

4.2.2.1 Riemann Problem or Shock Tube Problem

The Riemann problem is the simplest possible initial value problem for hyperbolic systems, and non-linear superposition of local Riemann problems lead to the solution of the general initial value problem.

The Riemann problem at the point (x_0, y_0) at time t_0 , for the one-dimensional Euler equations is governed by the following equation

$$\frac{\partial \bar{Q}}{\partial t} + \frac{\partial \bar{F}}{\partial x} = 0 \quad (4.75)$$

by the initial conditions stated as:

$$\bar{Q}(x, t_0) = \begin{cases} \bar{Q}_L & \text{if } x < x_0 \\ \bar{Q}_R & \text{if } x > x_0 \end{cases} \quad (4.76)$$

In case of Euler equations, Riemann problem is best experienced in a flow field called the shock tube. If the viscous effects are neglected and an infinitely long tube is taken into consideration, the flow characteristics of the shock tube represents the exact solution of the Euler equations consisting of a combination

of three wave types: shocks, expansion waves, and contact discontinuities. [3]

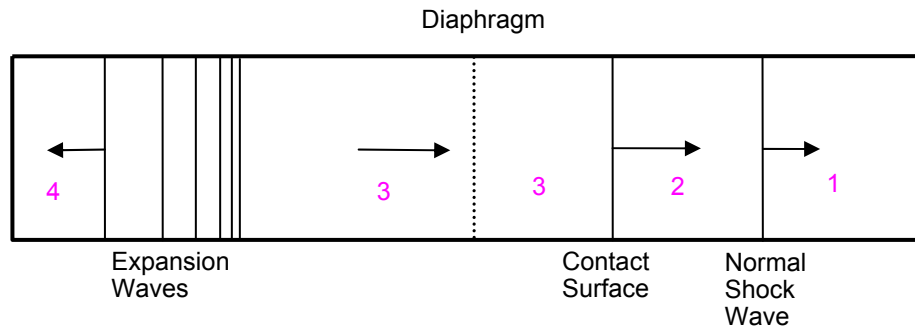


Figure 4.1 Shock Tube

The shock tube shown in Figure 4.1 is initially divided into two regions, which are filled with the same gas in two different physical states, divided by the diaphragm, shown with dotted lines in the figure. The fluid in the tube is initially at rest, and the left hand side of the diaphragm is at a higher pressure than the right hand side. After the sudden rupture of the diaphragm, expansion waves move to the high-pressure side in order to decrease the pressure; and a normal shock wave moves to the low-pressure side to increase the pressure. A contact surface is formed between the normal shock wave and the tail of the expansion waves. [3, 18, 62, 64]

Although the fluid is at the same pressure and moves with the same velocity in regions 2 and 3, there are discontinuities in the temperature and density. The temperature in region 3 is lower than in region 2, since expansion waves cool the fluid in region 3. Hence, the temperature in region 4 is higher than the temperature in region 3. While pressure and temperature vary discontinuously across the normal shock wave, they vary continuously across the expansion waves. The fluid properties in the tube before the rupture determine the strength of the shock wave and the velocities of the fluid in regions 2 and 3. [3, 18, 62, 64]

The exact solution of the shock tube problem requires writing the flow relations

between regions 1 and 4 across the expansion waves, contact discontinuity and the normal shock wave. Further information about the exact solution can be found in [18] and [3].

4.2.2.2 Godunov Approach

Finite difference formulations assume that the functions are sufficiently smooth, continuous and continuously differentiable at the order of accuracy. This assumption is not true when discontinuities like shock waves are present in the flow field. Godunov has suggested a finite volume method to overcome this problem by handling the flow field by evaluating the fluxes by the solution of Riemann problem. [3, 18, 64]

Godunov recommended representing the solution in the flow field by adding up the local exact solutions to the Euler equations. The method considers the solution to be constant over a cell at a fixed time, t , as shown in Figure 4.2. The cell interfaces are assumed to be separating the fluid at different states, like the diaphragm in the shock tube. The flow properties at the next time step are evaluated by the wave interaction at the cell interfaces of the adjacent cells. [3, 18, 64]

As stated in the previous subsection, the general solution of the shock tube problem consists of an expansion wave, a contact discontinuity and a normal shock wave. Each of these waves carries information in the upwind direction. In order to clarify this, suppose that the wave directions are as shown in Figure 4.3. The updated value at the next time step, $t+\Delta t$, is calculated by the information carried from the upstream cell of the expansion wave, $(i+1, j)$ and the information carried from the upstream cell of the normal shock wave, $(i-1, j)$. The use of this methodology makes the time step, Δt , over which the waves are allowed to propagate, important. Time step, Δt , should be limited by the condition that the adjacent Riemann problems do not interfere. [3, 18, 64]

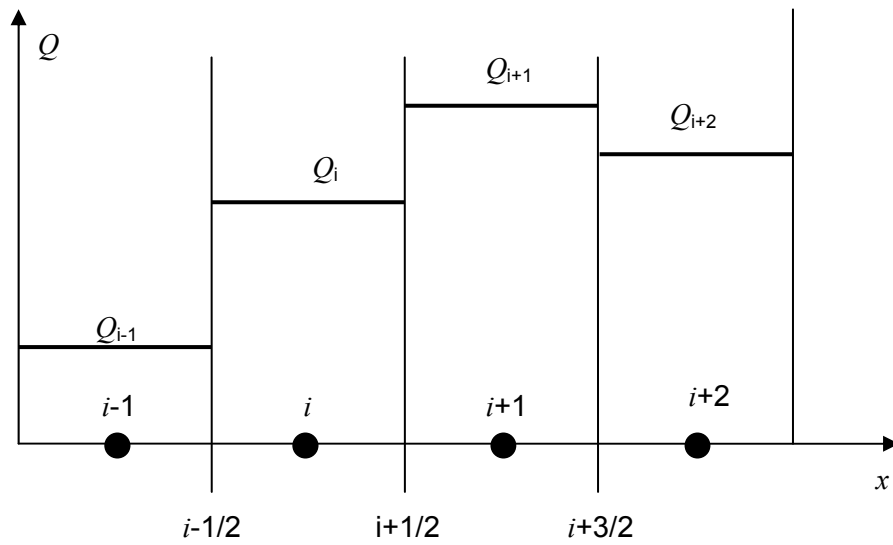


Figure 4.2 Piecewise constant distribution

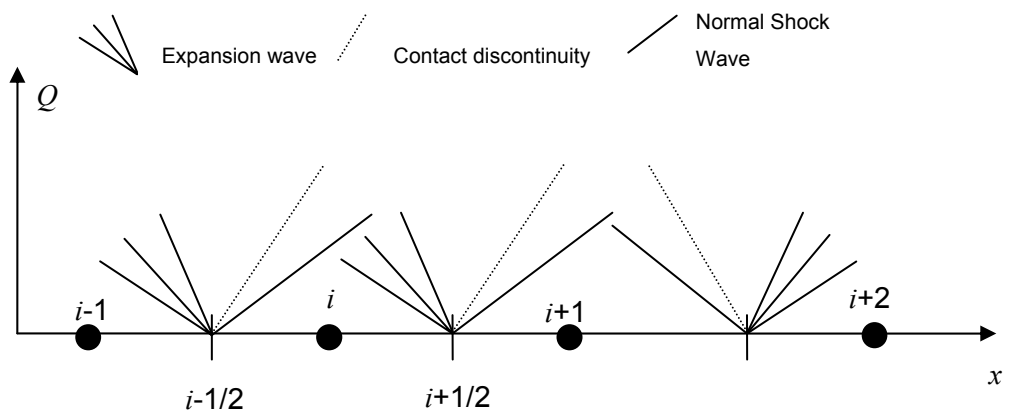


Figure 4.3 Exact solution of Riemann problem at cell interfaces

4.2.2.3 Roe's Approximate Solver

As stated previously, obtaining the exact solution of Riemann problem is costly and approximate solvers are preferred. The most well-known of all approximate Riemann solvers is Roe's approximate solver, which was first presented in 1981. [38]

The solution of Roe's approximate Riemann solver is based on solving a localized Riemann problem to calculate the flux at a given face of the domain. The solver approximates the nonlinear Riemann problem by a linear problem. The linear approximation is written as [18]

$$\frac{\partial \bar{Q}}{\partial t} + [\hat{a}] \cdot \bar{\nabla} \bar{Q} = 0 \quad (4.77)$$

The Jacobian matrix [a] is replaced with $[\hat{a}]$ which should satisfy some properties presented in [18], and the components of the Jacobian are evaluated using the averaged values of \bar{Q} at the interface separating two regions, which is indicated by [18]

$$[\hat{a}] = [\hat{a}(Q_L, Q_R)] \quad (4.78)$$

For a flow moving from left to right, a positive sense flux will also move from left to right. A negative sense flux will move from right to left. Thus, to preserve proper upwind stenciling, a variable or flux term from the left should be stenciled from the left, and a variable or flux from the right should be evaluated using points from the right. Thus, the term "left", "+" and "right", "-" can be used interchangeably.

Looking from another perspective to the Roe's approximate Riemann solver, the direct evaluation of the Jacobian is not necessary. The solution to the equation set changes only across one of the waves presented in Section 4.2.2.2, the solution of the Euler equations at any point in space and time can be represented by a summation of the state to the extreme left or right of the space, plus (or minus) one or more of the state changes across these waves. [19] The method De Zeeuw and Powell [57] presented is used in this study and will be explained.

The flux across a face is represented in Equation (3.9) as:

$$\sum_{k=1}^4 \vec{F}_{I,J_k} \cdot \vec{S}_{I,J_k} \quad (4.79)$$

The flux can be rewritten as

$$\sum_{k=1}^4 \vec{F}_{I,J_k} \cdot \vec{S}_{I,J_k} = \sum_{k=1}^4 \left(\vec{f}_{I,J_k} \Delta y_{I,J_k} - \vec{g}_{I,J_k} \Delta x_{I,J_k} \right) \quad (4.80)$$

Using the concept that Laney [19] introduced, Equation (4.80) is expressed as, for a specific face in the solution domain

$$\left(\vec{f} \Delta y - \vec{g} \Delta x \right) = \begin{pmatrix} \rho u_n \\ \rho u_n u + p \frac{\Delta y}{\Delta S} \\ \rho u_n v - p \frac{\Delta x}{\Delta S} \\ \rho u_n H \end{pmatrix} \Delta S \equiv \Phi \Delta S \quad (4.81)$$

The convective flux through a specific face in the solution domain is a function of the variables at both sides of that face, in other words right and left state variables are needed to calculate the convective flux across a face. The convective flux across a face using the Roe's approximate Riemann solver is expressed as [57]

$$\Phi(\bar{Q}_L, \bar{Q}_R) = \frac{1}{2} \left[\Phi(\bar{Q}_L) + \Phi(\bar{Q}_R) \right] - \frac{1}{2} \sum_{m=1}^4 \left| \hat{a}_m \right|^* \Delta V_m \hat{R}_m \quad (4.82)$$

where

$$\hat{\mathbf{a}}_m = \begin{bmatrix} \hat{\mathbf{u}}_n - \hat{c} \\ \hat{\mathbf{u}}_n \\ \hat{\mathbf{u}}_n \\ \hat{\mathbf{u}}_n + \hat{c} \end{bmatrix}_m \quad (4.83)$$

$$\Delta V_m = \begin{bmatrix} \frac{\Delta p - \hat{\rho} \hat{c} \Delta u_n}{2 \hat{c}^2} \\ \frac{\hat{\rho} \Delta u_t}{\hat{c}} \\ \Delta \rho - \frac{\Delta p}{\hat{c}^2} \\ \frac{\Delta p + \hat{\rho} \hat{c} \Delta u_n}{2 \hat{c}^2} \end{bmatrix}_m \quad (4.84)$$

$$\hat{\mathbf{R}}_m = \begin{bmatrix} 1 & 0 & 1 & 1 \\ \hat{u} - \hat{c} \frac{\Delta y}{\Delta S} & \hat{c} \frac{\Delta x}{\Delta S} & \hat{u} & \hat{u} + \hat{c} \frac{\Delta y}{\Delta S} \\ \hat{v} + \hat{c} \frac{\Delta x}{\Delta S} & \hat{c} \frac{\Delta y}{\Delta S} & \hat{v} & \hat{v} - \hat{c} \frac{\Delta x}{\Delta S} \\ H - \hat{u}_n \hat{c} & \hat{u}_t \hat{c} & \frac{\hat{u}^2 + \hat{v}^2}{2} & H + \hat{u}_n \hat{c} \end{bmatrix}_m \quad (4.85)$$

where u_n and u_t are normal and tangential velocities, respectively. Variables in the above equations which have cap are defined as follows.

$$\begin{aligned} \hat{\rho} &= \sqrt{\rho_L \rho_R} \\ \hat{u} &= \frac{\sqrt{\rho_L} u_L + \sqrt{\rho_R} u_R}{\sqrt{\rho_L} + \sqrt{\rho_R}} \\ \hat{v} &= \frac{\sqrt{\rho_L} v_L + \sqrt{\rho_R} v_R}{\sqrt{\rho_L} + \sqrt{\rho_R}} \\ \hat{H} &= \frac{\sqrt{\rho_L} H_L + \sqrt{\rho_R} H_R}{\sqrt{\rho_L} + \sqrt{\rho_R}} \end{aligned} \quad (4.86)$$

The other variables \hat{c} , \hat{u}_n and \hat{u}_t are calculated using the above variables. [57]

As De Zeeuw and Powell stated in [57] nonphysical expansion shocks are prevented by imposing a condition called entropy fix. Entropy fix is imposed on the solver of Roe's approximate Riemann solver by smoothing the $|\hat{a}_m|$ for the two acoustic waves given with $m=1$ and 4 and replacing with $|\hat{a}_m|^*$, which is defined as [57]

$$|\hat{a}_m|^* = \begin{cases} |\hat{a}_m|, & |\hat{a}_m| \geq \frac{1}{2} \delta a_m \\ \frac{(\hat{a}_m)^2}{\delta a_m} + \frac{1}{4} \delta a_m, & |\hat{a}_m| \leq \frac{1}{2} \delta a_m \end{cases} \quad (4.87)$$

where

$$\delta a_m = \max(4\Delta a_m, 0) \quad , \quad \Delta a_m = a_{m_R} - a_{m_L} \quad (4.88)$$

4.3 Solution Reconstruction

The flux evaluation schemes introduced in Sections 4.1 and 4.2 require the cell center data to be extrapolated to the face of the control volume. The left-right states declared in AUSM, AUFS and Roe's schemes and positive-negative states used in Steger-Warming's and Van-Leer's schemes are calculated using the reconstruction techniques. Although different names are used, the positive and left states have the same physical meaning. For a positive velocity (in the positive x direction), information is taken from the upwind cell. When the flux at the right face of a cell is calculated, the first upwind cell is the cell in consideration. With a different approach, the first cell in the left of a face (again the right face of the cell is taken into account) is the cell in consideration. Similarly, the negative and right states represent the same physical meaning.

If the solution in a control volume is assumed to be constant, the procedure to

obtain the left and right states is very straightforward. For positive velocity at the face of the control volume, the reconstructed conservative variables are expressed as;

$$\begin{aligned}\bar{Q}_L &= \bar{Q}_I \\ \bar{Q}_R &= \bar{Q}_{I+1}\end{aligned}\tag{4.89}$$

Equation (4.89) represents the first-order accurate upwind discretisation. For higher-order spatial accuracy, more upwind points should be introduced to the schemes. Van Leer suggested to use piecewise linear data distribution instead of piecewise constant data distribution to construct fluxes from the flux evaluation schemes. [46] Van Leer's, Monotone Upstream-Centered Schemes for Conservation Laws (MUSCL) is a widely used method, which is at first introduced for uniform structured grids. MUSCL interpolation is actually a brand name for a whole type of reconstruction methods, and all the variations of the method invented after the original work, are referred to as "MUSCL". MUSCL scheme determines the conserved variables at the cell faces by an upwind-biased interpolation. The scheme gives second-order accurate results if the data is assumed to be piecewise-linear and higher-order results if the data is assumed to be piecewise-polynomials of orders higher than two over the control volume. The scheme is used in many researches and yields accurate and stable results. [20]

The original form of MUSCL scheme is not used in this study since body-fitted structured grid is used to mesh the domain. MUSCL scheme can be derived by using the Taylor series expansion. When using Taylor series expansion distances between two adjacent cell centers, and distance between the cell center and cell face come into scene. In uniform structured grids, cells are equally spaced and the distances in consideration cancel each other in the equation. For a body-fitted structured grid, however, cells are not equally spaced. Because of this fact, a compact equation like the MUSCL equation can not be obtained for unstructured or body-fitted structured meshes.

Due to this deficiency of the original MUSCL scheme, there exist extensions for unstructured and body-fitted structured meshes in the literature. [6, 51] One way of adapting the original MUSCL scheme to unstructured and body-fitted structured grids needs phantom cell centers to be introduced. These phantom cell centers are defined to be located at a distance equal to the original cell center-face distance, to the cell face. By introducing these phantom cells, grid like the uniform-structured is obtained, and the original MUSCL equations can be used. This technique may cause difficulties at the boundaries due to the phantom cells outside the boundaries and needs too many data to be stored for each cell. [6]

Barth and Jespersen presented a linear reconstruction scheme for unstructured flow solvers. This method achieves second-order accuracy by extrapolating from the center of the control volume to the face using the value and the gradient at the center. [54] Although the technique is verified for triangular control volumes and cell-centered schemes in [54], it is extended to arbitrary meshes and schemes. [6, 51] For a cell-centered, body fitted structured scheme, shown in Figure 3.3, the reconstructed conservative variables for positive velocity, are expressed as;

$$\begin{aligned}\bar{Q}_L &= \bar{Q}_{I,J} + \psi_{I,J} \left(\nabla \bar{Q}_{I,J} \cdot \vec{r}_L \right) \\ \bar{Q}_R &= \bar{Q}_{I+1,J} + \psi_{I+1,J} \left(\nabla \bar{Q}_{I+1,J} \cdot \vec{r}_R \right)\end{aligned}\tag{4.90}$$

$\psi_{I,J}$, in Equation (4.90) represents the limiter function, that should be used to eliminate the oscillations near discontinuities. $\nabla \bar{Q}_{I,J}$ is the gradient at the cell center (I,J) and its derivation is presented below. \vec{r}_L and \vec{r}_R are the vectors directing from the cell center to the midpoint of the cell face as shown in Figure 4.4.

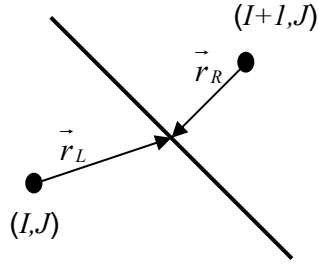


Figure 4.4: Typical face and cell-center within a body-fitted structured grid

The gradient, $\nabla \bar{Q}_{I,J}$, at the cell center of a control volume can be expressed by the Green-Gauss theorem or the least squares approach. The former method is used in this study. Green-Gauss theorem states that the surface integral of a function is equal to the volume integral (over the volume bound by the surface) of the gradient of the function.

$$\int_{\Omega} \nabla \bar{Q}_{I,J} d\Omega = \oint_S \bar{Q}_{I,J} \vec{dS} \quad (4.91)$$

Since $\nabla \bar{Q}_{I,J}$ is assumed to be constant over the control volume, Equation (4.91) can be rewritten as;

$$\nabla \bar{Q}_{I,J} = \frac{1}{\Omega_{I,J}} \oint_S \bar{Q}_{I,J} \vec{dS} \quad (4.92)$$

Finally, the integral over the surface is approximated as a summation of the value times the surface vector.

$$\nabla \bar{Q}_{I,J} = \frac{1}{\Omega_{I,J}} \sum_{k=1}^4 \frac{1}{2} (\bar{Q}_{I,J} + \bar{Q}_{IN,JN}) \cdot \vec{S}_{I,J,k} \quad (4.93)$$

$\bar{Q}_{IN,JN}$ represents the value of the corresponding variable at the corresponding

neighboring cell in Equation (4.93). All the terms in Equation (4.90) are defined except the limiter term, $\psi_{I,J}$. Limiters are described in the next section.

4.4 Limiters

Limiters are used in high resolution schemes with discontinuous solutions. Limiters damp oscillations due to shocks, sharp changes in the solution and maintain monotonicity. Monotonicity preserving solutions satisfy the following conditions

1. maxima is non-increasing
2. minima non-decreasing
3. no new extrema should be created

Limiters suppress oscillations at the cost of reducing accuracy when multidimensional unstructured grids are considered. [56]

Limiter functions are forced to be greater than or equal to zero. The limiter is equal to zero in the region of high gradients and maintain first-order scheme. It means that the second-order reconstruction represented in Equation (4.90) reduces to Equation (4.89). On the other hand, the limiter term is set to one in smooth flow regions and maintain fully second-order scheme meaning that no limiting is applied to the reconstruction method.

There are a variety of limiters presented in the literature. Most of the limiters developed are for one-dimensional flow governed by uniform grids. There exist fewer extensions to multi-dimensions and non-uniform grids. The multidimensional slope limiter developed by Hubbard [48] for unstructured grids is used in this study. This limiter constructs a “maximum principle region” for each cell in which the gradient defined by Equation (4.93) must lie. The “maximum

principle region" limits the gradient operator by [48]

$$\min\left[(Q_{neigh} - Q_{cell}), 0\right] \leq (\nabla \bar{Q}_{I,J} \cdot \vec{r}_L) \leq \max\left[(Q_{neigh} - Q_{cell}), 0\right] \quad (4.94)$$

The limiter function, by using the definition of the "maximum principle region", is expressed as [48]

$$\alpha^k = \begin{cases} \frac{\max\left[(Q_{neigh} - Q_{cell}), 0\right]}{\nabla \bar{Q}_{I,J} \cdot \vec{r}_L} & \text{if } \nabla \bar{Q}_{I,J} \cdot \vec{r}_L > \max\left[(Q_{neigh} - Q_{cell}), 0\right] \\ \frac{\min\left[(Q_{neigh} - Q_{cell}), 0\right]}{\nabla \bar{Q}_{I,J} \cdot \vec{r}_L} & \text{if } \nabla \bar{Q}_{I,J} \cdot \vec{r}_L < \min\left[(Q_{neigh} - Q_{cell}), 0\right] \\ 0 & \text{otherwise} \end{cases} \quad (4.95)$$

$$\psi_{I,J} = \min(\alpha^k)$$

CHAPTER 5

RESULTS AND DISCUSSION

The flux splitting schemes based on various methods for handling the flux terms in Euler equations presented in Chapter 4 are tested here for a variety of flow regimes.

External flow over a NACA0012 airfoil is used with varying freestream Mach numbers and angle of attacks. Boundary condition based on ghost cell logic is used which is explained in Chapter 3. The farfield boundary is handled by assigning the freestream values, which is not based on method of characteristics. Using characteristic boundary conditions is known to yield less radius of computational domain. In order to eliminate the risk of reaching the disturbances to the freestream, the radius of computational domain is taken to be 20 chord lengths from the mid-chord. All the cases are initialized with the freestream conditions of the stagnation temperature and pressure of 350 K and 150 kPa, respectively. Schemes presented herein, are tested using fine as well as coarse meshes for showing the grid independency of the methods.

The most widely used channel which has a circular arc on the lower boundary is selected to investigate the behavior of the flux splitting methods in internal flow. Two different channel geometries are taken into consideration for subsonic-transonic flows and supersonic flow as in [60]. Solid wall boundary condition explained in Chapter 3 is implemented for lower and upper boundaries, whereas farfield boundary conditions are used for inlet and outlet regions. As in the external flow case the flow is initialized using the freestream conditions with the stagnation temperature and pressure of 350 K and 150 kPa, respectively.

Subsonic, transonic and supersonic flows are tested, and compared with the experimental data and the numerical results presented in the literature. The same test cases are used for second order calculations for external flow, and the results are discussed. Finally, convergence times for each flux splitting method are compared. The calculation of residuals is given in Appendix A in detail.

5.1 External Flow

5.1.1 First Order Calculations

5.1.1.1 Subsonic Flow

A subsonic flow case is considered, which has a freestream Mach number of $M_\infty = 0.6$ and an angle of attack $\alpha = 0^\circ$, and the obtained results are compared with the experimental results presented in [65] for all flux-splitting schemes. Due to the symmetry of the airfoil, in addition with the angle of attack being zero, the flow is characterized by the symmetry about the x -axis.

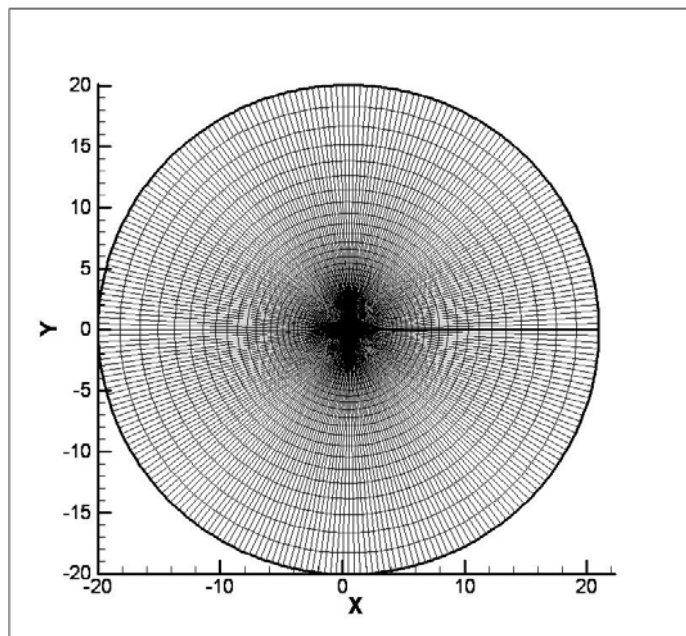


Figure 5.1: 129x65 O-grid over NACA0012 airfoil

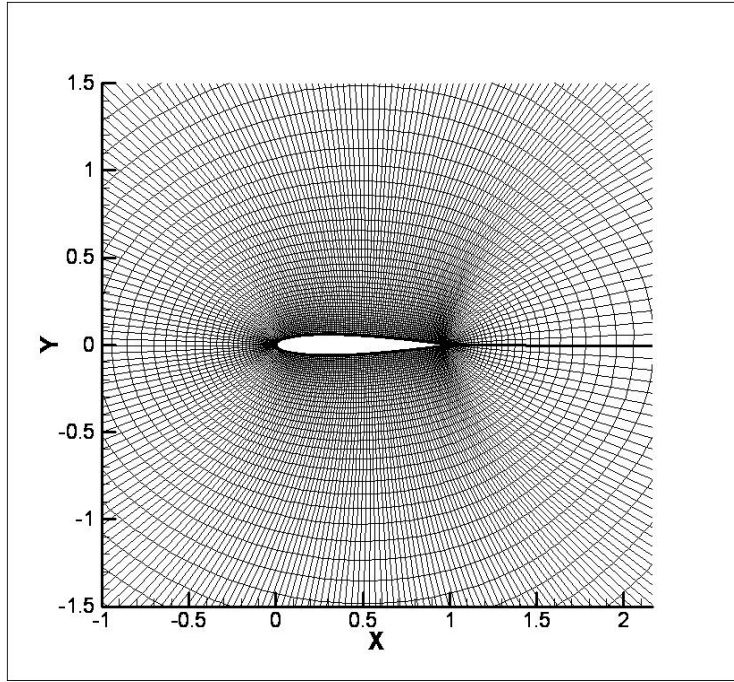


Figure 5.2: Detailed view of 129x65 O-grid over NACA0012 airfoil

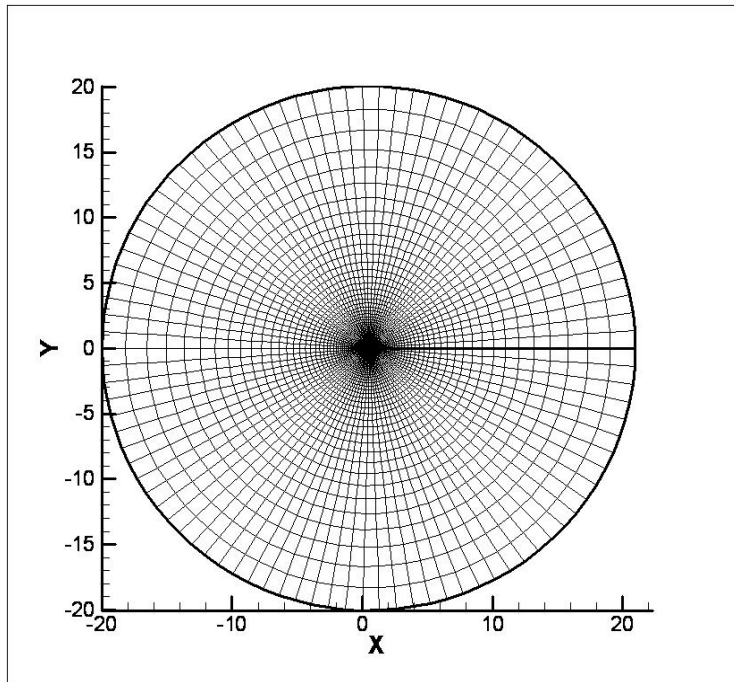


Figure 5.3: 97x65 O-grid over NACA0012 airfoil

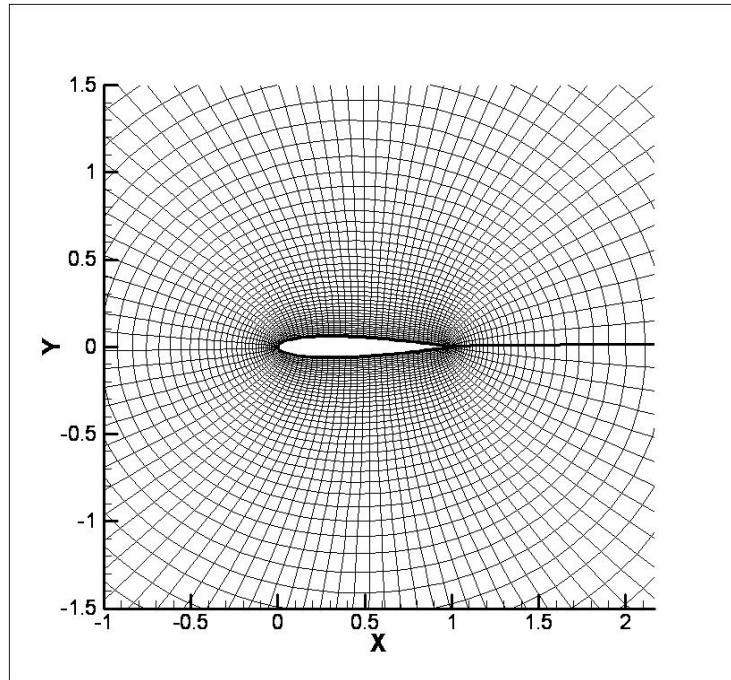


Figure 5.4: Detailed view of 97x65 O-grid over NACA0012 airfoil

The case is tested for three different grids. The first grid consists of 129 nodes on the body and 65 nodes in the direction towards the farfield boundary, giving a total of 8385 grids. The second grid consists of 97 nodes on the body and 65 nodes in the direction normal to the body, giving a total of 6305 cells in the physical domain. The overall and detailed views of the meshes used are shown in Figures 5.1 to 5.4.

The distribution of pressure coefficients C_p for all methods, which are obtained by using the 97x65 O-grid, is shown in Figure 5.6 with the experimental data in [65]. The results obtained by using the 129x65 O-grid is shown in Figure 5.6. It is obvious that the finer (129x65) grid leads more accurate results. Additionally, a finer mesh with having 257x65 cells is used. However using grids finer than 129x65 does not change the accuracy of the solutions, but leads to slower convergence. Thus, 129x65 O-grid is selected and used in the calculations.

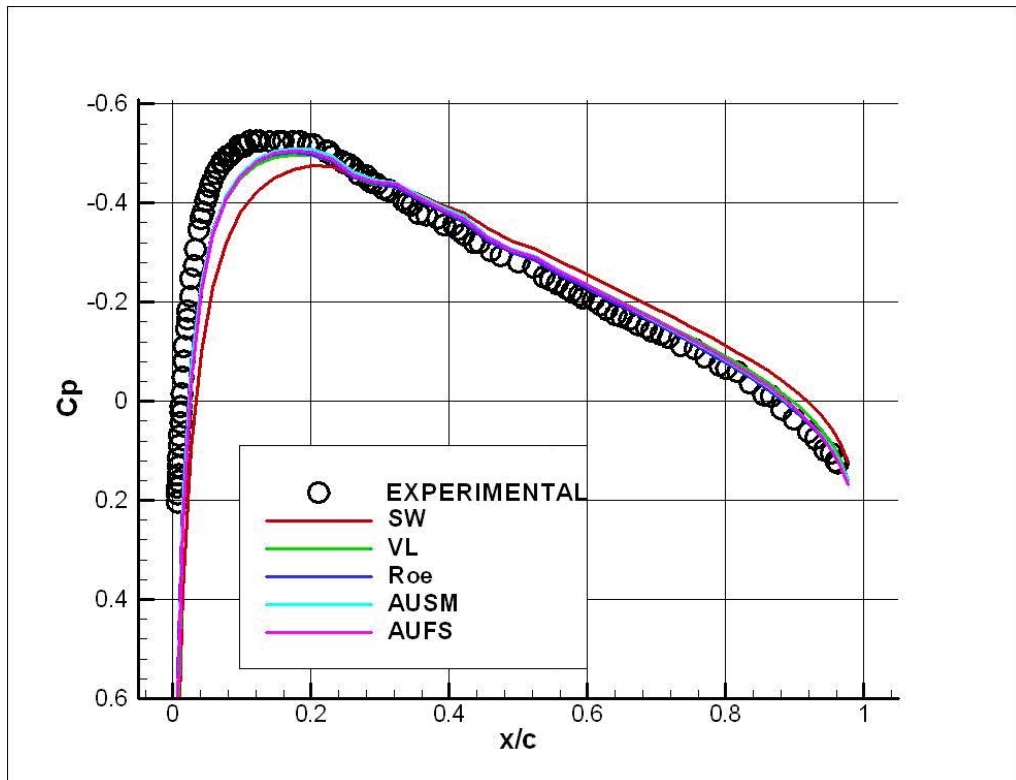


Figure 5.5: Distribution of pressure coefficient over NACA0012 airfoil at $M_\infty = 0.6$ $\alpha = 0^\circ$ using 97x65 O-grid with first-order reconstruction

All the methods examined yield comparable accuracy with the experimental data, as it is seen from Figure 5.6. It can be concluded from the figure that the AUSM scheme gives the most accurate results for the case considered. Although Roe's flux difference splitting scheme has higher accuracy than the Steger-Warming and Van Leer flux vector splitting schemes as expected, the accuracy of the hybrid AUSM scheme cannot be reached. The results agree with the argument that the Steger-Warming flux vector splitting has a very dissipative character, since the peak of pressure coefficient cannot be caught as good as the other schemes in consideration.

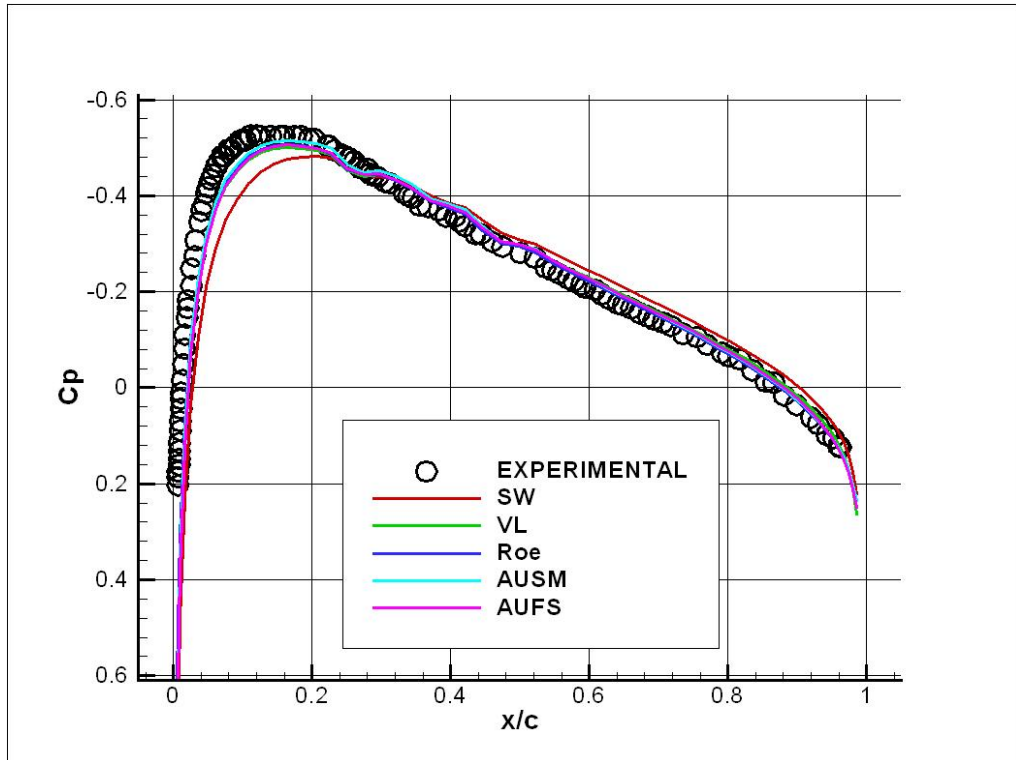


Figure 5.6: Distribution of pressure coefficient over NACA0012 airfoil at $M_\infty = 0.6$ $\alpha = 0^\circ$ using 129x65 O-grid with first-order reconstruction

The convergence history of each method is shown in Figures 5.7 to 5.11. The convergence histories show that AUSM converges faster than the other schemes. Van-Leer flux vector splitting scheme and AUFS converges slower than Steger-Warming flux vector splitting scheme and Roe's flux difference splitting scheme. The convergence speed is related with the CFL number. If the CFL number were the same for all schemes, the results would be different. But the maximum allowable CFL number is defined by characteristics of the scheme and it should be used for the fastest convergence. Maximum allowable CFL numbers for this test case are shown in Table 5.1. Although the given accuracy is reached at more than 2000 iterations, the result is obtained around the 1000th iteration. Generally, the Euler solvers are run for 1000 iterations as stated in the literature.

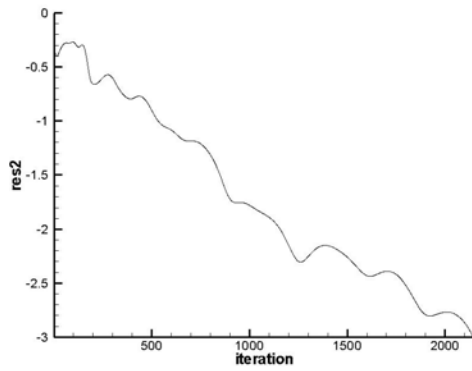


Figure 5.7: Convergence history of Steger-Warming FVS Scheme for first-order subsonic flow using 129x65 O-grid

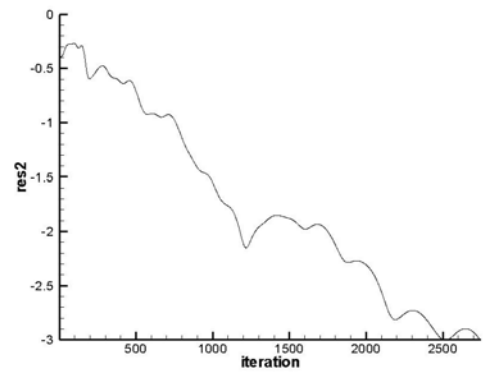


Figure 5.8: Convergence history of Van Leer FVS Scheme for first-order subsonic flow using 129x65 O-grid

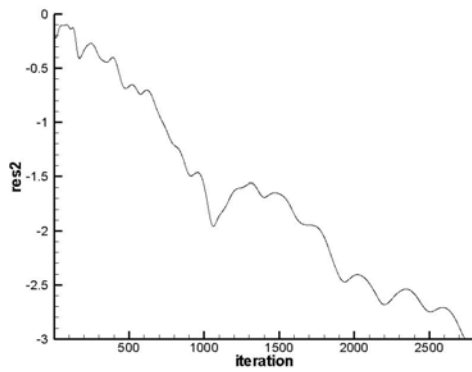


Figure 5.9: Convergence history of AUFS for first-order subsonic flow using 129x65 O-grid

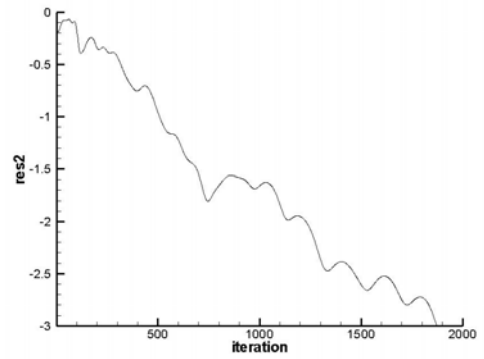


Figure 5.10: Convergence history of AUSM for first-order subsonic flow using 129x65 O-grid

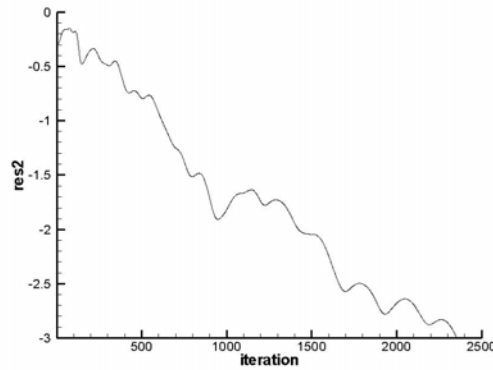


Figure 5.11: Convergence history of Roe's FDS Scheme for first-order subsonic flow using 129x65 O-grid

Table 5.1: Maximum Allowable CFL numbers for $M_\infty = 0.6$ $\alpha = 0^\circ$

	SW FVS	VL FVS	AUSM	AUFS	Roe's FDS
CFL	0.6	0.6	0.99	0.75	0.8

5.1.1.2 Transonic Flow

A transonic flow case is considered having a freestream Mach number of $M_\infty = 0.8$ and an angle of attack $\alpha = 0^\circ$ and the results are compared with the numerical results presented in [66] by Wu and Li. Under the given conditions, a shock appears on both the upper and lower surfaces. The shock is located in the middle of the airfoil. Due to the symmetry of the airfoil and the angle of attack being zero, the shock is symmetric about the x -axis.

The grid used in this test case is adapted according to the shock. Knowing the approximate or exact location of the shock allows the grid to be clustered in the corresponding region. A regular grid may be used to test this case, however, the use of the adapted grid results in sharper shock definitions and increases the convergence speed. The regular grids without shock adaptation should be finer in

order to obtain the same accuracy with the adaptive ones, although it is not needed in the regions without discontinuities. As a result, the convergence time is bound to increase. Thus, shock adapted meshes are preferred when the shock locations can be estimated. The grid used is shown in Figures 5.12 and 5.13.

The distribution of pressure coefficients C_p for all methods is given in Figure 5.14 with the numerical data in [66]. The results are obtained by using the 185x60 O-grid. Figure 5.14 shows that, all the methods used in the calculations except Steger-Warming flux vector splitting method give acceptable results. Roe's flux difference splitting scheme and AUSM serve the best results in the case of shock waves as expected. Although AUSM gives as accurate results as Roe's FDS method for capturing the shock, AUSM could not define the foot of the shock as sharp as Roe's FDS. On the other hand, results obtained by Steger-Warming flux vector splitting scheme are worse than expected. Van-Leer FVS and AUFS give comparable accuracy. Although both of the schemes could not catch the shock exactly, they define the shock in a same number of cells. One advantage of Van-Leer flux vector splitting over AUFS is that it defines the foot of the shock sharper than AUFS.

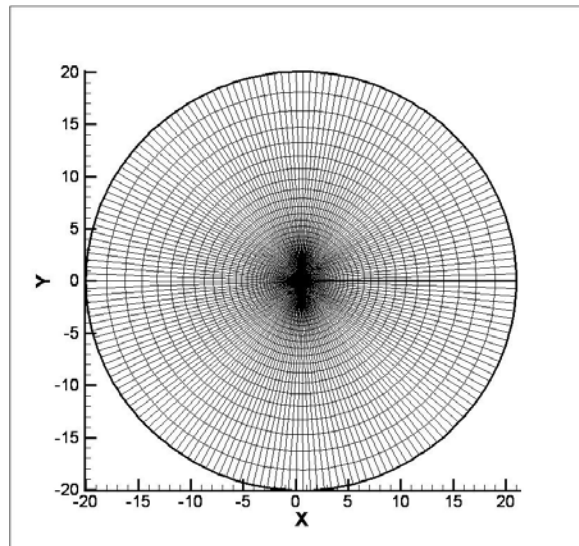


Figure 5.12: 185x60 O-grid over NACA0012 airfoil for $M_\infty = 0.8$ $\alpha = 0^\circ$ flow

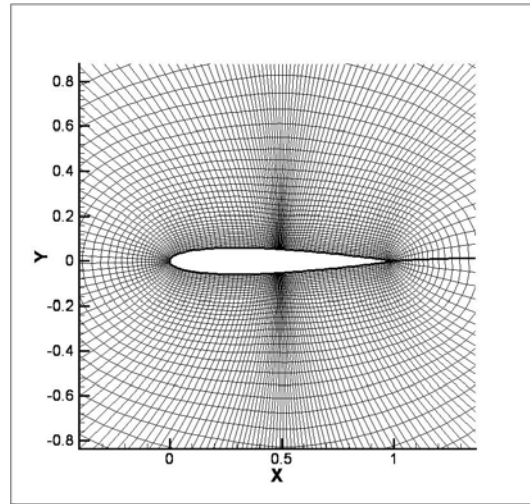


Figure 5.13: Detailed view of 185x60 O-grid over NACA0012 airfoil for $M_\infty = 0.8 \alpha = 0^\circ$ flow

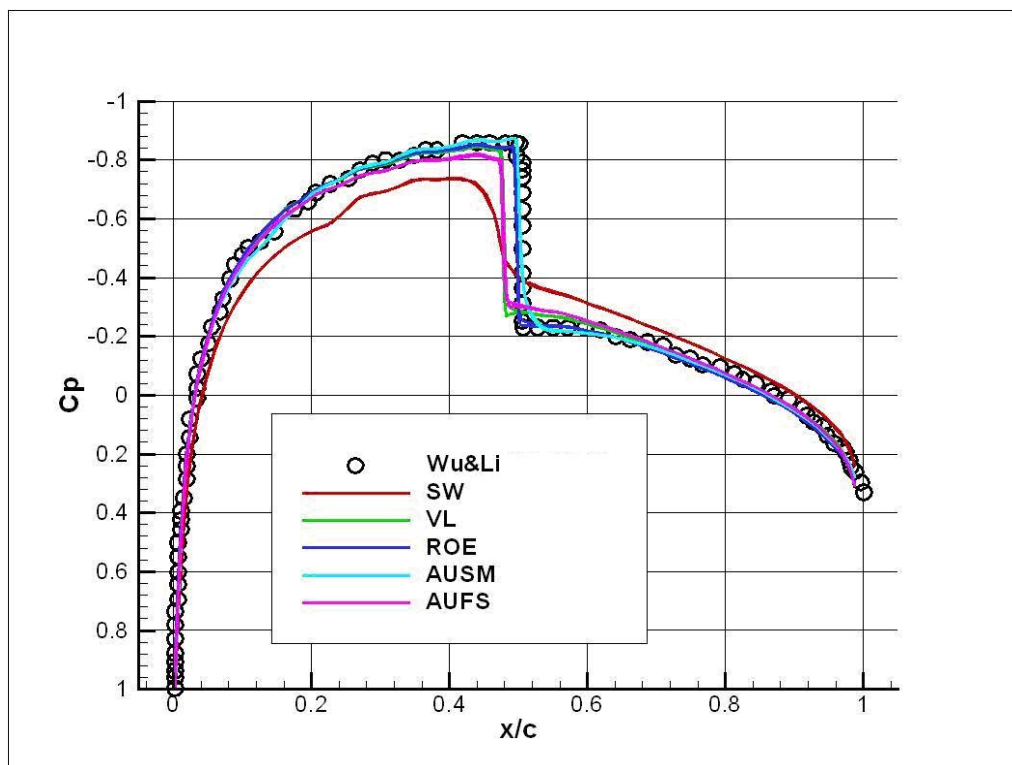


Figure 5.14: Distribution of pressure coefficient over NACA0012 airfoil at $M_\infty = 0.8 \alpha = 0^\circ$ using 185x60 O-grid with first-order reconstruction

Figures 5.15 to 5.19 show the convergence histories of the methods used. As it is observed from the figures, convergence time for AUSM is shorter than the other schemes. CFL number used for AUSM is 0.99, which has a great effect on the convergence time. The maximum allowable time steps taken do not change flow case so the CFL numbers given in Table 5.1 are also valid for this flow case.

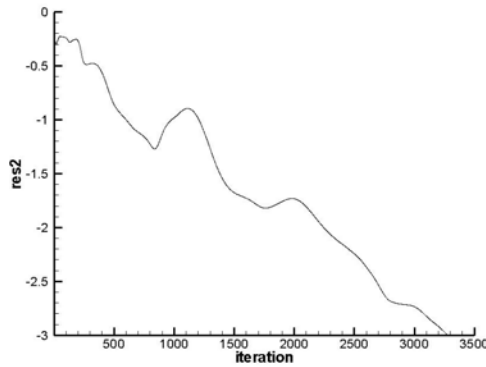


Figure 5.15: Convergence history for Steger-Warming FVS Scheme for first-order transonic flow using 185x60 O-grid

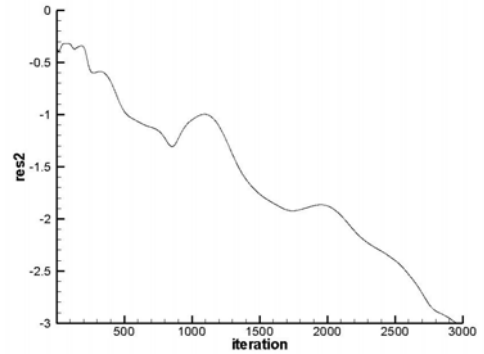


Figure 5.16: Convergence history for Van Leer FVS Scheme for first-order transonic flow using 185x60 O-grid

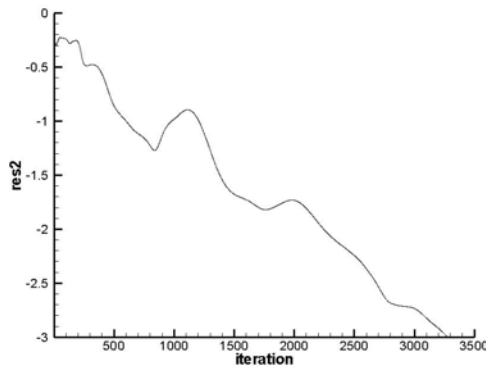


Figure 5.17: Convergence history for AUFS for first-order transonic flow using 185x60 O-grid

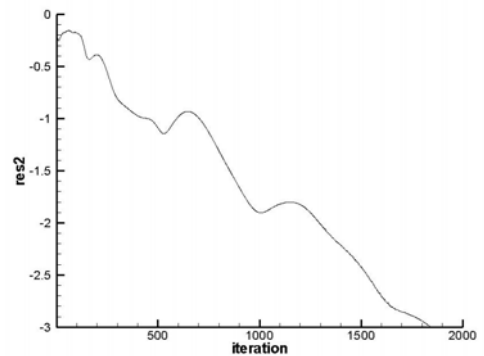


Figure 5.18: Convergence history for AUSM for first-order transonic flow using 185x60 O-grid

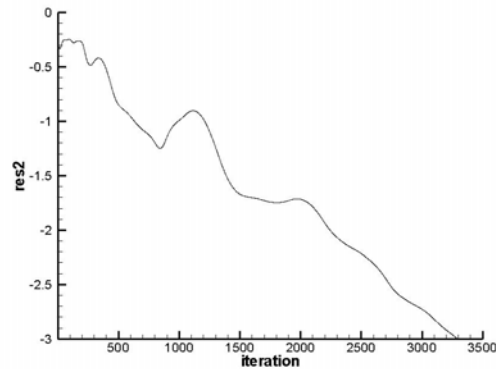


Figure 5.19: Convergence history for Roe's FDS Scheme for first-order transonic flow using 185x60 O-grid

5.1.1.3 Supersonic Flow

A supersonic test case of $M_\infty = 1.2$ at a 0° angle of attack is used. The 129x65 O-grid used in the subsonic flow case is chosen in the solution. The obtained solution is compared with the ones in [22]. This supersonic case is tested in order to investigate the ability of the methods to capture the strong shocks present in the flow.

Pressure contours around NACA0012 airfoil presented by Liou and Steffen [22] by using second-order accurate AUSM is shown in Figure 5.20. The pressure contours obtained by using the methods described in this study are given in Figures 5.21 to 5.25. It can be concluded that all the schemes give almost identical results. Especially, Van Leer FVS scheme and AUFS, likewise AUSM and Roe's FDS scheme gives similar results with each other for the oblique shock wave at the trailing edge. It seems that the bow shock at the leading edge is not captured accurately. This may be due to the order of reconstruction which will be mentioned in the next subsection.

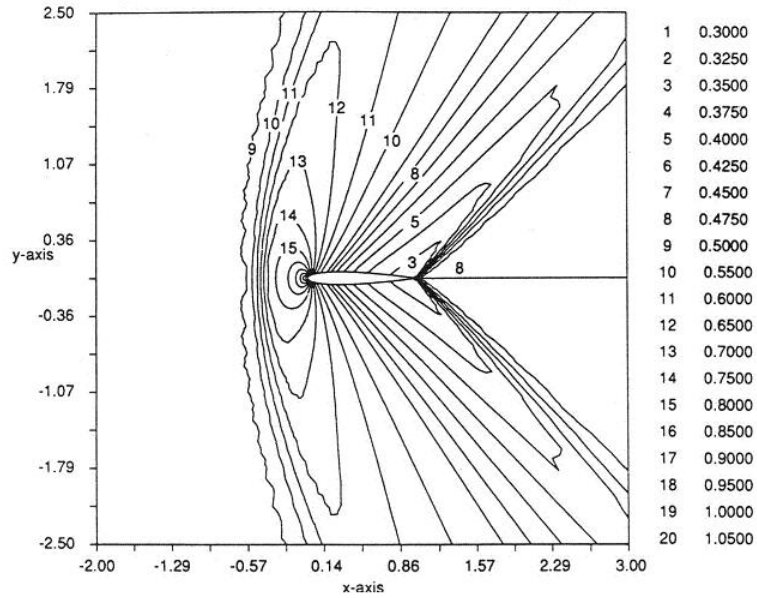


Figure 5.20: Pressure contours around NACA0012 at $M_\infty = 1.2$ $\alpha = 0^\circ$ by AUSM [22]

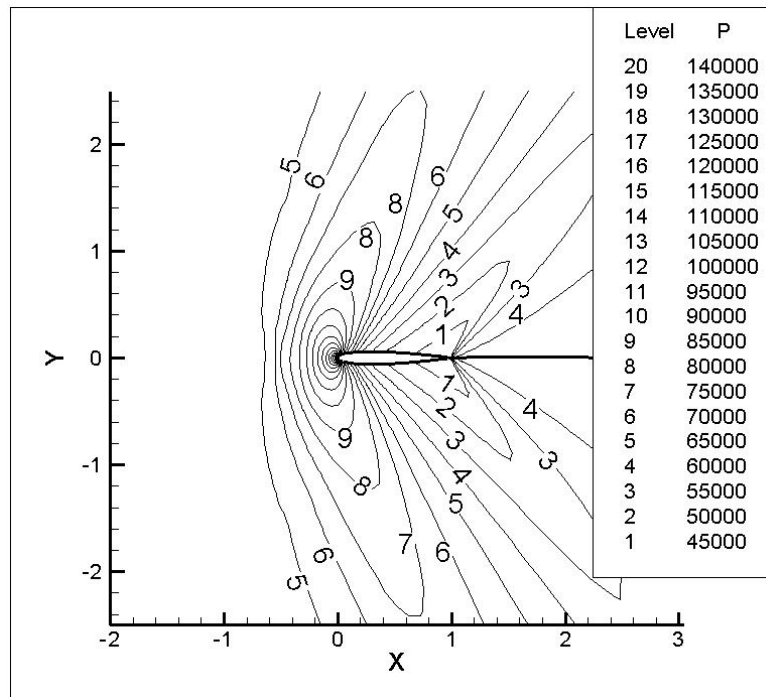


Figure 5.21: Pressure contours around NACA0012 at $M_\infty = 1.2$ $\alpha = 0^\circ$ by Steger-Warming FVS Scheme using 129x65 O-grid with first-order reconstruction

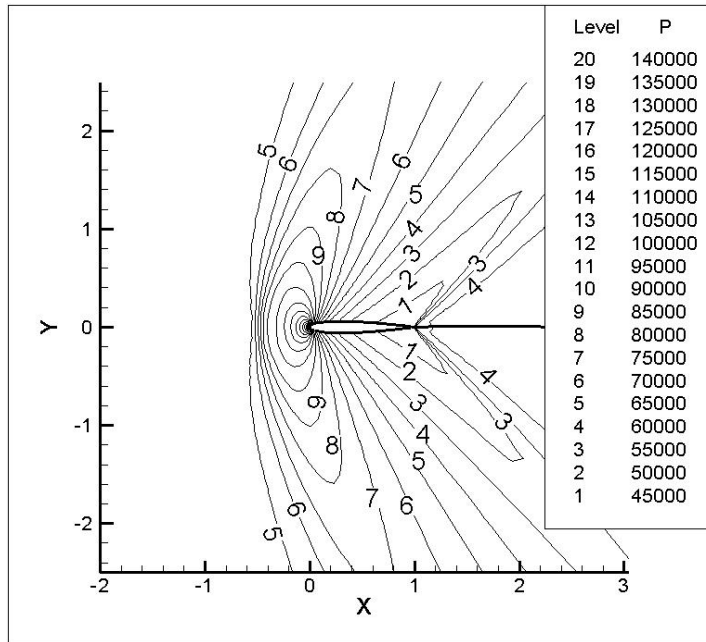


Figure 5.22: Pressure contours around NACA0012 at $M_\infty = 1.2$ $\alpha = 0^\circ$ by Van Leer FVS

Scheme using 129x65 O-grid with first-order reconstruction

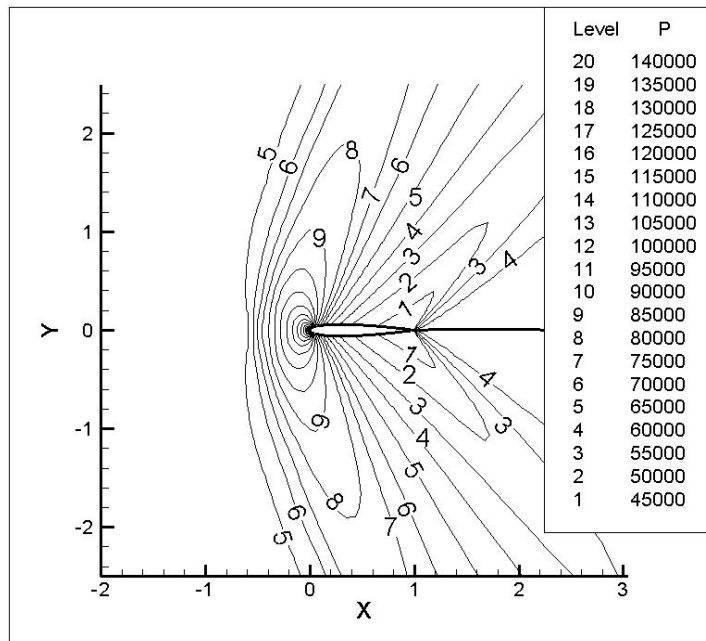


Figure 5.23: Pressure contours around NACA0012 at $M_\infty = 1.2$ $\alpha = 0^\circ$ by AUSM using

129x65 O-grid with first-order reconstruction

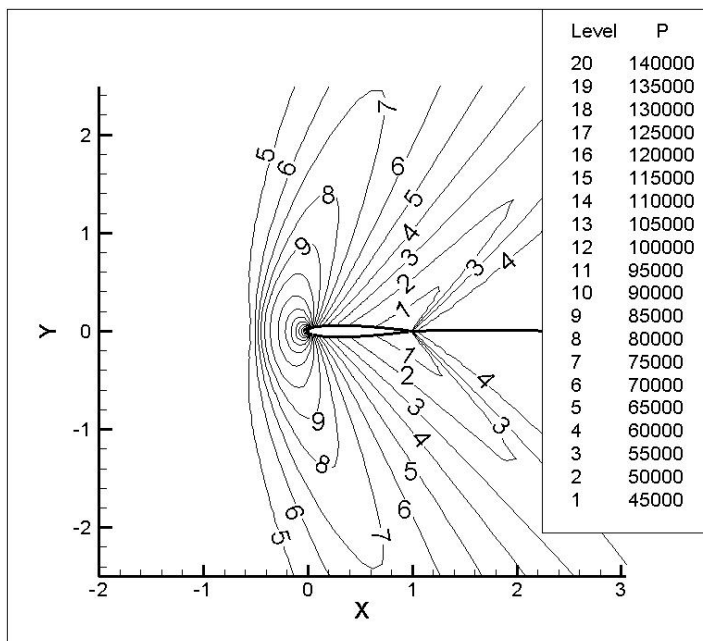


Figure 5.24: Pressure contours around NACA0012 at $M_\infty = 1.2$ $\alpha = 0^\circ$ by AUFS using 129x65 O-grid with first-order reconstruction

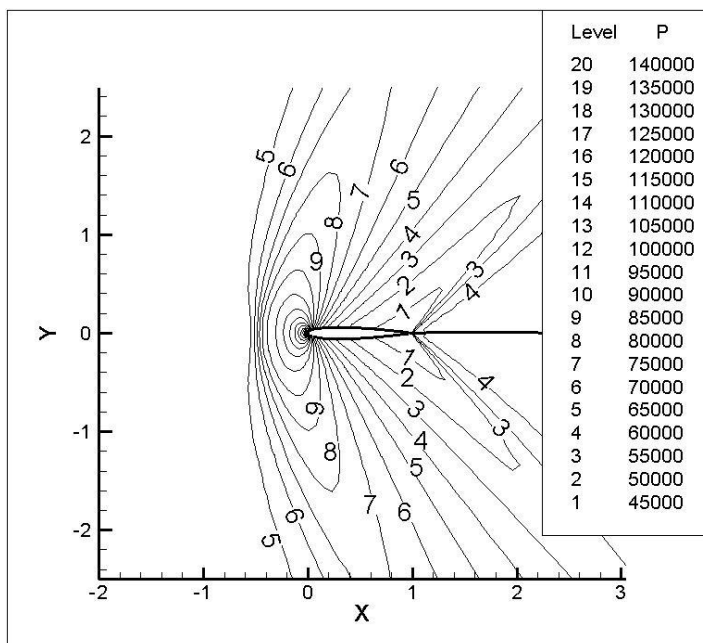


Figure 5.25: Pressure contours around NACA0012 at $M_\infty = 1.2$ $\alpha = 0^\circ$ by Roe's FDS Scheme using 129x65 O-grid with first-order reconstruction

Convergence histories of the used methods are shown in Figures 5.26 to 5.30 for supersonic flow. AUSM, AUFS and Roe's flux difference splitting schemes lead to the fastest convergence.

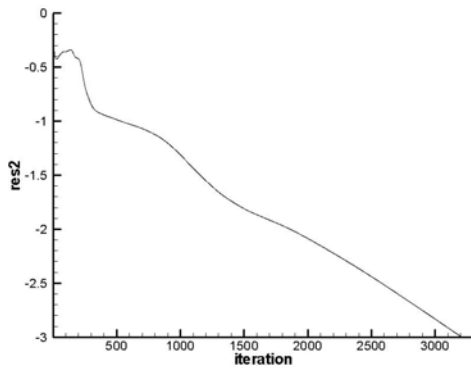


Figure 5.26: Convergence history of Steger-Warming FVS Scheme for first-order supersonic flow using 129x65 O-grid

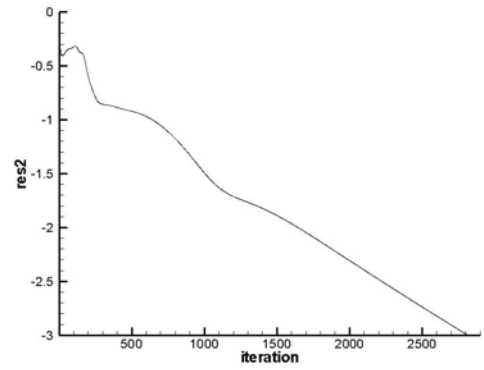


Figure 5.27: Convergence history of Van Leer FVS Scheme for first-order supersonic flow using 129x65 O-grid

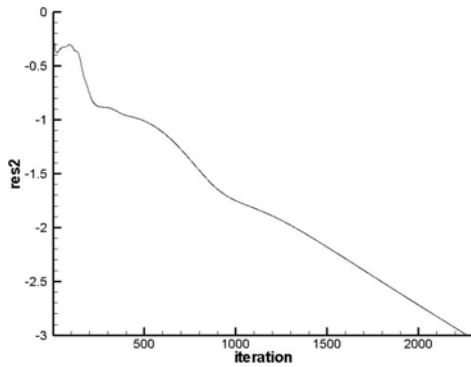


Figure 5.28: Convergence history of AUFS for first-order supersonic flow using 129x65 O-grid

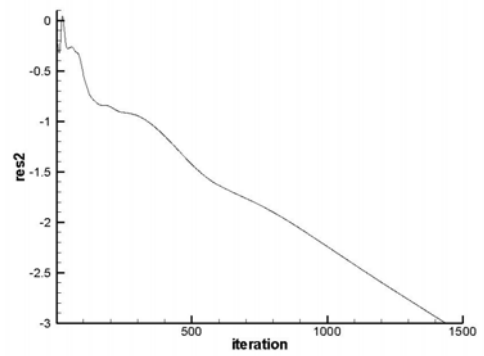


Figure 5.29: Convergence history of AUSM for first-order supersonic flow using 129x65 O-grid

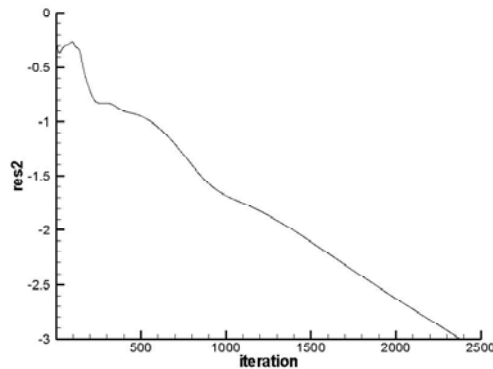


Figure 5.30: Convergence history of Roe's FDS Scheme for first-order supersonic flow using 129x65 O-grid

5.1.2 Second order calculations

5.1.2.1 Second order calculations without a limiter function

5.1.2.1.1 Subsonic Flow

The first case is the standard subcritical test case at a freestream Mach number of $M_\infty = 0.63$ and an angle of attack $\alpha = 2^\circ$. Obtained results are compared with the numerical results of Anderson & Thomas presented in [22] for Steger-Warming and Van Leer flux vector splitting schemes. This is selected in order to validate the written second order code. Then the obtained second order results for this case will be compared with each other for all the methods used. 129x65 O-grid shown in Figure 5.1 is used in the calculations.

The comparison of the distribution of pressure coefficients C_p for the first test case is given in Figures 5.31 and 5.32 for the Steger-Warming and Van Leer flux vector splitting schemes, respectively, with the numerical results of Anderson and Thomas. The second order accuracy is obtained by the linear reconstruction of the flow variables to the interfaces of control volumes. No limiters are used in the calculations as it is done in [20]. As the figures imply, written code gives results which are in close agreement with the ones obtained by Anderson & Thomas.

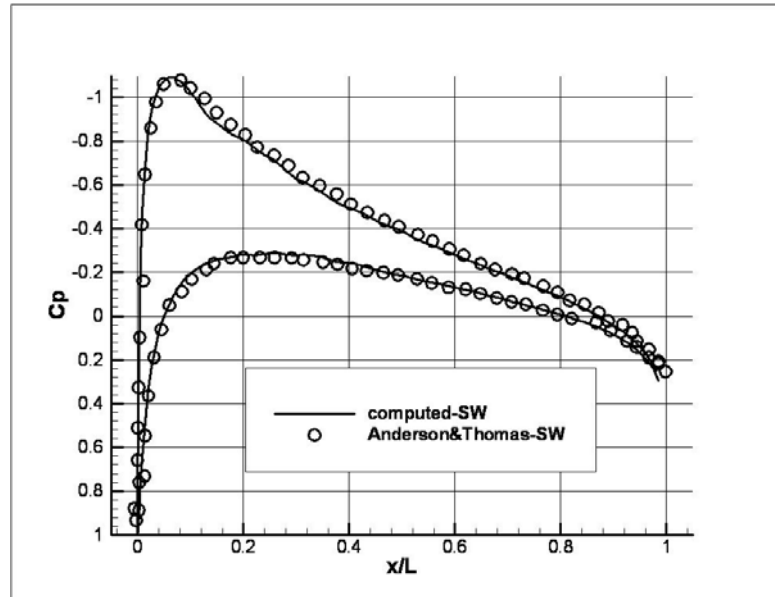


Figure 5.31: Distribution of pressure coefficient over NACA0012 airfoil at $M_\infty = 0.63$ $\alpha = 2^\circ$ using Steger-Warming FVS Scheme with second-order reconstruction by 129x65 O-grid

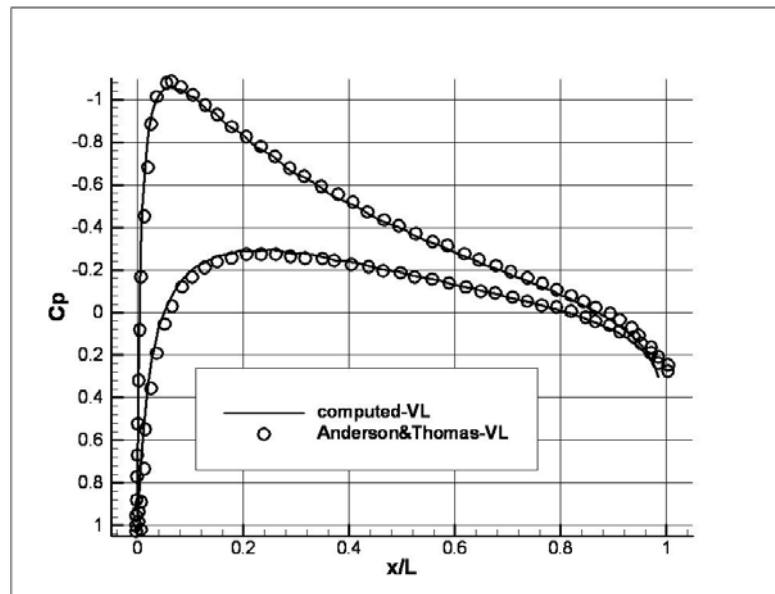


Figure 5.32: Distribution of pressure coefficient over NACA0012 airfoil at $M_\infty = 0.63$ $\alpha = 2^\circ$ using Van Leer FVS Scheme with second-order reconstruction by 129x65 O-grid

The results obtained by AUFS, AUSM and Roe's FDS are also presented for the same test case. The coefficient of pressure distributions for all methods is shown in Figure 5.33. All the schemes except AUFS give accurate results for this test case although it was anticipated that AUFS to give comparable accuracy with Roe's FDS as stated in [32].

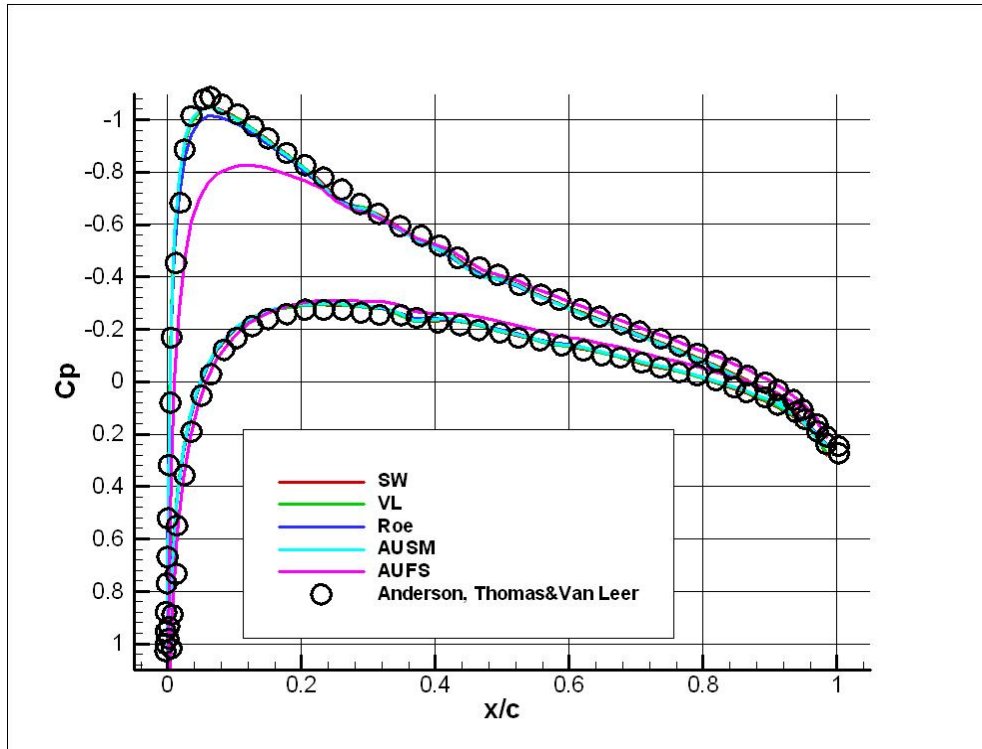


Figure 5.33: Distribution of pressure coefficient over NACA0012 airfoil at $M_\infty = 0.63$ $\alpha = 2^\circ$ using 129x65 O-grid with second-order reconstruction

The subsonic flow case considered for the first order calculations with a freestream Mach number of $M_\infty = 0.6$ and an angle of attack $\alpha = 0^\circ$, is used as the second test case for the second order calculations, in order to clarify the effect of second order reconstruction. 129x65 O-grid shown in Figure 5.1 is used in the calculations. The distribution of pressure coefficients is presented in Figure 5.34. Results obtained by using first order reconstruction shows that AUSM is the best in this test case. But as far as the second order reconstruction results are concerned, it is clearly seen that none of the schemes has superiority. AUSM and

Van-Leer FVS gives higher pressure coefficients at the peak point, but this can be accepted. For subsonic case, it can be concluded that second order reconstruction gives compatible results with the experimental data, even without a limiter.

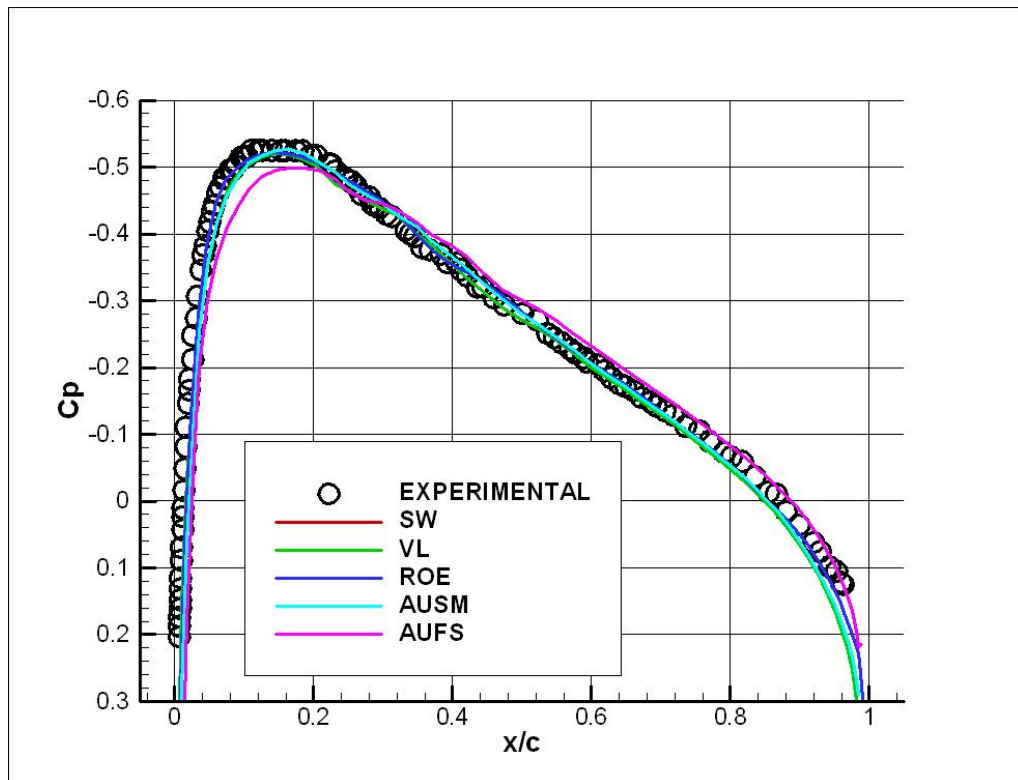


Figure 5.34: Distribution of pressure coefficient over NACA0012 airfoil at $M_\infty = 0.6$ $\alpha = 0^\circ$ using 129x65 O-grid with second-order reconstruction

Convergence histories of the second-order solutions are shown in Figures 5.35 to 5.39 for the second subsonic flow case. Convergence histories of the second-order transonic and supersonic flows will not be shown, since the subsonic flow results give the general idea about the increase in the convergence time when using second-order accurate reconstruction. All the methods converge in a longer time except AUFS. Actually AUFS converges faster than first order calculations.

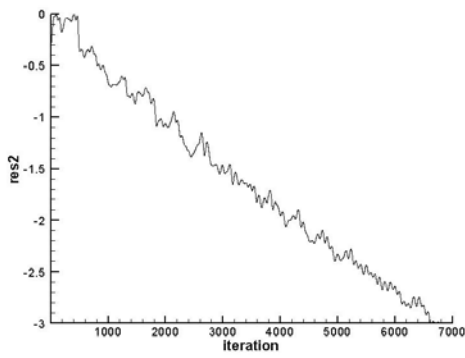


Figure 5.35: Convergence history of Steger-Warming FVS Scheme for second-order subsonic flow using 129x65 O-grid

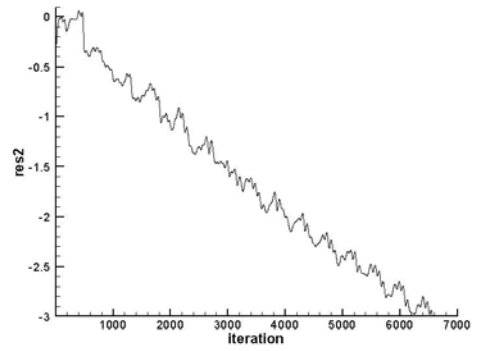


Figure 5.36: Convergence history of Van Leer FVS Scheme for second-order subsonic flow using 129x65 O-grid

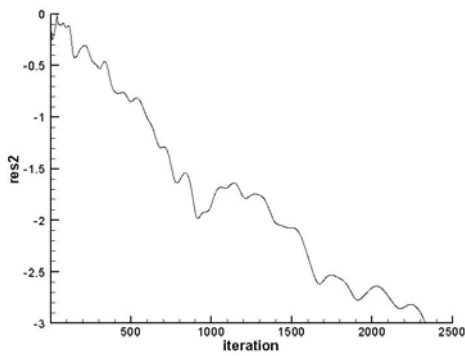


Figure 5.37: Convergence history of AUFS for second-order subsonic flow using 129x65 O-grid

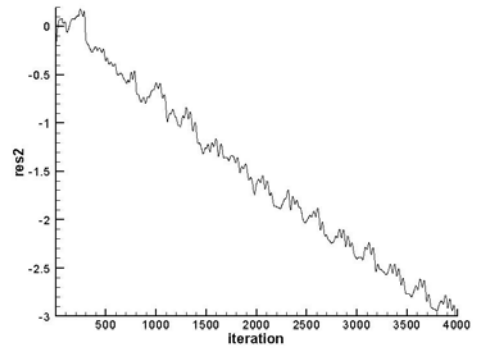


Figure 5.38: Convergence history of AUSM for second-order subsonic flow using 129x65 O-grid

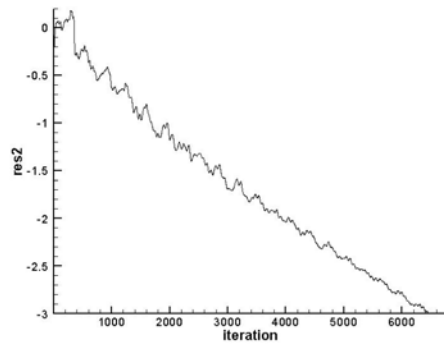


Figure 5.39: Convergence history of Roe's FDS Scheme for second-order subsonic flow using 129x65 O-grid

5.1.2.1.2 Transonic Flow

The first test case for the transonic flow has a freestream Mach number of $M_\infty = 0.85$ and an angle of attack $\alpha = 1^\circ$. This case is selected in order to compare the second-order accuracy, in transonic flow solutions with the ones obtained for AUSM and Roe's FDS in [22]. The grid used is not refined according to shocks, since Liou and Steffen have not used such a grid. Various types of meshes are used for the calculations. The selected meshes consist of 97x65, 129x65 and 257x65 cells, with the outer boundary placed at 20 chord lengths away from the body. Mesh used in this case does not have the same number of cells in the direction perpendicular to the solid body with the one given in [22], since the implementation of characteristic boundary conditions leads the outer boundary to be placed nearer to the body.

Figure 5.40 shows the distribution of the pressure coefficient for the above test case obtained by handling the flux terms with AUSM using 97x65 grid. The computed results are in good agreement with the results of Liou & Steffen in the subsonic region. On the other hand, shocks on the upper and lower surfaces can not be captured accurately. This is thought to be the effect of the coarse grid and solutions are obtained by using finer grids as specified before. Figure 5.41 shows comparison of the coefficient of pressure along the body using 257x65 grid and

the results obtained by Liou and Steffen. This figure shows that the obtained result is superior to the one obtained using the coarse mesh. The results reflect the need of a finer mesh since nothing other than the mesh is changed. Although the second one is better, the shock on the lower surface can not be captured accurately. The Zierep singularity which appears after the shocks on the lower and upper surfaces cannot be handled as good as Liou and Steffen.

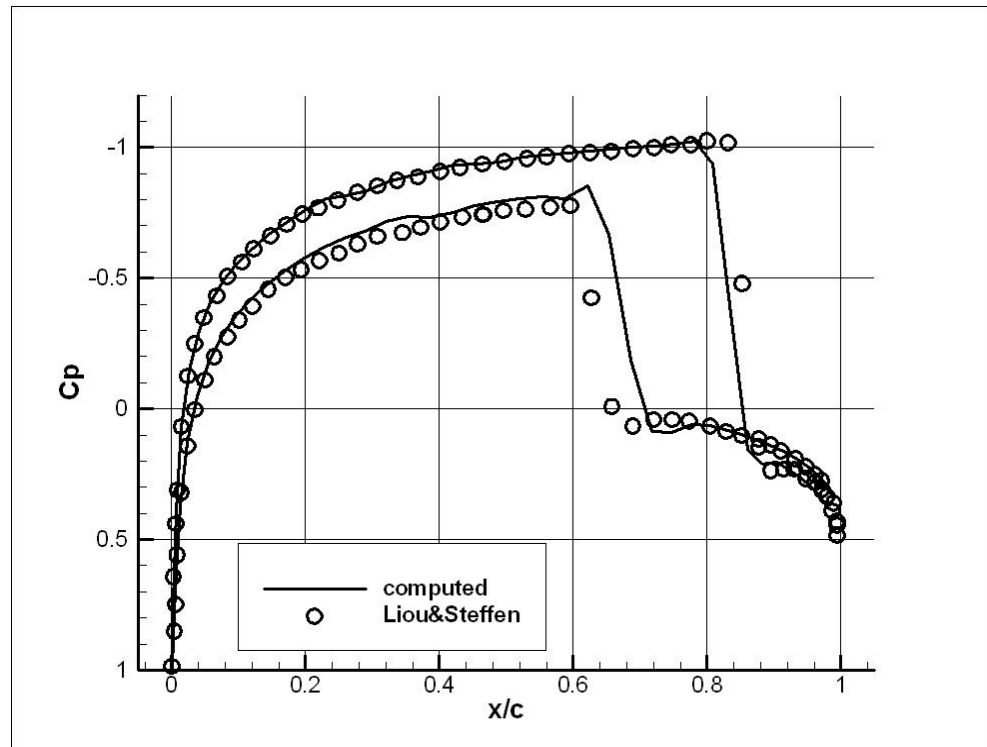


Figure 5.40: Distribution of pressure coefficient over NACA0012 airfoil at $M_\infty = 0.85$ $\alpha = 1^\circ$ using AUSM with second-order reconstruction by 97x65 O-grid

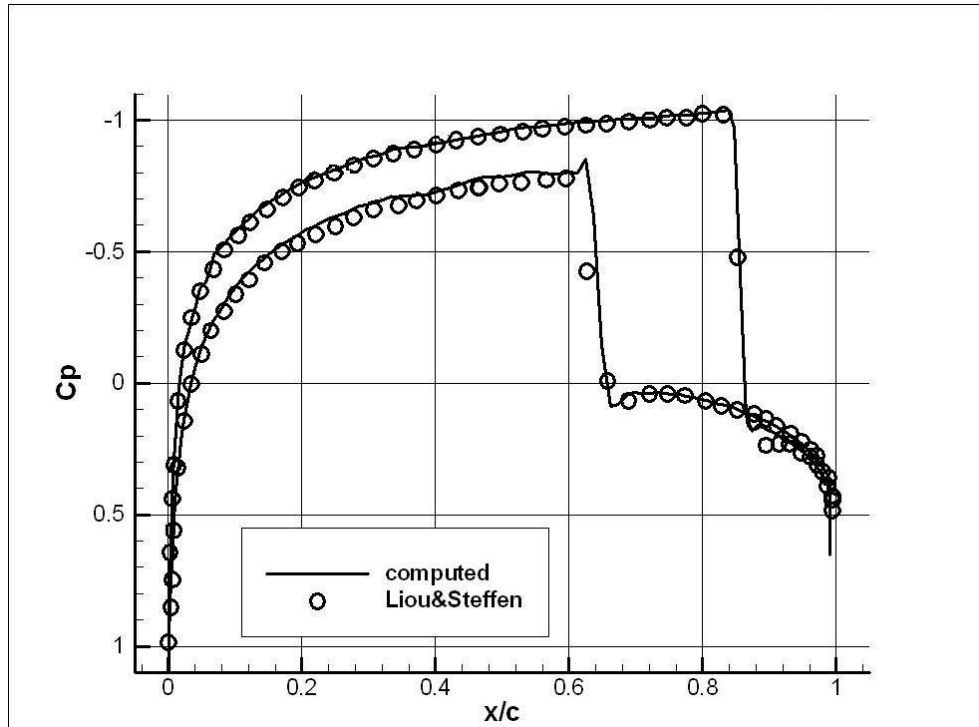


Figure 5.41: Distribution of pressure coefficient over NACA0012 airfoil at $M_\infty = 0.85$ $\alpha = 1^\circ$ using AUSM with second-order reconstruction by 257x65 O-grid

Figure 5.42 shows the pressure coefficient distribution over a NACA0012 airfoil obtained by using 257x65 mesh with Roe's FDS scheme when the freestream Mach number is 0.85 and angle of attack is 1° . Although it was expected to get very accurate results by using Roe's FDS scheme, second order calculations leads to spurious oscillations in the vicinity of shock waves. These oscillations may be damped by using appropriate flux or slope limiters. Use of finer grids having 513x65 cells or shock adapted grids give less oscillatory results, and the results obtained are shown in Figures 5.43 and 5.44. Although, shock adaptive grid has fewer cells in the overall domain, it slows down the convergence of the solution, and does not give sharper definition of the lower surface shock. Use of finer grids having 513x65 cells lowers the number of oscillations and carries them nearer to the shock wave. But, the convergence time is increased almost 1.5 times compared to 257x65 O-grid.

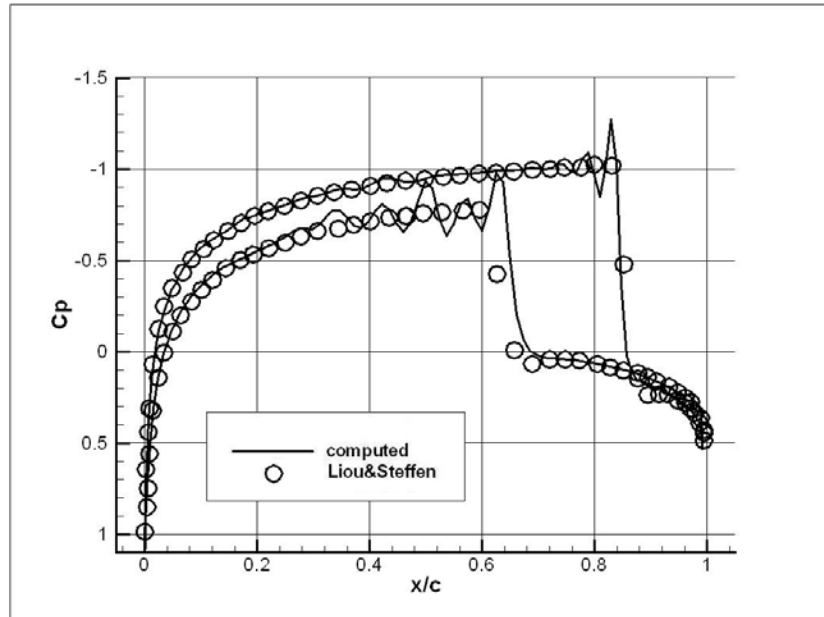


Figure 5.42: Distribution of pressure coefficient over NACA0012 airfoil at $M_\infty = 0.85$ $\alpha = 1^\circ$ using Roe's FDS Scheme with second-order reconstruction by 257x65 O-grid

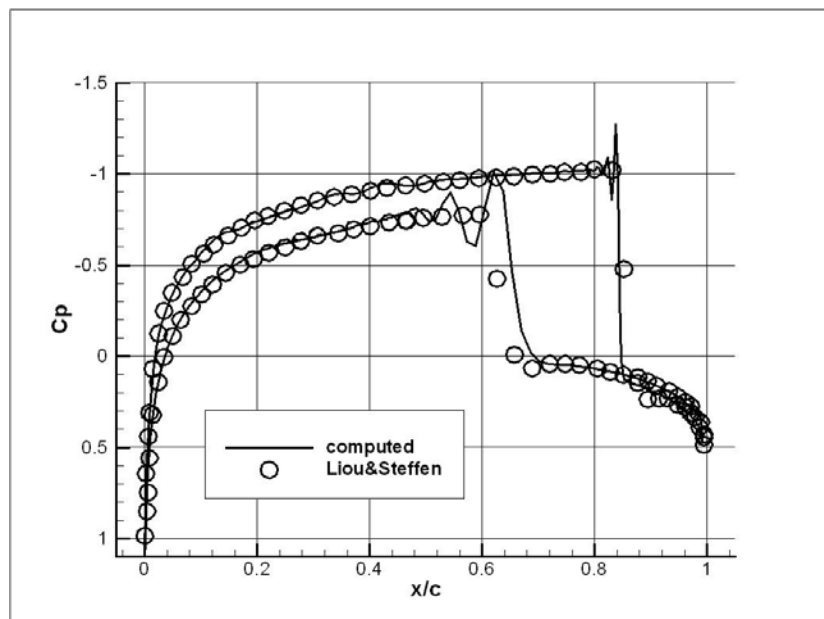


Figure 5.43: Distribution of pressure coefficient over NACA0012 airfoil at $M_\infty = 0.85$ $\alpha = 1^\circ$ using Roe's FDS Scheme with second-order reconstruction by 317x60 shock-adapted O-grid

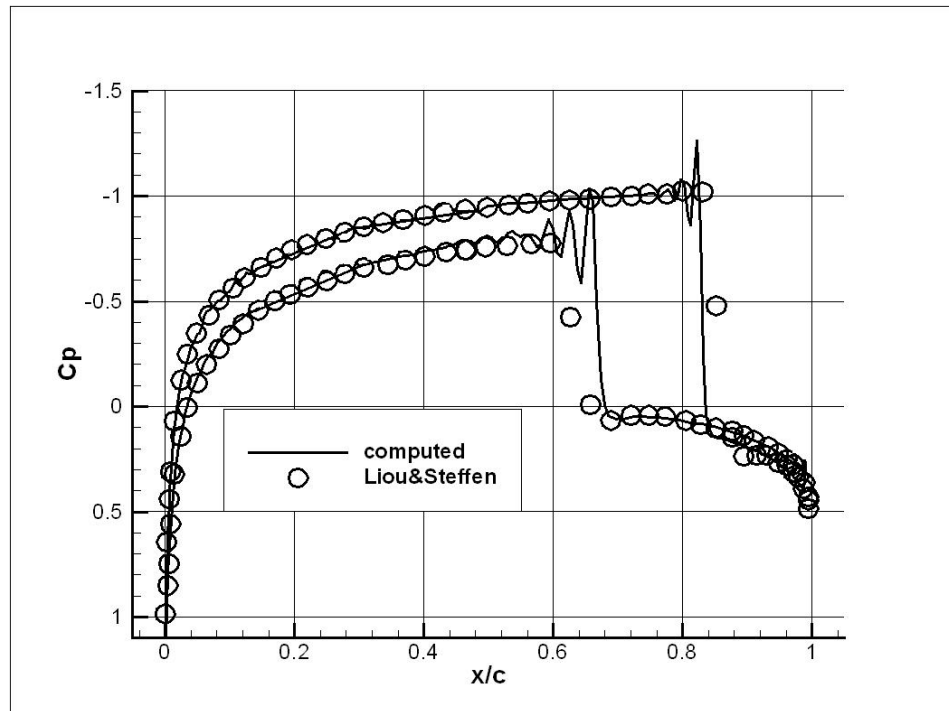


Figure 5.44: Distribution of pressure coefficient over NACA0012 airfoil at $M_\infty = 0.85$ $\alpha = 1^\circ$ using Roe's FDS Scheme with second-order reconstruction by 513x65 O-grid

The second case having a freestream Mach number of $M_\infty = 0.8$ and an angle of attack $\alpha = 1.25^\circ$ is used to test the accuracy of the Steger-Warming and Van Leer flux vector splitting schemes. The second order results using the corresponding schemes are presented by Anderson, Thomas and Van Leer in [20]. Obtained pressure coefficient distributions are compared with the ones in [20] and shown in Figures 5.45 and 5.46 for Steger-Warming and Van Leer flux vector splitting schemes, respectively. Both of the schemes give accurate results in handling the upper surface shock. However, shock on the lower surface of the airfoil is not captured as accurately as the upper surface one. This accuracy may be increased with the use of finer grids. Finally, Steger-Warming and Van Leer flux vector splitting schemes do not lead any oscillations in the vicinity of shocks, although there was a risk of generation of oscillations in second-order schemes.

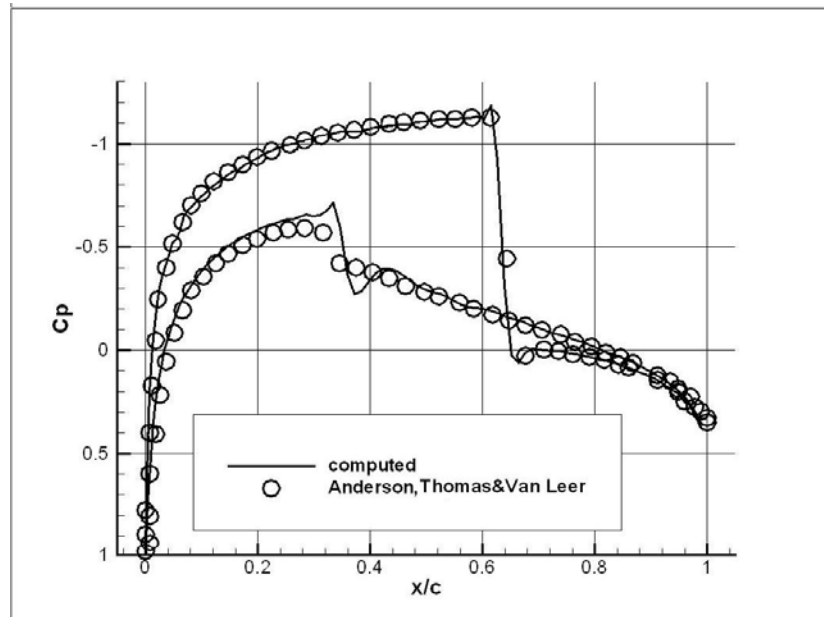


Figure 5.45: Distribution of pressure coefficient over NACA0012 airfoil at $M_\infty = 0.8$ $\alpha = 1.25^\circ$ using Steger-Warming FVS Scheme with second-order reconstruction by 257x65 O-grid

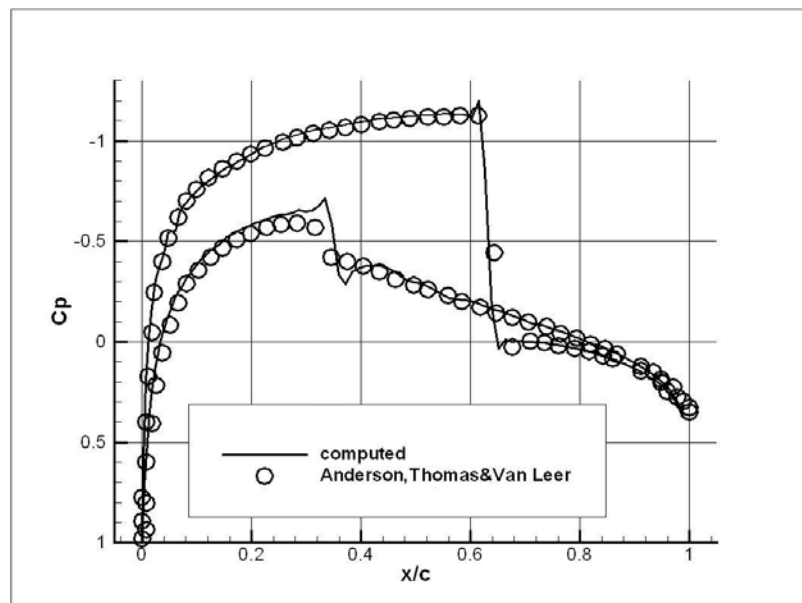


Figure 5.46: Distribution of pressure coefficient over NACA0012 airfoil at $M_\infty = 0.8$ $\alpha = 1.25^\circ$ using Van Leer FVS Scheme with second-order reconstruction by 257x65 O-grid

Behavior of AUSM, Roe's flux difference splitting scheme, Steger-Warming and Van Leer flux vector splitting schemes with second order reconstruction techniques in transonic flow is compared with the results in literature. However, second-order performance of AUFS cannot be tested since no results are presented in the literature. Instead, this flux splitting scheme is tested by using the first-order test results with case of freestream Mach number of 0.8 at an angle of attack 0° . Distribution of pressure coefficients along the airfoil is shown in Figure 5.47 for all methods. Results show that the Steger-Warming and Van Leer flux vector splitting schemes and AUSM lead to accurate results when using second-order reconstruction methods without limiters and Roe's flux difference splitting schemes lead oscillations as specified before. Surprisingly, AUFS gives less accurate results than its first-order reconstruction results.

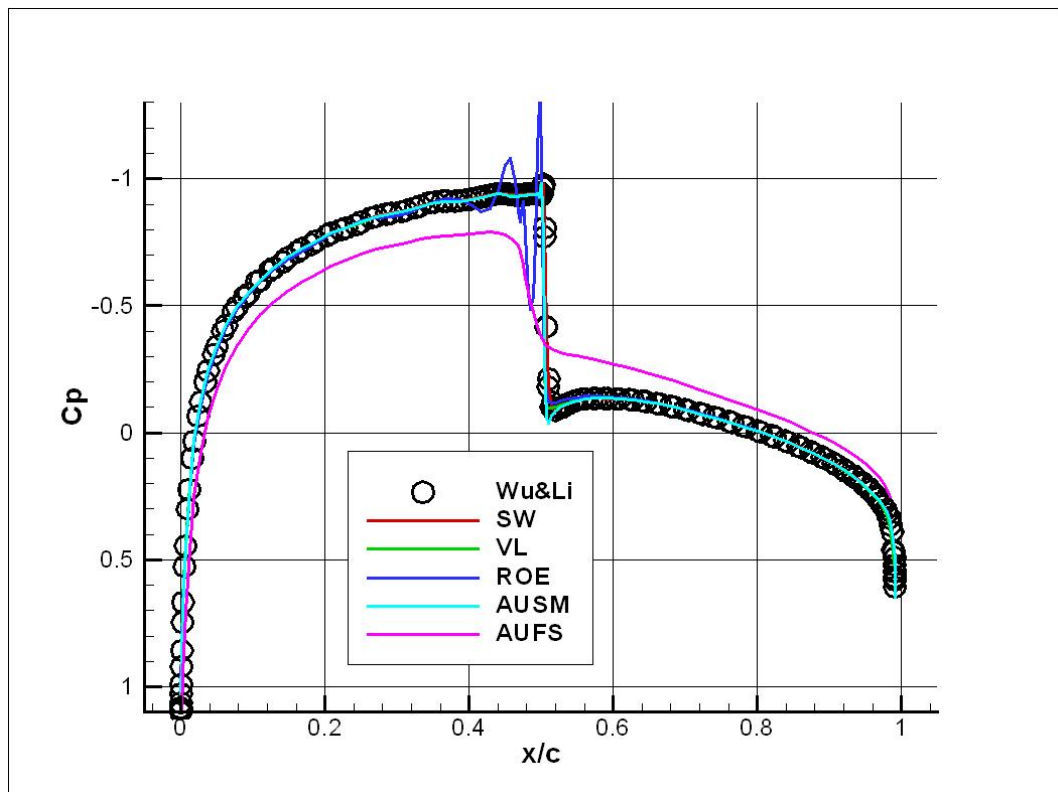


Figure 5.47: Distribution of pressure coefficient over NACA0012 airfoil at $M_\infty = 0.8$ $\alpha = 0^\circ$ using 185x60 shock-adapted O-grid with second-order reconstruction

5.1.2.1.3 Supersonic Flow

The same supersonic test case of $M_\infty = 1.2$ at a 0 degree angle of attack as in the first-order calculations is used. The 129x65 O-grid used in the subsonic flow case, is again chosen for the solution. The obtained solution is compared with the ones in [22].

Figure 5.48 shows the pressure coefficient distribution over the NACA0012 airfoil compared with the results obtained from [20]. It is seen from this figure that all methods give compatible results. The important aspect for the specified supersonic flow is not the pressure distribution over the airfoil, but the behavior of the flow at the leading and trailing edges of the airfoil. The bow shock occurs at the leading edge, and oblique shock occurs at the trailing edge, as specified in subsection 5.1.1.3. The performance of the methods in handling these shocks is important in this case. Figures 5.50 to 5.54 show the pressure contours which will be compared to Figure 5.49. The pressure distribution given in Figure 5.49 is obtained by using second order AUSM in [22]. As seen in Figure 5.53, the obtained result greatly agrees with the one in [22]. Steger-Warming and Van Leer flux vector splitting schemes and AUSM give very accurate results in the definition of the bow and oblique shocks. Although Roe's flux difference splitting scheme resolve the bow shock, the scheme pollutes the flow region, which is named as the carbuncle instability. The carbuncle problem is the most common problem that researchers face with in the solutions using Roe's method. The pollution affects the flow region in front of the bow shock, and the definition of the oblique shock is not very accurate. AUFS does not resolve the shocks at the trailing and leading edges very accurately.

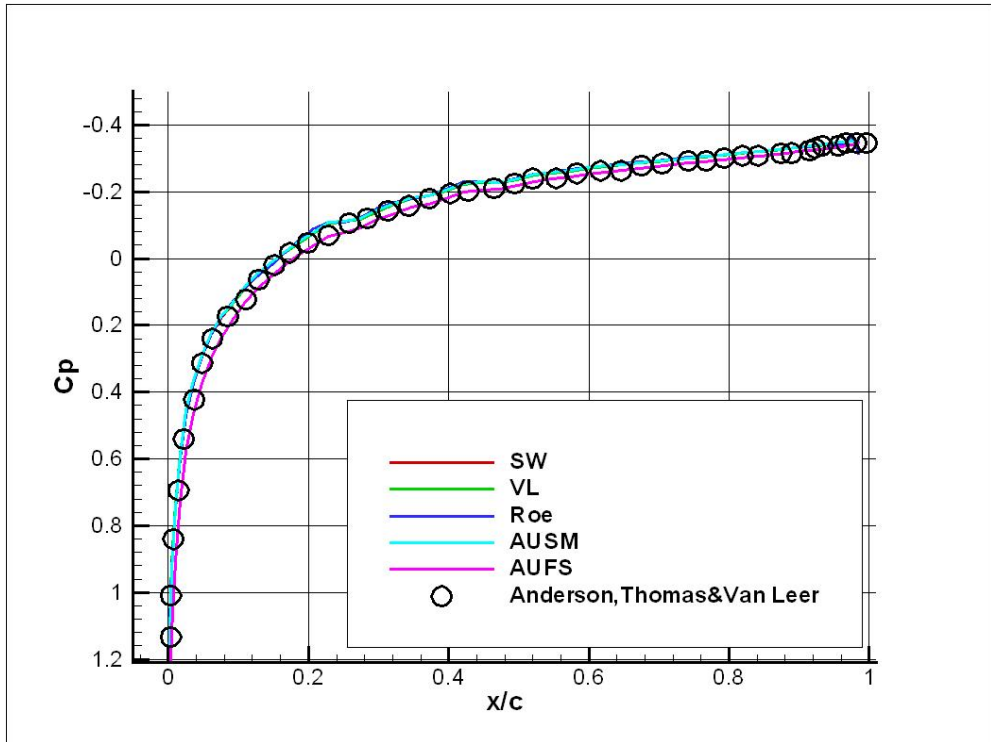


Figure 5.48: Distribution of pressure coefficient over NACA0012 airfoil at $M_\infty = 1.2 \alpha = 0^\circ$ using 129x65 O-grid with second-order reconstruction

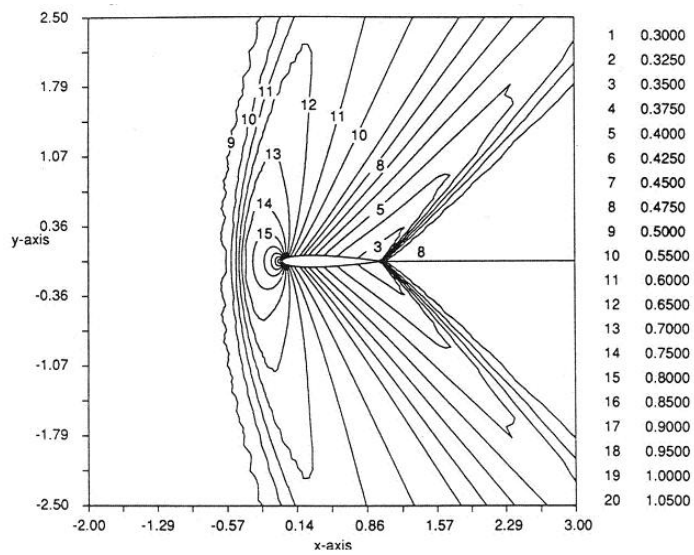


Figure 5.49: Pressure contours around NACA0012 at $M_\infty = 1.2 \alpha = 0^\circ$ by AUSM [22]

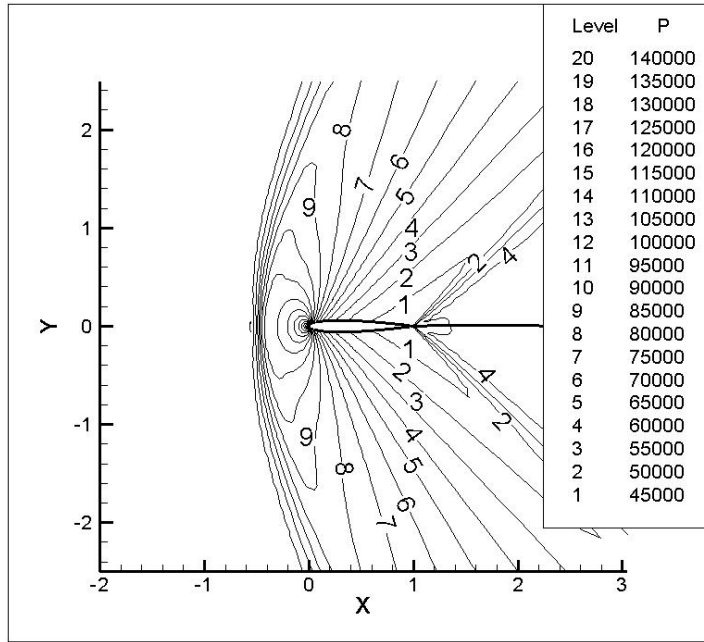


Figure 5.50: Pressure contours around NACA0012 at $M_\infty = 1.2$ $\alpha = 0^\circ$ by Steger-Warming FVS Scheme using 129x65 O-grid with second-order reconstruction

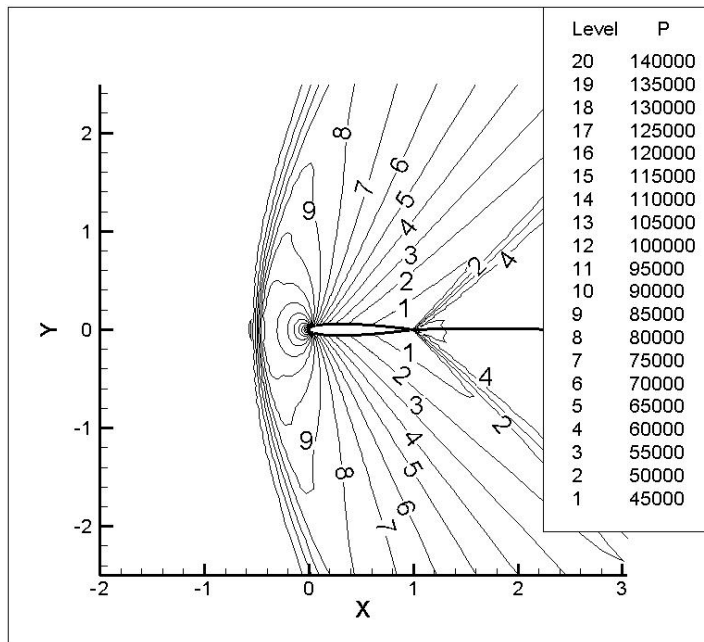


Figure 5.51: Pressure contours around NACA0012 at $M_\infty = 1.2$ $\alpha = 0^\circ$ by Van Leer FVS Scheme using 129x65 O-grid with second-order reconstruction

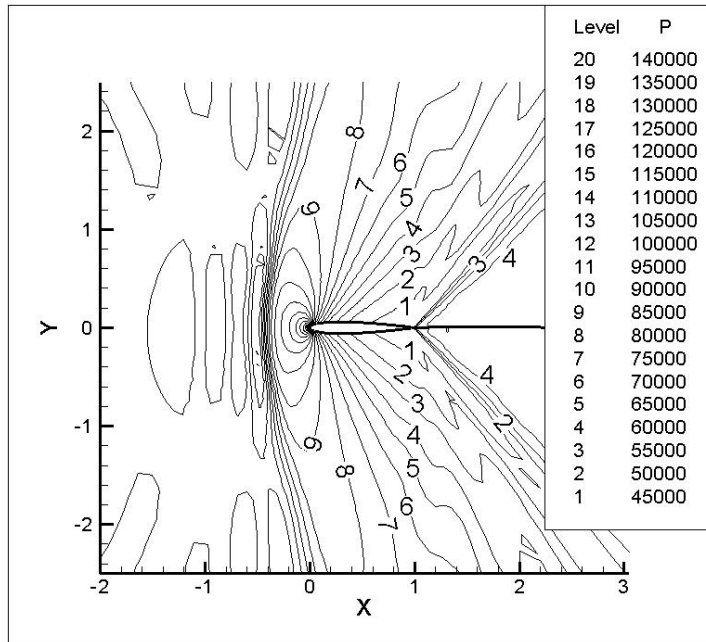


Figure 5.52: Pressure contours around NACA0012 at $M_\infty = 1.2 \alpha = 0^\circ$ by Roe's FDS
 Scheme using 129x65 O-grid with second-order reconstruction

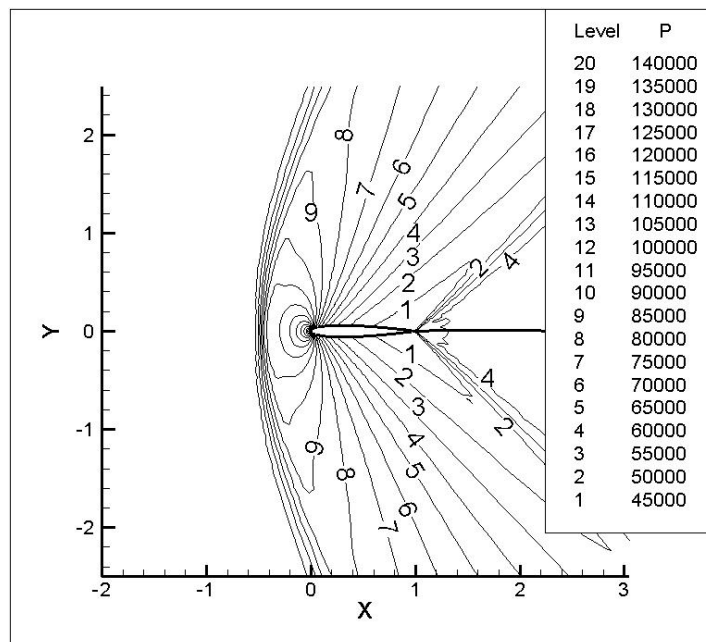


Figure 5.53: Pressure contours around NACA0012 at $M_\infty = 1.2 \alpha = 0^\circ$ by AUSM using
 129x65 O-grid with second-order reconstruction

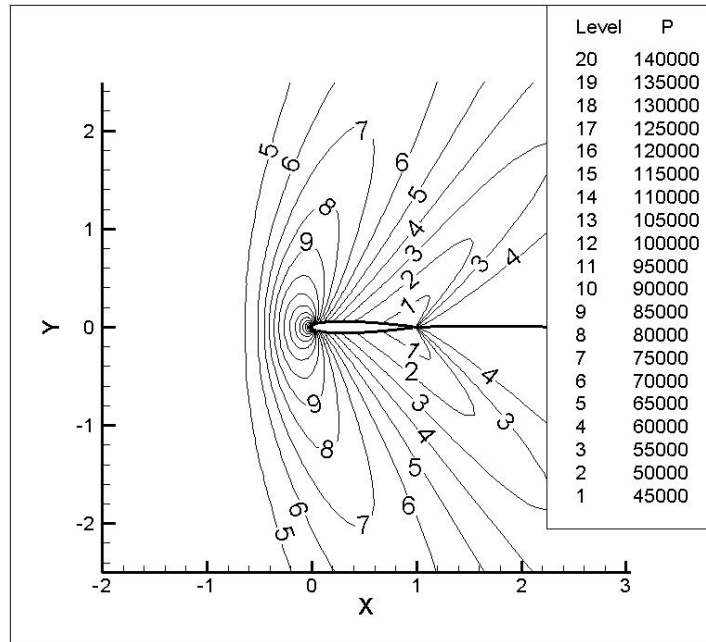


Figure 5.54: Pressure contours around NACA0012 at $M_\infty = 1.2$, $\alpha = 0^\circ$ by AUFS using 129x65 O-grid with second-order reconstruction

5.1.2.2 Second order calculations with a limiter function

5.1.2.2.1 Subsonic flow

The subsonic flow case with a freestream Mach number of $M_\infty = 0.6$ and an angle of attack $\alpha = 0^\circ$ is used for testing the effect of limiters in second order calculations. 129x65 O-grid shown in Figure 5.1 is used in the calculations. The distribution of pressure coefficients is presented in Figure 5.55. As expected, use of limiters does not improve the solution accuracy as the figure implies. Since subsonic flow does not include any flow regions with high gradients limiter function does not have any effect on the solution, and it guarantees fully second order calculation.

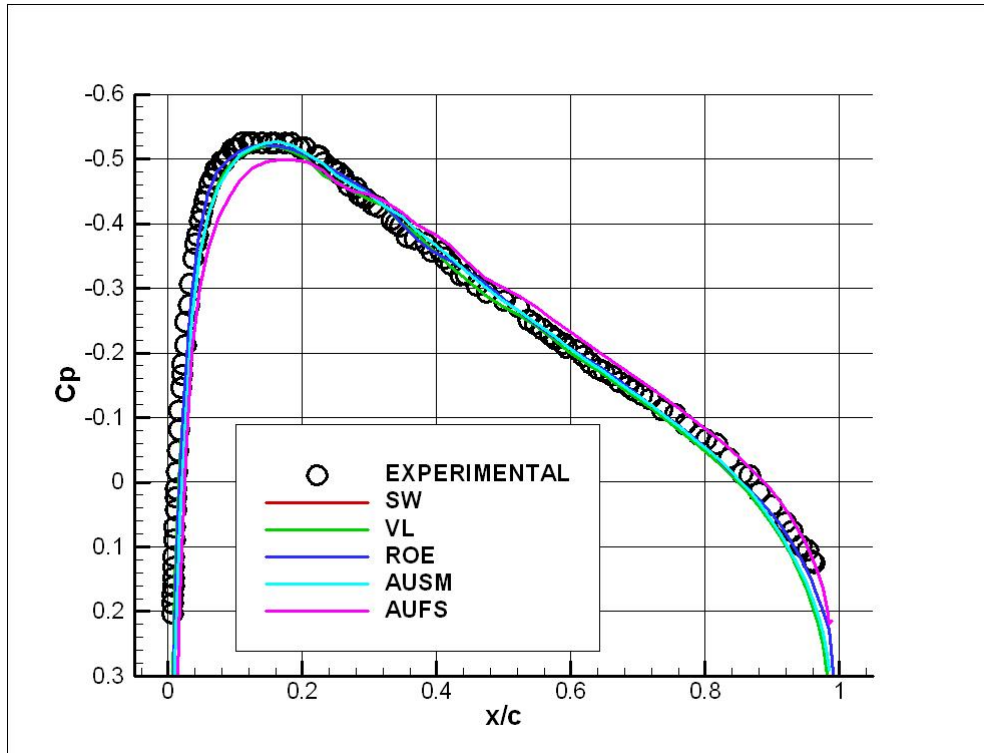


Figure 5.55: Distribution of pressure coefficient over NACA0012 airfoil at $M_\infty = 0.6$ $\alpha = 0^\circ$ using 129x65 O-grid with second-order reconstruction with limiter function

5.1.2.2.2 Transonic Flow

The transonic flow case with a freestream Mach number of $M_\infty = 0.8$ and an angle of attack $\alpha = 0^\circ$ is used for testing the effect of limiters in second order calculations. The calculations are performed by using 185x60 shock-adapted O-grid. The results obtained by second order reconstruction without a limiter function for the transonic flow case in consideration were discussed in subsection 5.1.2.1.2. Roe's flux difference splitting scheme leads to oscillations in the vicinity of shocks when limiters are not used. Figure 5.56 shows the distribution of pressure coefficient for second order transonic flow calculation with limiter function in comparison with the results of Wu & Li [66].

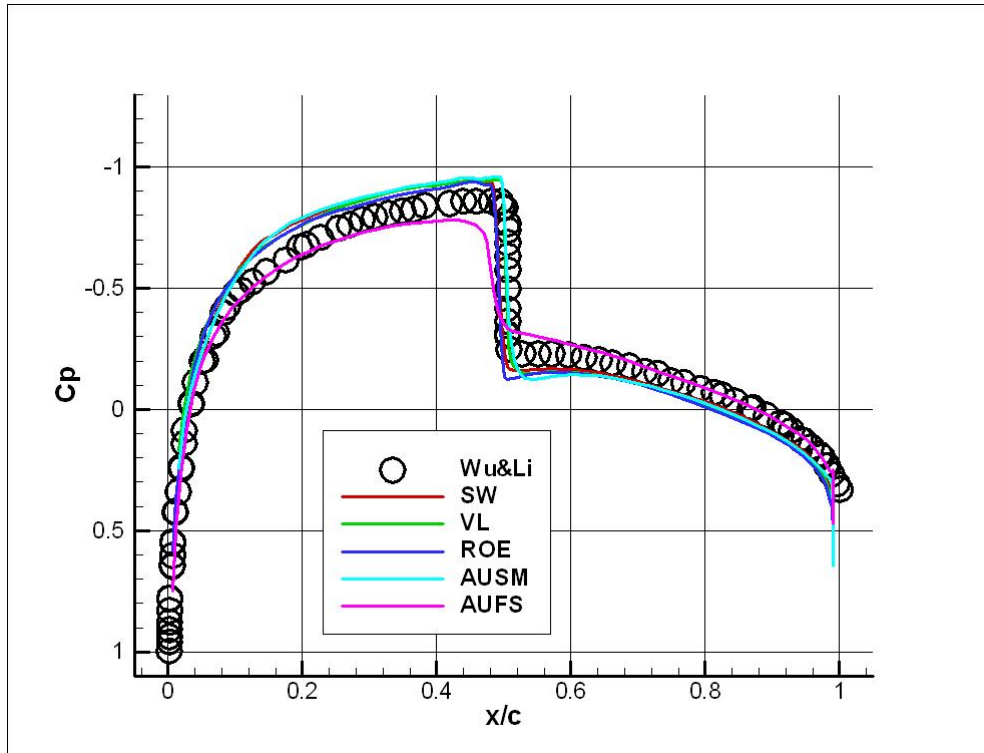


Figure 5.56: Distribution of pressure coefficient over NACA0012 airfoil at $M_\infty = 0.8$ $\alpha = 0^\circ$ using 185x60 shock-adapted O-grid with second-order reconstruction with limiter function

Figure 5.56 show the effect of the limiter function. Limiter function damps the oscillations occurred when using Roe's flux difference splitting scheme. Roe's flux difference splitting scheme provides a sharp definition of the normal shock wave. Van Leer's flux vector splitting scheme and AUSM provides the most accurate results by capturing the normal shock better than the other schemes. Roe's flux difference splitting scheme and Steger-Warming flux vector splitting schemes also give accurate results but the location of the normal shock can not be defined as accurate as AUSM and Van Leer's flux vector splitting scheme. AUFS does not lead to accurate results as it was the case in the second order calculations without a limiter function.

5.1.2.2.3 Supersonic Flow

The supersonic flow case with a freestream Mach number of $M_\infty = 1.2$ and an angle of attack $\alpha = 0^\circ$ is used for testing the effect of limiters in second order calculations. 129x65 O-grid is used in the calculations. The obtained results are compared with results of Liou & Steffen [22], the pressure contours provided in [22] are shown in Figure 5.57. Figures 5.58 to 5.62 show the pressure contours obtained by using the flux splitting schemes considered in this study.

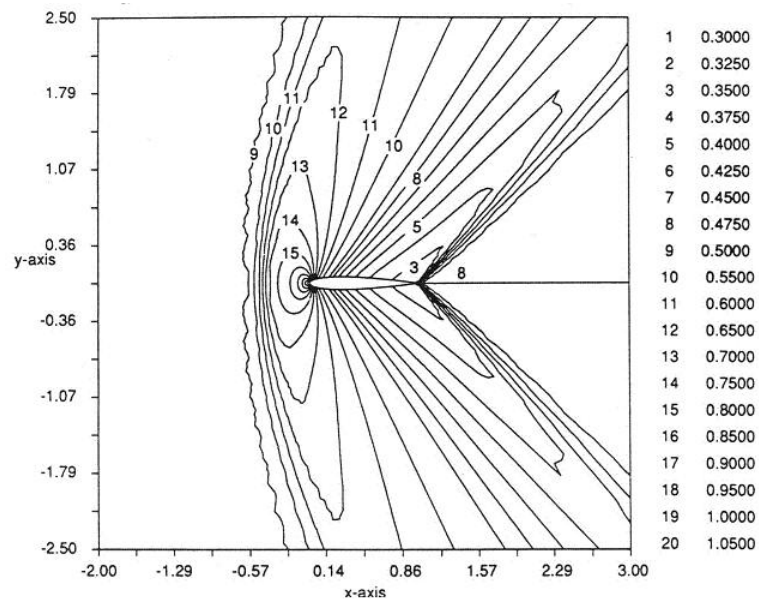


Figure 5.57: Pressure contours around NACA0012 at $M_\infty = 1.2$ $\alpha = 0^\circ$ by AUSM [22]

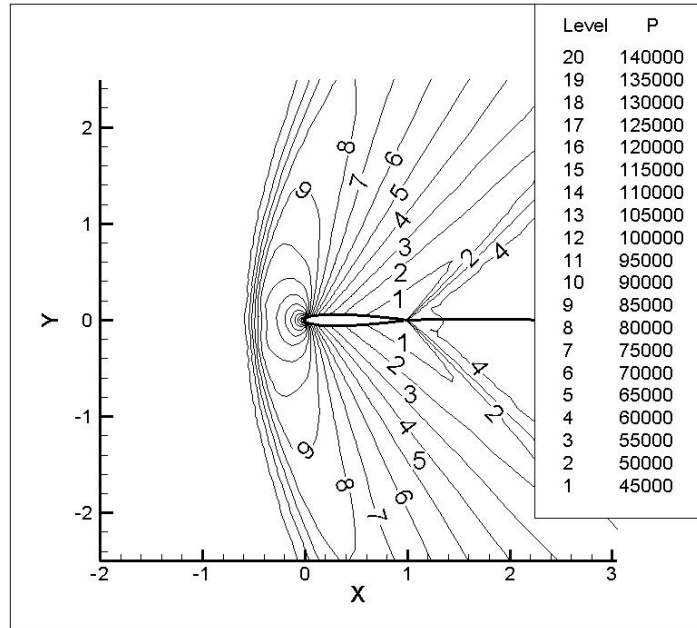


Figure 5.58: Pressure contours around NACA0012 at $M_\infty = 1.2$ $\alpha = 0^\circ$ by Steger-Warming FVS Scheme using 129x65 O-grid with second-order reconstruction with limiter function

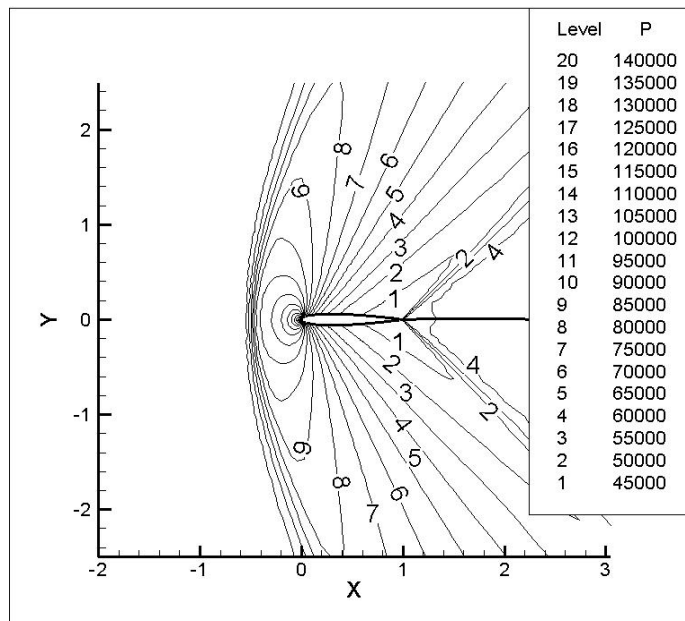


Figure 5.59: Pressure contours around NACA0012 at $M_\infty = 1.2$ $\alpha = 0^\circ$ by Van Leer FVS Scheme using 129x65 O-grid with second-order reconstruction with limiter function

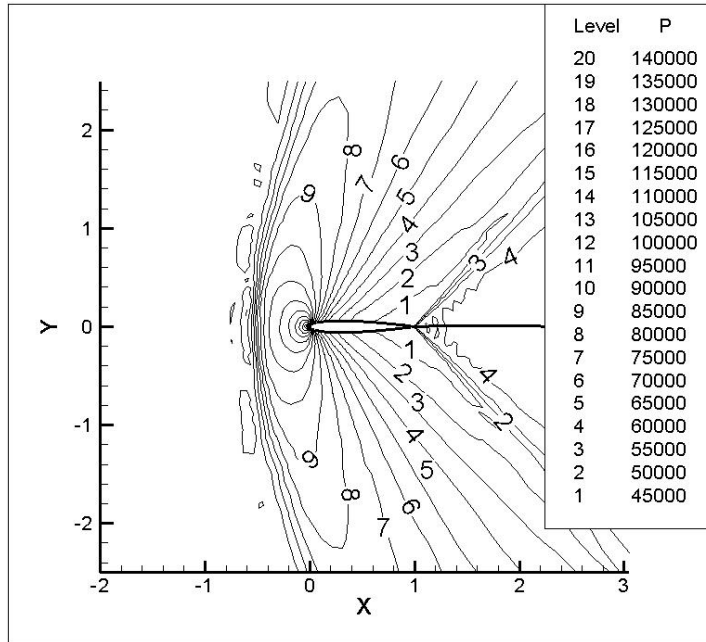


Figure 5.60: Pressure contours around NACA0012 at $M_\infty = 1.2 \alpha = 0^\circ$ by Roe's FDS Scheme using 129x65 O-grid with second-order reconstruction with limiter function

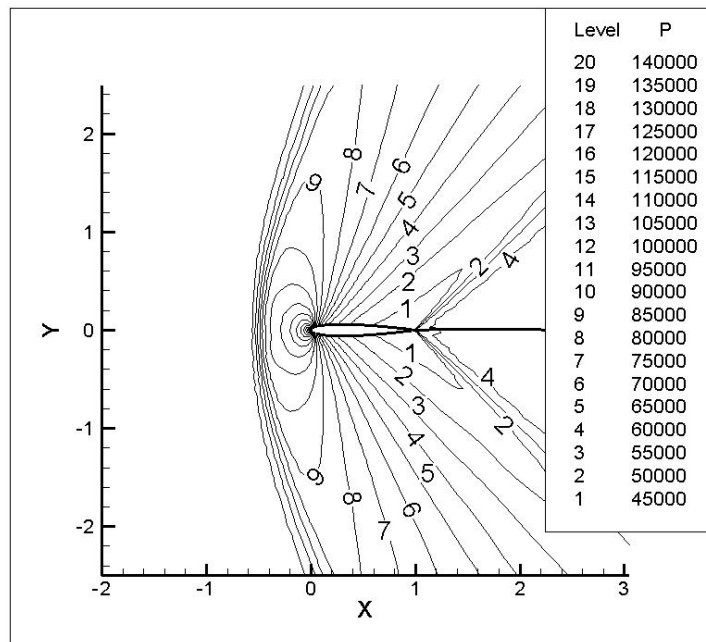


Figure 5.61: Pressure contours around NACA0012 at $M_\infty = 1.2 \alpha = 0^\circ$ by AUSM using 129x65 O-grid with second-order reconstruction with limiter function

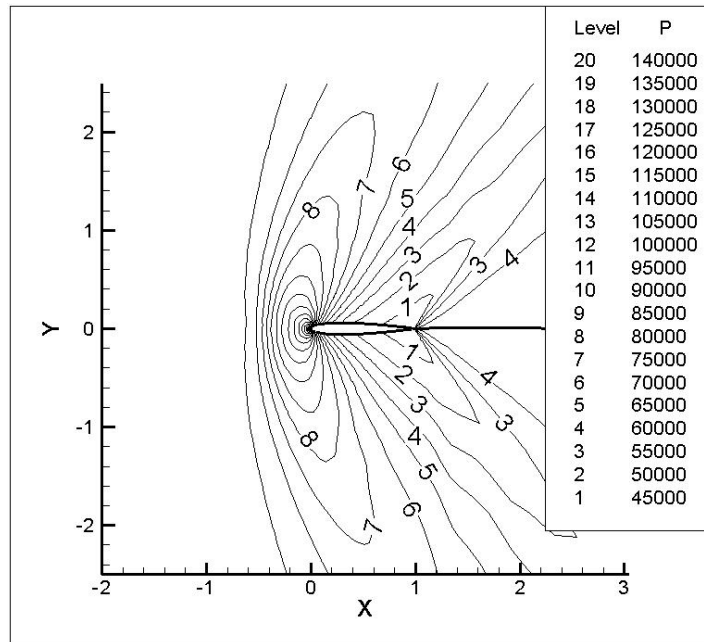


Figure 5.62: Pressure contours around NACA0012 at $M_\infty = 1.2$ $\alpha = 0^\circ$ by AUFS using 129x65 O-grid with second-order reconstruction with limiter function

The obtained results are not much different than the results obtained by using second order reconstruction without a limiter function. Using limiter function advances the results of Roe's flux difference splitting scheme only. As seen in Figure 5.60 the pollution upstream the bow shock due the carbuncle instability is mostly damped by the limiter function.

5.2 Internal Flow

Flow in channel having a circular arc in the lower boundary is analyzed. The geometry used for subsonic and transonic flows consists of a bump having a thickness of 10% of the chord length, while the bump has a thickness of 4% of the chord length in the domain for supersonic flows. For both cases, the computational domain consists of 129x33 grids as shown in Figure 5.63.

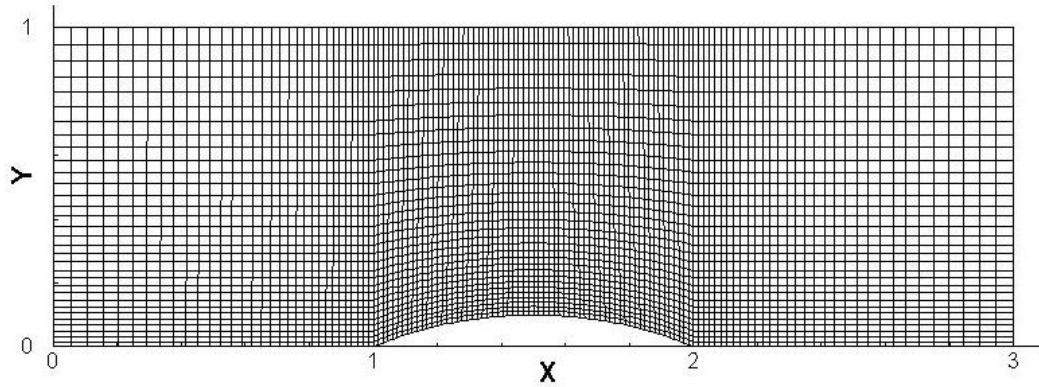


Figure 5.63: 129x33 grid for a channel having a circular arc

5.2.1 First-order Calculations

5.2.1.1 Subsonic Flow

The inflow Mach number is given as $M_\infty = 0.5$, where the theoretical solution gives a subsonic, symmetric solution about the bump. The Mach contours presented by Ni [60] are shown in Figure 5.64, while Figures 5.65 to 5.69 shows the Mach contours obtained by using the flux splitting methods. Figure 5.70 presents a complete comparison for the distribution of Mach number in the computational domain in comparison with Ni's result. One may conclude from this figure that Roe's flux difference splitting scheme and AUSM give the most accurate results; the results obtained are highly symmetric about the bump which is the expected outcome. The dissipative character of Steger-Warming flux vector splitting scheme is clearly observed from the Mach number distribution. Van Leer flux vector splitting scheme and AUFS result in almost the same Mach number distribution. Although the latter three schemes do not lead to symmetric results around the bump, the outcome of the schemes has a comparable accuracy. The asymmetry occurring at the inlet and outlet, which is identified in the Mach contours and the lower boundary Mach number distributions, is thought to be due to the boundary conditions. Method of characteristics takes the inlet and outlet Mach numbers into concern and could give more accurate results.

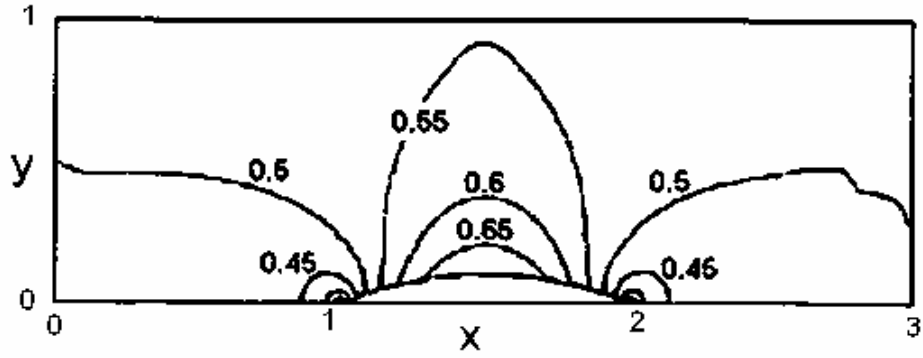


Figure 5.64: Mach contours in the channel having a circular bump at $M_\infty = 0.5$ $\alpha = 0^\circ$ by Ni [60]

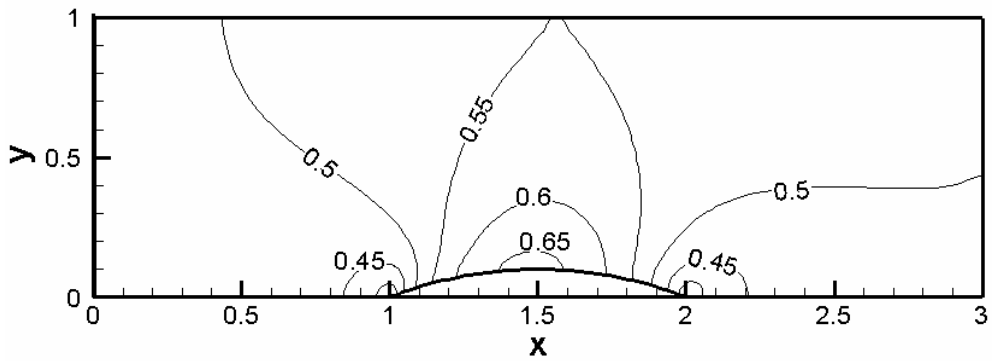


Figure 5.65: Mach contours in the channel having a circular bump at $M_\infty = 0.5$ $\alpha = 0^\circ$ obtained by Steger-Warming flux vector splitting scheme using first-order reconstruction

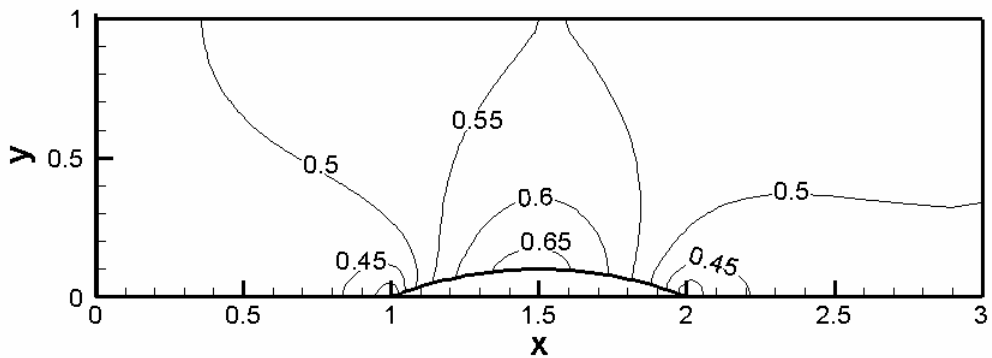


Figure 5.66: Mach contours in the channel having a circular bump at $M_\infty = 0.5$ $\alpha = 0^\circ$ obtained by Van Leer flux vector splitting scheme using first-order reconstruction

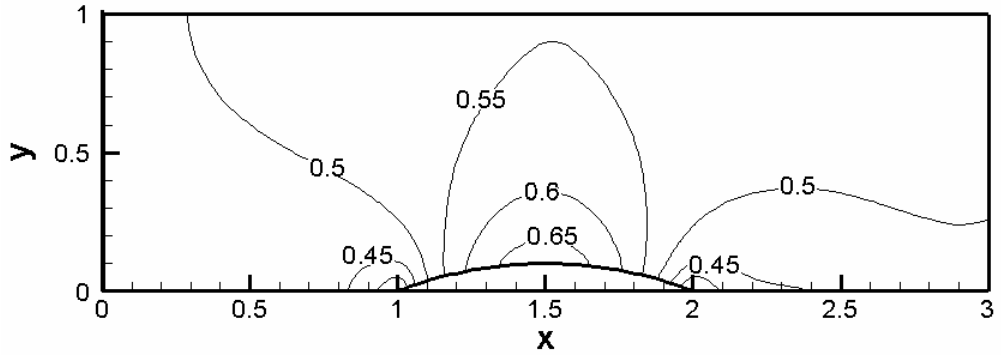


Figure 5.67: Mach contours in the channel having a circular bump at $M_\infty = 0.5$ $\alpha = 0^\circ$ obtained by Roe's flux difference splitting scheme using first-order reconstruction

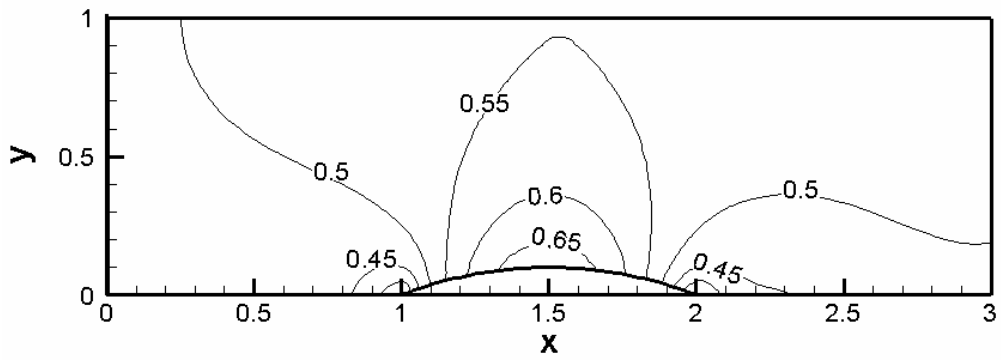


Figure 5.68: Mach contours in the channel having a circular bump at $M_\infty = 0.5$ $\alpha = 0^\circ$ obtained by AUSM using first-order reconstruction

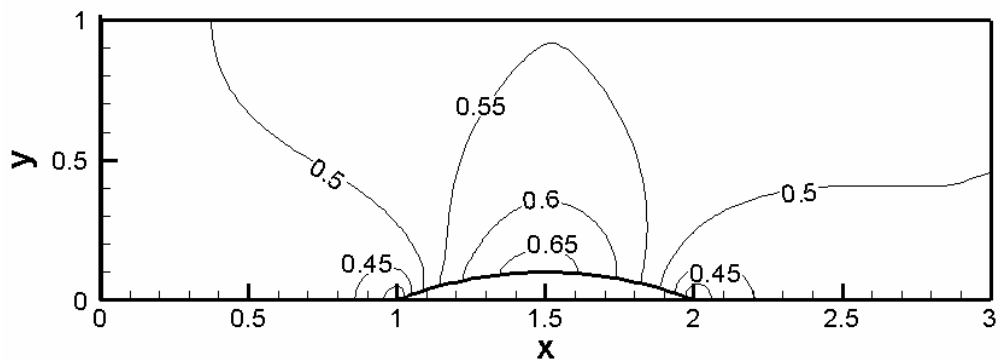
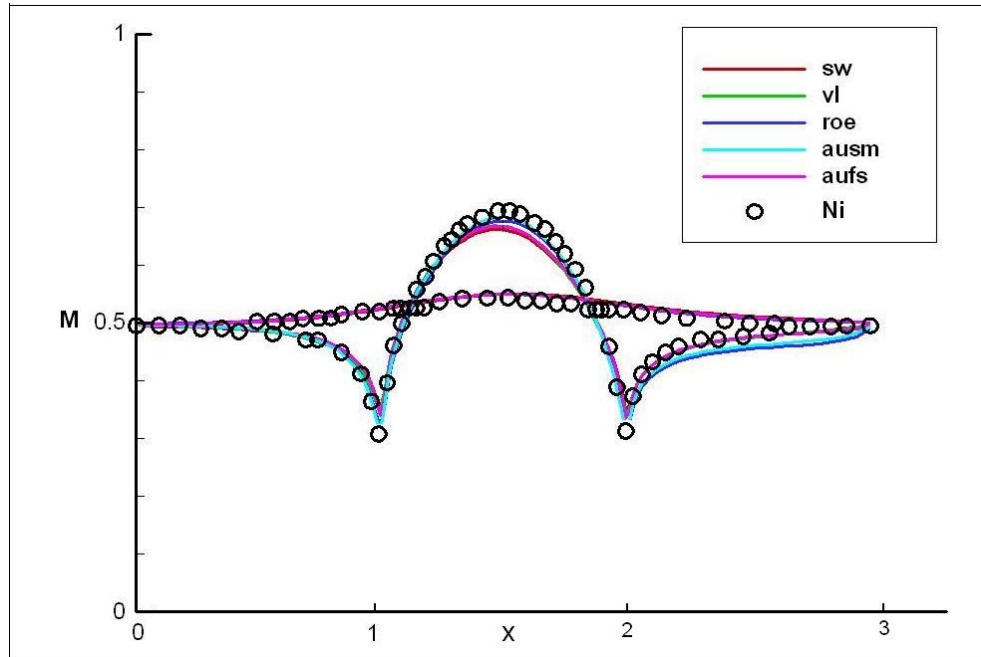


Figure 5.69: Mach contours in the channel having a circular bump at $M_\infty = 0.5$ $\alpha = 0^\circ$ obtained by AUFS using first-order reconstruction



5.70: Distribution of Mach number in the channel having a circular bump at $M_\infty = 0.5 \alpha = 0^\circ$ using first-order reconstruction

5.2.1.2 Transonic Flow

For transonic flow case, the inlet Mach number of $M_\infty = 0.675$ is used. This leads to a transonic flow with a shock located at 72% of the bump chord. The Mach contours obtained by Ni [60] are shown in Figure 5.71, whilst Figures 5.72 to 5.76 presents the Mach contours obtained by using the flux splitting methods. Figure 5.78 presents the distribution of Mach number in the domain in comparison with Ni's result. The flux splitting schemes presented in this study, except Steger-Warming flux vector splitting scheme, capture the shock at around 72% of the bump's chord and give accurate results for the transonic flow case. Steger-Warming flux vector splitting scheme can not catch the shock wave sharply, which was the situation for the transonic flow case of first-order calculations. On the other hand, as in the subsonic flow case AUSM and Roe's flux difference splitting schemes give the most accurate results compared to the others.

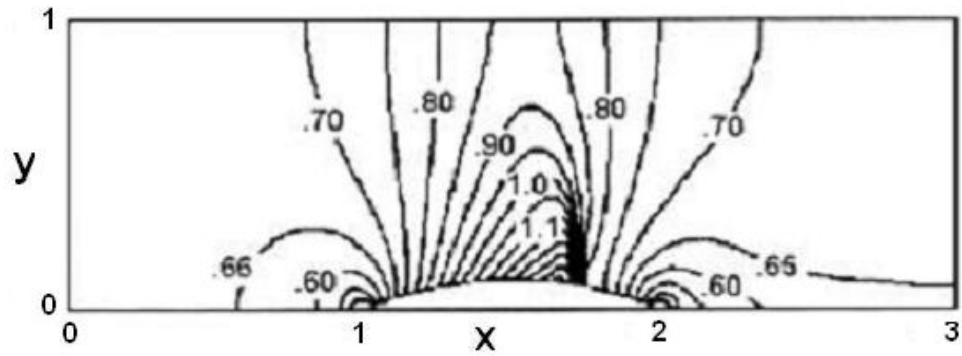


Figure 5.71: Mach contours in the channel having a circular bump at $M_\infty = 0.675$ $\alpha = 0^\circ$
by Ni [60]

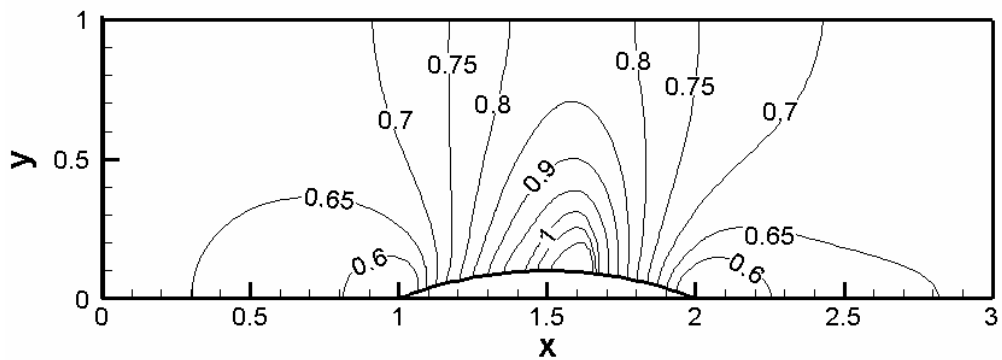


Figure 5.72: Mach contours in the channel having a circular bump at $M_\infty = 0.675$ $\alpha = 0^\circ$
obtained by Steger-Warming flux vector splitting scheme using first-order reconstruction

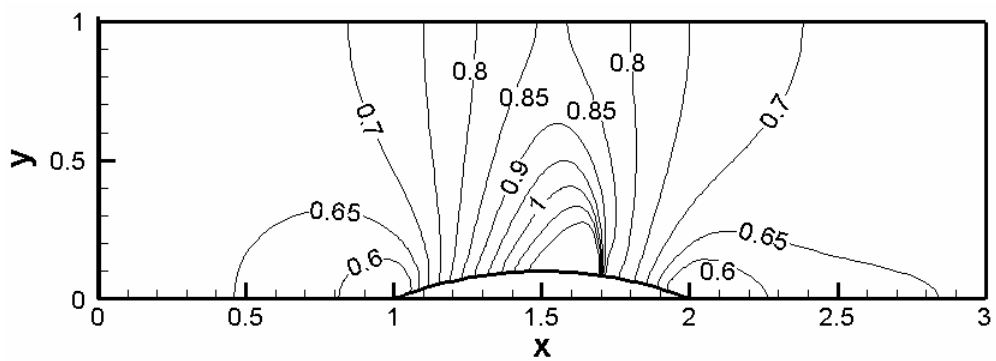


Figure 5.73: Mach contours in the channel having a circular bump at $M_\infty = 0.675$ $\alpha = 0^\circ$
obtained by Van Leer flux vector splitting scheme using first-order reconstruction

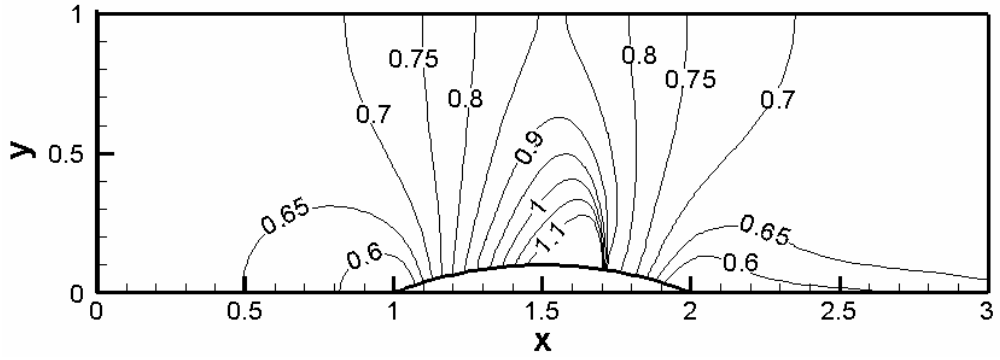


Figure 5.74: Mach contours in the channel having a circular bump at $M_\infty = 0.675$ $\alpha = 0^\circ$ obtained by Roe's flux difference splitting scheme using first-order reconstruction

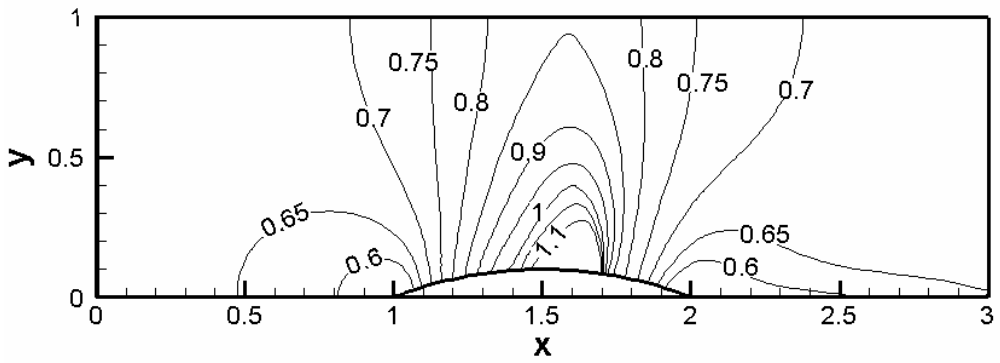


Figure 5.75: Mach contours in the channel having a circular bump at $M_\infty = 0.675$ $\alpha = 0^\circ$ obtained by AUSM using first-order reconstruction

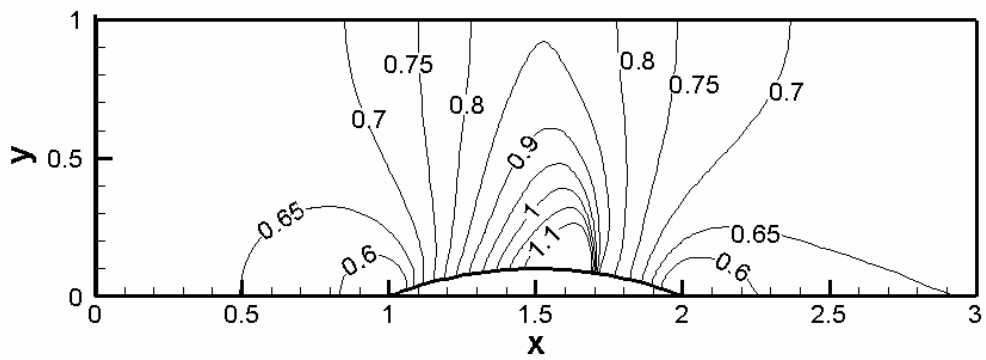


Figure 5.76: Mach contours in the channel having a circular bump at $M_\infty = 0.675$ $\alpha = 0^\circ$ obtained by AUFS using first-order reconstruction

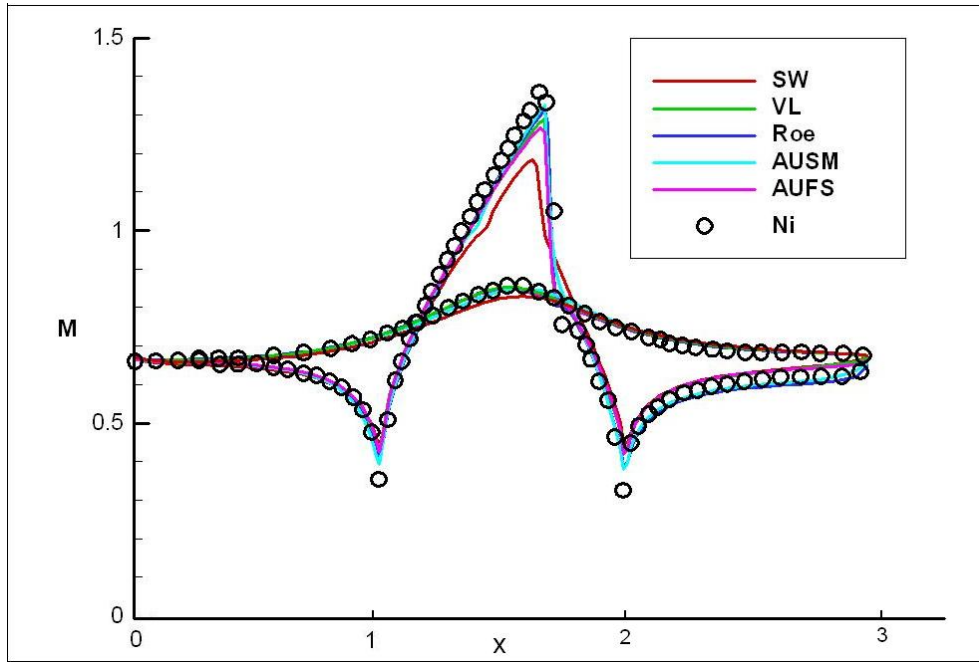


Figure 5.77: Distribution of Mach number in the channel having a circular bump at $M_\infty = 0.675$ $\alpha = 0^\circ$ using first-order reconstruction

5.2.1.3 Supersonic Flow

Flow with an inlet Mach number of $M_\infty = 1.4$ is tested in a 4% thick circular arc in the channel for the supersonic flow case. The flow is characterized by two oblique shock waves at the leading and trailing edges of the bump. The Mach contours shown for each flux splitting method separately in Figures 5.79 to 5.83 are compared with the Mach contours presented by Ni [60], shown in Figure 5.78. On top of this, Figure 5.84 shows the comparison of the distribution of Mach number in the flow field. Mach number upstream of the first oblique shock wave is the inlet Mach number of 1.4 for all schemes. Steger-Warming flux vector splitting scheme gives accurate results in the case of oblique shock waves, although the scheme is not accurate in capturing the normal shock waves. AUSM yields the most accurate results, whereas the other schemes give comparable accuracy.

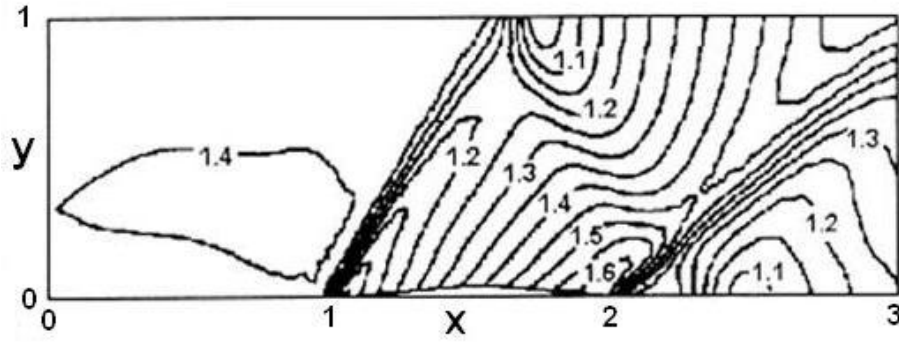


Figure 5.78: Mach contours in the channel having a circular bump at $M_\infty = 1.4$ $\alpha = 0^\circ$ by Ni [60]

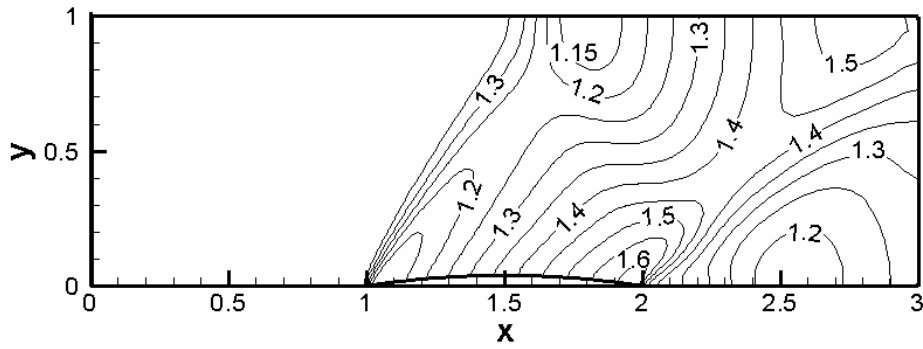


Figure 5.79: Mach contours in the channel having a circular bump at $M_\infty = 1.4$ $\alpha = 0^\circ$ obtained by Steger-Warming flux vector splitting scheme using first-order reconstruction

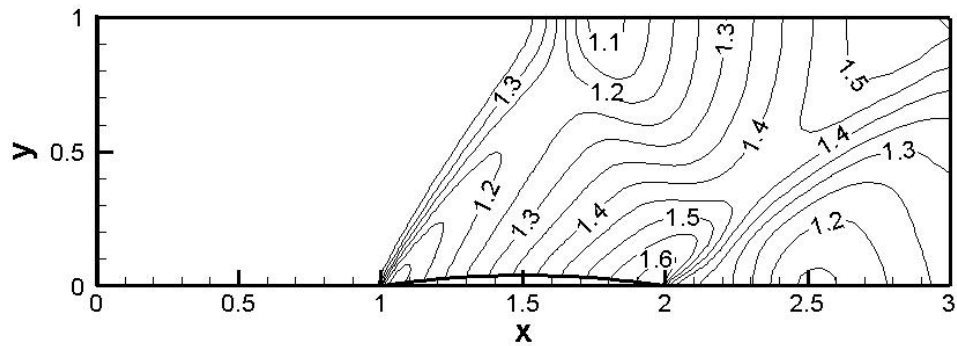


Figure 5.80: Mach contours in the channel having a circular bump at $M_\infty = 1.4$ $\alpha = 0^\circ$ obtained by Van Leer flux vector splitting scheme using first-order reconstruction

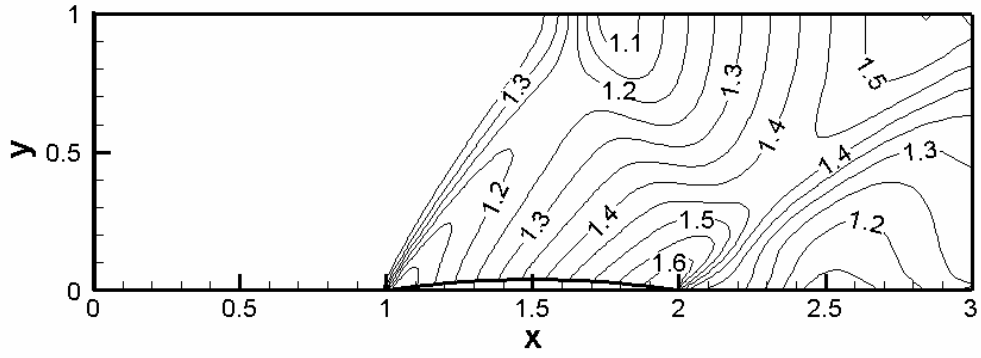


Figure 5.81: Mach contours in the channel having a circular bump at $M_\infty = 1.4$ $\alpha = 0^\circ$ obtained by Roe's flux difference splitting scheme using first-order reconstruction

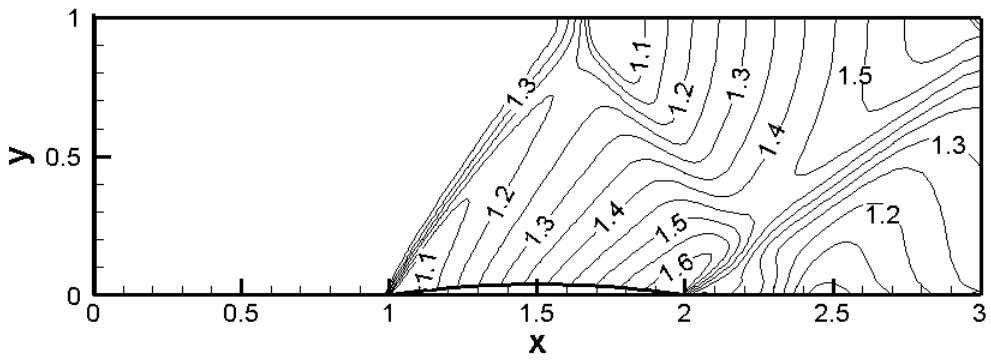


Figure 5.82: Mach contours in the channel having a circular bump at $M_\infty = 1.4$ $\alpha = 0^\circ$ obtained by AUSM using first-order reconstruction

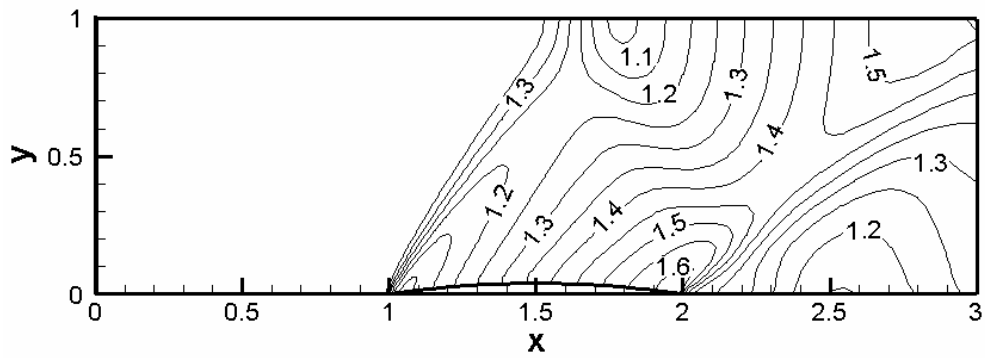


Figure 5.83: Mach contours in the channel having a circular bump at $M_\infty = 1.4$ $\alpha = 0^\circ$ obtained by AUFS using first-order reconstruction

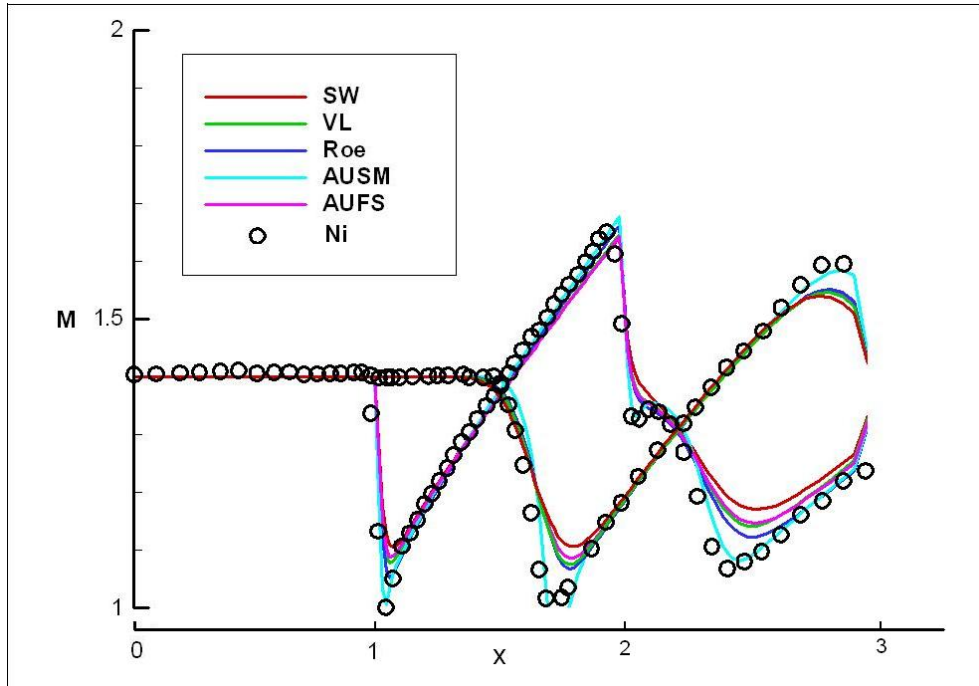


Figure 5.84: Distribution of Mach number in the channel having a circular bump at $M_\infty = 1.4 \alpha = 0^\circ$ using first-order reconstruction

5.2.2 Second-order Calculations

5.2.2.1 Second-order calculations without a limiter function

5.2.2.1.1 Subsonic Flow

The inflow Mach number is given as $M_\infty = 0.5$, where the theoretical solution gives a subsonic, symmetric solution about the bump, as stated in subsection 5.2.1.1. Figure 5.85 presents a complete comparison for the distribution of Mach number in the computational domain in comparison with Ni's result. It can be concluded from the figure that, Roe's flux difference splitting scheme and AUSM leads to the most accurate results as in the first-order case. The results obtained by the other schemes, Steger-Warming and Van Leer flux vector splitting schemes and AUFS, does not yield to symmetric results around the bump which is the indication of accuracy. Although the results are not symmetric they can be accepted. Using second-order reconstruction methods does not increase the accuracy in this internal flow subsonic test case. Mach contours are not shown

since the results are very similar to the ones obtained in the first-order case.

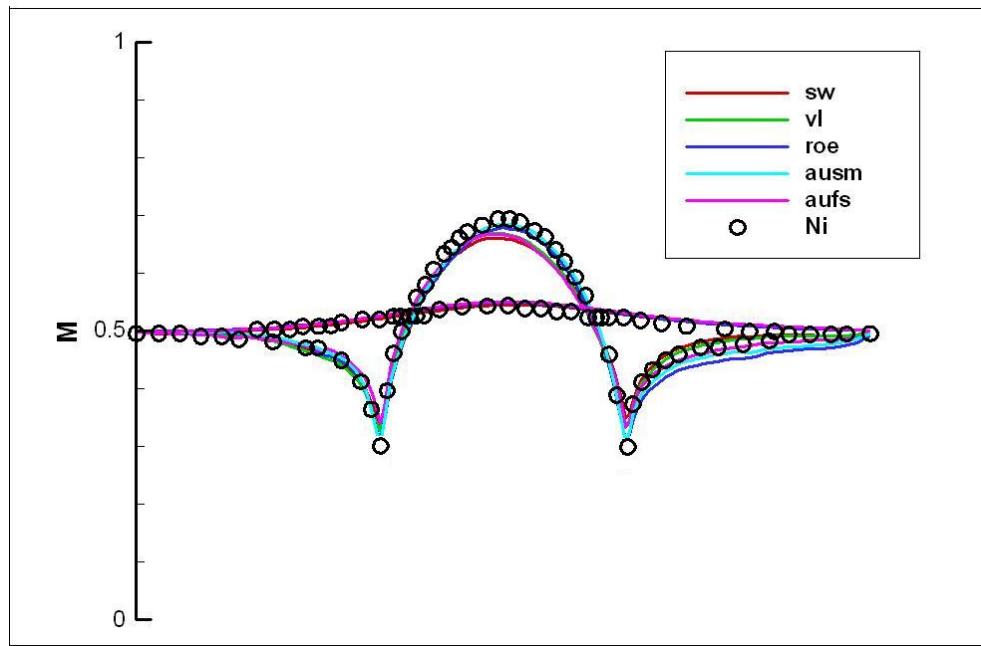


Figure 5.85: Distribution of Mach number in the channel having a circular bump at $M_\infty = 0.5$ $\alpha = 0^\circ$ obtained using second-order reconstruction without a limiter function

5.2.2.1.2 Transonic Flow

The inflow Mach number is given as $M_\infty = 0.675$, where the theoretical solution to transonic flow with a shock located at a 72% of the bump chord, as stated in subsection 5.2.1.2. Figure 5.86 presents a complete comparison for the distribution of Mach number in the computational domain in comparison with Ni's result. It can be concluded from the figure that, schemes other than Steger-Warming flux vector splitting lead to accurate results. Although an increase in accuracy was expected, Steger-Warming flux vector splitting scheme does not give accurate results as in the case of first-order reconstruction. All the other schemes in consideration capture the shock very accurately. The occurrence of oscillations is only encountered in the case of AUFS and Roe's flux difference splitting schemes. They can be damped by using limiters. Mach contours are not shown since the results are very similar to the ones obtained in the first-order

case.

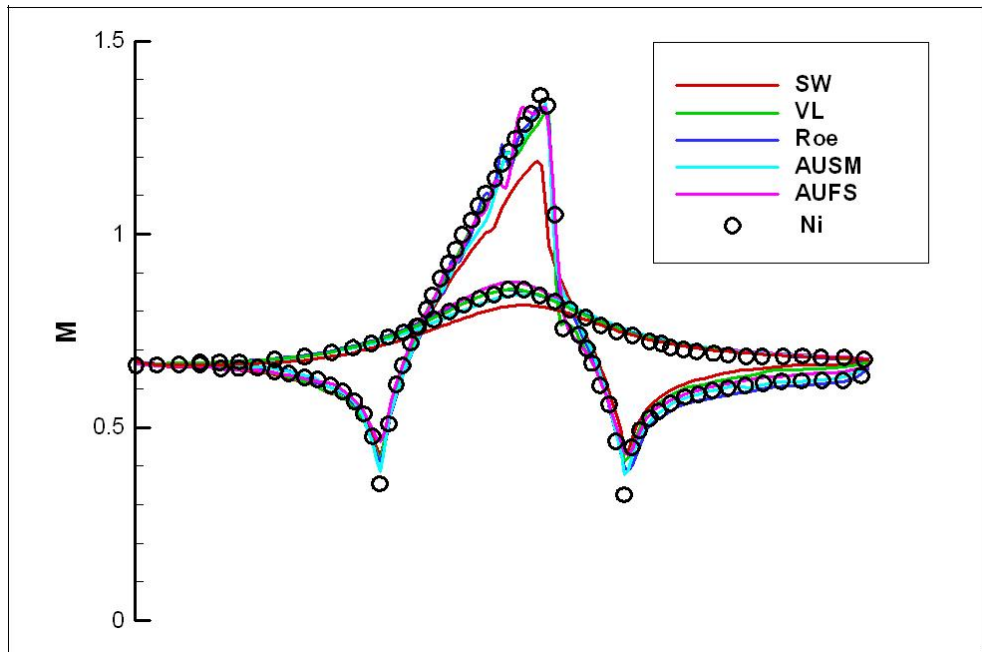


Figure 5.86: Distribution of Mach number in the channel having a circular bump at $M_\infty = 0.675$ $\alpha = 0^\circ$ obtained using second-order reconstruction without a limiter function

5.2.2.1.3 Supersonic Flow

Flow with an inlet Mach number of $M_\infty = 1.4$ is tested in a 4% thick circular arc in the channel for the supersonic flow case. The flow is characterized by two oblique shock waves at the leading and trailing edges of the bump. Figure 5.87 presents a complete comparison for the distribution of Mach number in the computational domain in comparison with Ni's result. AUFS does not give any results and leads to spurious oscillations. None of the other schemes could capture the oblique shock waves, accurately. As clearly seen from the figure, Mach number at the leading and trailing edges of the bump cannot be obtained. All the schemes lead to oscillatory results. Use of limiters is compulsory when second-order reconstruction methods are used. Although, the obtained results are not accurate and oscillatory, AUSM leads to the best results among all.

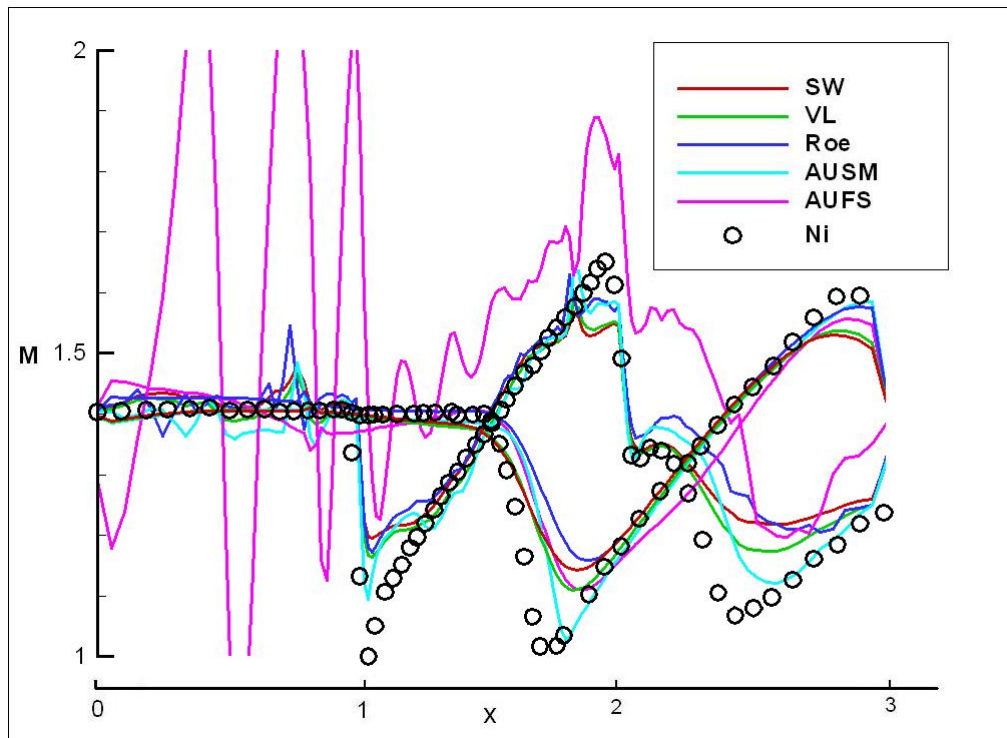


Figure 5.87: Distribution of Mach number in the channel having a circular bump at $M_\infty = 1.4$ $\alpha = 0^\circ$ obtained using second-order reconstruction without a limiter function

5.2.2.2 Second-order calculations with a limiter function

5.2.2.2.1 Subsonic Flow

The inflow Mach number is given as $M_\infty = 0.5$, where the theoretical solution gives a subsonic, symmetric solution about the bump, as stated in subsection 5.2.1.1. Figure 5.88 presents a complete comparison for the distribution of Mach number in the computational domain with Ni's result. As expected, and as seen in the external flow case, using limiter functions in the case of subsonic flows does not advance the solution, and there is no need to use one.

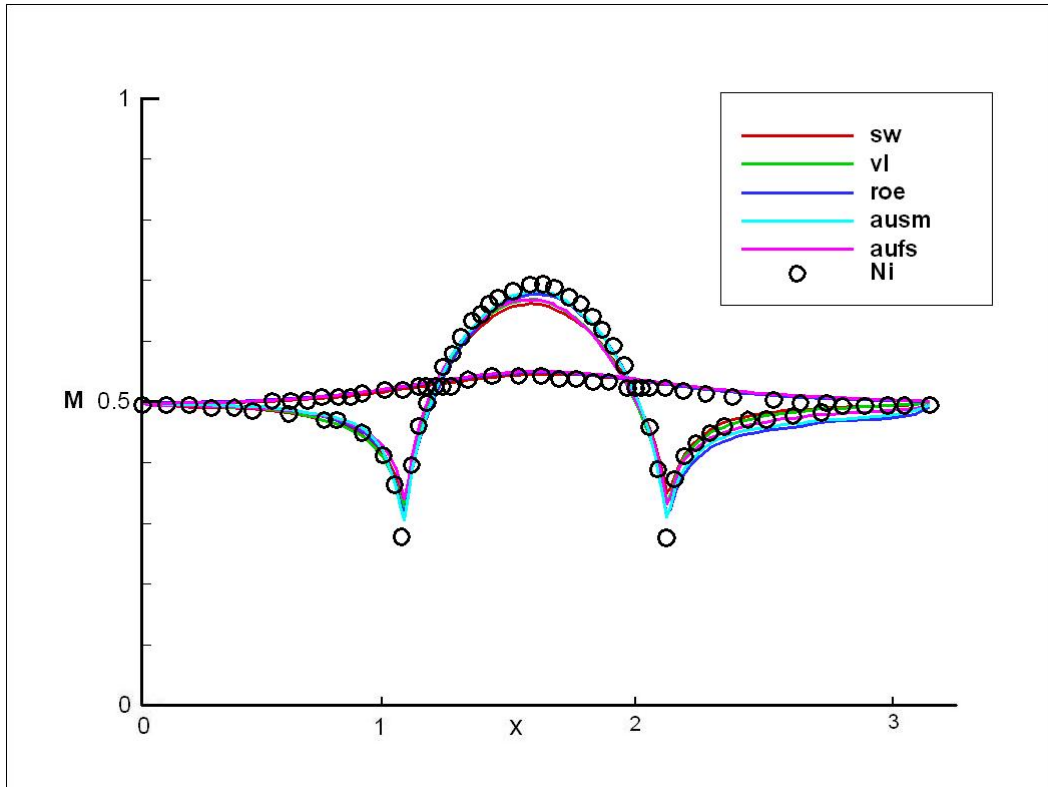


Figure 5.88: Distribution of Mach number in the channel having a circular bump at $M_\infty = 0.5$ $\alpha = 0^\circ$ obtained using second-order reconstruction with a limiter function

5.2.2.2.2 Transonic Flow

The inflow Mach number is given as $M_\infty = 0.675$, where the theoretical solution to transonic flow with a shock located at a 72% of the bump chord, as stated in subsection 5.2.1.2. Figure 5.89 presents a complete comparison for the distribution of Mach number in the computational domain with Ni's result. Figure 5.86 implies that AUFS and Roe's flux difference splitting schemes lead to oscillations in the vicinity of normal shock when second-order reconstruction is used. Limiter functions damp the oscillations in these schemes but there are still some spurious oscillations. Using a different type of limiter function may damp the oscillations fully. The results obtained by Steger-Warming flux vector splitting scheme are not advanced and they are not accurate. AUSM and Van Leer flux vector splitting schemes provides the most accurate results by defining the normal

shock wave sharply.

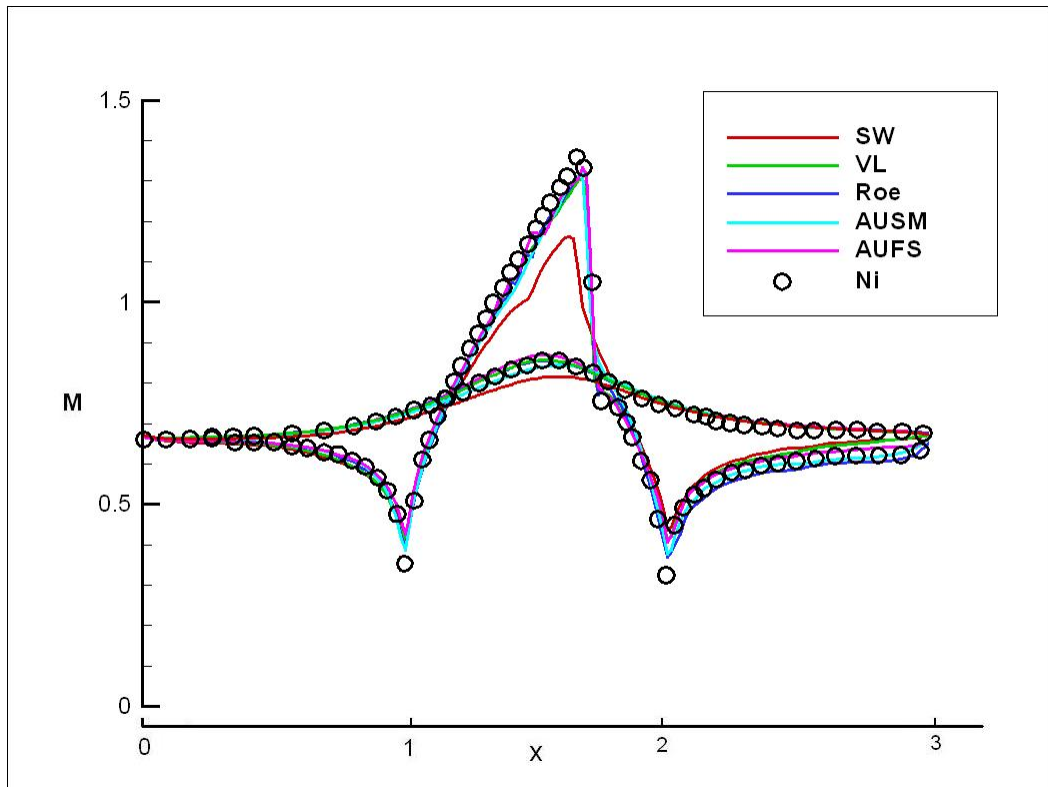


Figure 5.89: Distribution of Mach number in the channel having a circular bump at $M_\infty = 0.675$ $\alpha = 0^\circ$ obtained using second-order reconstruction with a limiter function

5.2.2.2.3 Supersonic Flow

Flow with an inlet Mach number of $M_\infty = 1.4$ is tested in a 4% thick circular arc in the channel for the supersonic flow case. The flow is characterized by two oblique shock waves at the leading and trailing edges of the bump. Figure 5.90 presents a complete comparison for the distribution of Mach number in the computational domain with Ni's result. Second-order supersonic flow calculations do not lead to any solutions when the limiter function is not used. Using a limiter function mostly damps the spurious oscillations but still they exist. The best results are obtained by using AUSM, but it also gives oscillatory results upstream the oblique shock at the leading edge of the bump. The results obtained by the other schemes can not

be accepted as accurate.

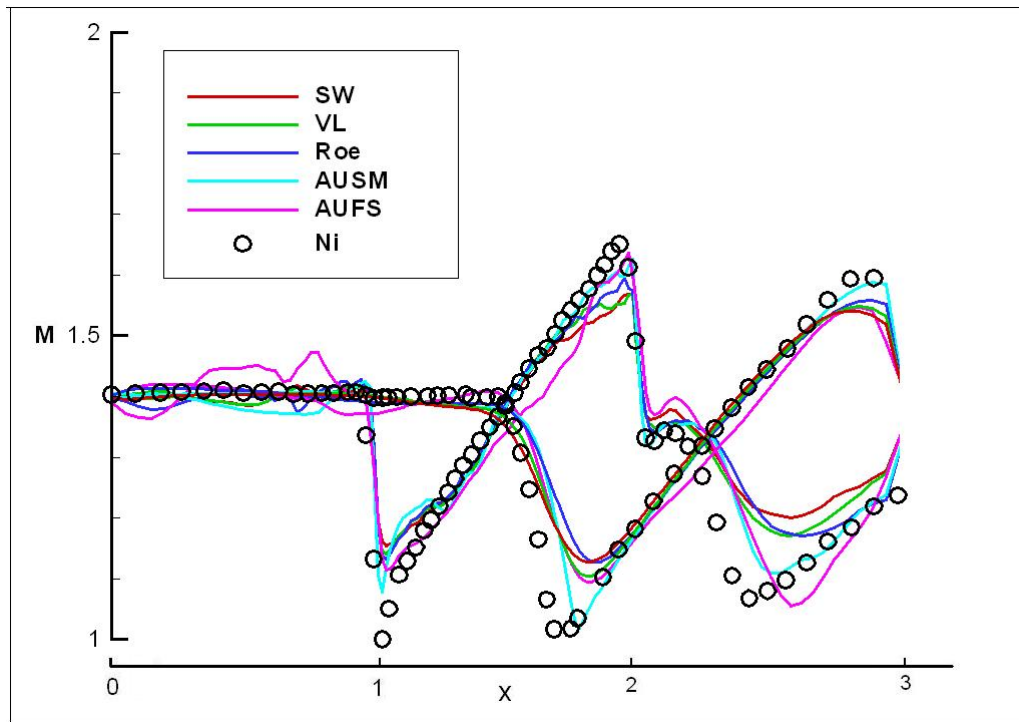


Figure 5.90: Distribution of Mach number in the channel having a circular bump at $M_\infty = 1.4$ $\alpha = 0^\circ$ obtained using second-order reconstruction with a limiter function

CHAPTER 6

CONCLUSION

In this study, a two-dimensional Euler solver is developed which is capable of handling both internal and external flows. Various upwind flux splitting methods are used in the finite volume discretisation of the governing equations. The analysis includes different types of flux splitting methods as well as the first- and second-order reconstruction schemes. Test calculations for the accuracy and efficiency of flux splitting schemes are performed by investigating subsonic, transonic and supersonic flows over NACA0012 airfoil and in channel having a circular arc on the lower boundary.

Different grids are used in the tests in order to examine the relation between the grid and solution. It is concluded that the denseness of the grid has an effect on the result until a sufficiently dense grid is obtained. Once the grid density is sufficient enough for accurate and efficient results to be obtained, using finer grids does not lead to more accurate results and it increases the convergence time.

Comparing the flux splitting methods presented in the study, it can be concluded that the Advection Upstream Splitting Scheme (AUSM) serves the most accurate and efficient results both in external and internal flows, no matter what the order of reconstruction and the freestream Mach number is. Roe's flux difference splitting scheme also leads to accurate and efficient results. However, when second-order reconstruction is used the solution oscillates in the vicinity of discontinuities. Moreover, supersonic flow solutions for external flows show that the scheme pollutes the region upstream of the bow shock. More accurate solutions are obtained when limiters are used. Although Artificially Upstream Flux Splitting (AUFS) scheme gives accurate results when the first-order

reconstruction is concerned, the second-order reconstruction does not give satisfactory results. Van

Leer flux vector splitting scheme gives as accurate results as AUFS scheme does in the first-order calculations. On the other hand, the second-order results of Van Leer flux vector splitting scheme are more accurate than the second-order results of AUFS and are comparable with the ones obtained by AUSM. Although Steger-Warming flux vector splitting scheme does not provide accurate results in the first-order calculations, the second-order results for external flows are comparable with AUSM like Van Leer flux vector splitting scheme. But the results obtained for second-order internal flows with Steger-Warming flux vector splitting scheme are not accurate. Results obtained with transonic and supersonic speeds for internal flows show that, internal flows require characteristic boundary conditions.

Limiters should not be used in subsonic flows, since they do not have an effect on the solution when there is no high gradient region in the flow field. It is known that limiters should be used for transonic and supersonic flows, both for internal and external flows. However, as long as the test results are concerned, it can be concluded that Steger-Warming and Van Leer flux vector splitting schemes do not require limiters in external flows for the cases considered. AUSM provide acceptable results for external flows, and transonic internal flows. Limiters should be used for more accurate results. Roe's flux difference splitting scheme require limiters for transonic and supersonic speeds in both internal and external flows.

As far as the convergence times are concerned, AUSM gives the fastest convergence, AUFS and Roe's flux difference splitting schemes follow AUSM and the flux vector splitting schemes converge more slowly. Convergence time can be decreased by the use of characteristic boundary conditions in external flow calculations, since the farfield boundary will be closer to the airfoil.

Further studies based on this study should include implementation of different flux splitting schemes, higher-order reconstruction schemes, and different types of limiters.

REFERENCES

- [1] Versteeg, H.K., Malalasekera W., "An Introduction to Computational Fluid Dynamics - The Finite Volume Method", Longman, 1995

- [2] Hoffmann, K. A., Chiang, S. T., "Computational Fluid Dynamics", Engineering Education System, 2000

- [3] Hirsch, C., "Numerical Computation of Internal and External Flows", John Wiley & Sons, 1988

- [4] Ferziger, J.H., Perić, M., "Computational Methods for Fluid Dynamics", Springer, 1996

- [5] Tannehill, J. C., Anderson, D. A., Pletcher, R. H., "Computational Fluid Mechanics and Heat Transfer", Taylor & Francis, 1997

- [6] Blazek, J., "Computational Fluid Dynamics: Principles and Applications", Elsevier, 2001

- [7] Jameson, A., Schmidt, W., and Turkel, E., "Numerical Solution of the Euler Equations by Finite-Volume Methods Using Runge-Kutta Time-Stepping Schemes", AIAA-81-1259, 1981

- [8] Swanson, R. C., Turkel, E., "On central-difference and upwind schemes", Journal of Computational Physics, vol. 101, pp. 292-306, 1992

- [9] Lax, P. D., "Weak solutions of nonlinear hyperbolic equations and their numerical computation", Comm. Pure Appl. Math., vol. 7, pp. 159-93.

- [10] Lax, P. D., and Wendroff, B., "Systems of Conservation Laws", Comm.

Pure and Applied Mathematics, vol. 13, pp. 217-37, 1960

[11] MacCormack, R. W., "The effect of viscosity in hypervelocity impact cratering", AIAA-66-354, 1966

[12] Lerat, A., "Numerical shock structure and nonlinear corrections for difference schemes in conservation form", Lecture Notes in Physics, vol. 20, pp. 345-351, New York: Springer-Verlag.

[13] Lerat, A., "Implicit Methods of Second Order Accuracy for the Euler Equations", AIAA-83-1925, AIAA 6th Computational Fluid Dynamics Conference; also AIAA Journal, vol. 23, pp. 33-40, 1983

[14] Beam, R. M., and Warming, R. F., "An Implicit Finite-Difference Algorithm for Hyperbolic System in Conservation Law Form", Journal of Computational Physics, vol. 22, pp. 87-109, 1976

[15] Chung, T.J., "Computational Fluid Dynamics", Cambridge University Press

[16] Jameson, A., "Artificial Diffusion, Upwind Biasing, Limiters and their Effect on Accuracy and Multigrid Convergence in Transonic and Hypersonic Flow", AIAA-93-3559, 1993

[17] Steger, J. L., Warming, R. F., "Flux Vector Splitting of the Inviscid Gas Dynamics Equations with Application to Finite-difference Methods", Journal of Computational Physics, vol. 40, pp. 263-293, 1981

[18] Toro, E.F., "Riemann Solvers and Numerical Methods for Fluid Dynamics", Springer, 1999

[19] Laney, C. B., "Computational Gas Dynamics", Cambridge University Press, 1998

[20] Anderson, W. K., and Thomas, J. L., Van Leer, B., "Comparison of Finite Volume Flux Vector Splittings for the Euler Equations", AIAA, vol.24, no.9, pp.

1453-1460, 1986

[21] Van Leer, B.: "Flux- Vector Splitting for the Euler Equations", Proc. 8th Int. Conf. on Numerical Methods in Fluid Dynamics, Springer Verlag, pp. 507-512; also ICASE Report 82-30, 1982.

[22] Liou, M. S., Steffen, C. J., "A New Flux Splitting Scheme", Journal of Computational Physics, vol. 107, pp. 23-29, 1993

[23] Liou, M. S., "A Continuing Search for a Near-Perfect Numerical Flux Scheme Part I: AUSM+", NASA-TM-106524

[24] Liou, M. S., Wada, "A Flux Splitting Scheme with High-resolution and Robustness for Discontinuities", AIAA-94-0083, SIAM J. SCI. COMPUT., vol. 18, No. 3, pp. 633-657, 1997

[25] Liou, M., "A Sequel to AUSM, Part II: AUSM+-up for all speeds", unpublished paper

[26] Kim, K. H., Kim, C., Rho, O., "Methods for the Accurate Computations of Hypersonic Flows I. AUSMPW+ Scheme", Journal of Computational Physics, vol. 174, pp. 38-80, 2001

[27] Kim, K. H., Kim, C., "Accurate, efficient and monotonic numerical methods for multi-dimensional compressible flows Part I: Spatial discretisation", Journal of Computational Physics, vol. 208, pp. 527-569, 2005

[28] Liou, M., "Ten Years in the Making- AUSM-family", AIAA-2001-2521

[29] Jameson, A., "Analysis and Design of Numerical Schemes for Gas Dynamics II: Artificial Diffusion and Discrete Shock Structure", Int. J. Computational Fluid Dynamics, vol. 5, pp. 1-38, 1995

[30] Zha, G., "A Low Diffusion E-CUSP Upwind Scheme for Transonic Flows", AIAA-2004-2707

- [31] Swanson, R. C., Radespiel, R., Turkel, E., "Comparison of Several Dissipation Algorithms for Central Difference Schemes", ICASE Report No. 97-40, 1997.
- [32] Sun, M., Takayama, K., "An artificially upstream flux vector splitting scheme for the Euler equations", *Journal of Computational Physics*, vol. 189, pp. 305-329, 2003
- [33] Rossow, C. C., "A Simple Flux-Vector Splitting Scheme for Compressible Flows", *Contributions to the 11th STAB/DGLR Symposium Berlin 1998*, in *Notes on Numerical Fluid Mechanics*, Vol. 72, Vieweg Publishers, Braunschweig/Wiesbaden, 1999
- [34] Rossow, C. C., "A Flux-Splitting Scheme for Compressible and Incompressible Flows", *Journal of Computational Physics*, vol. 164, pp. 104–122, 2000
- [35] Vinokur, M., "Generalized Flux-Vector Splitting and Roe Average for an equilibrium Real Gas", *Journal of Computational Physics*, vol. 89, pp. 276-300, 1990
- [36] Liou, M.-S., Van Leer, B., Shuen, J.-S., "Splitting of Inviscid Fluxes for Real Gases", *Journal of Computational Physics*, vol. 87, pp. 1-24, 1990
- [37] Godunov, S.K., "A Difference Scheme for Numerical Computation Discontinuous Solution of Hydrodynamic Equations", *Math. Sbornik (in Russian)*, 47 (1959), pp. 271-306; translated US Joint Publ. Res. Service, JPRS 7226, 1969.
- [38] Roe, P.L., "Approximate Riemann Solvers, Parameter Vectors, and Difference Schemes", *Journal of Computational Physics*, vol. 43, pp. 357-372, 1981
- [39] Osher, S.; Solomon, F., "Upwind Difference Schemes for Hyperbolic Systems of Conservation Laws", *Math. Comp.*, vol. 38, pp. 339-374, 1982
- [40] Dick, E., "A Flux-Difference Splitting Method for Steady Euler Equations",

Journal of Computational Physics, vol. 76, pp. 19-32, 1988

[41] Lombard, C. K., Olinger, J., Yang, J. Y., "Multi-Dimensional Formulation of CSCM an Upwind Flux Difference Eigenvector Split Method for the Compressible Navier-Stokes equations", AIAA 83-1895, 1983

[42] Collins, J. P., Colella, P., Glaz, H. M., "An Implicit-Explicit Godunov Scheme for Compressible Flow", Journal of Computational Physics, vol. 116, pp. 195-211, 1995

[43] Wesseling P., "Principles of Computational Fluid Dynamics", Springer, 2000

[44] Sidilkover, D., "A Genuinely Multidimensional Upwind Scheme and an Efficient Multigrid for the Compressible Euler Equations", ICASE Report 94-84, 1994

[45] Mesaros, L. M., "Multidimensional Fluctuation Splitting Schemes for the Euler Equations on Unstructured Grids", Phd. Thesis, University of Michigan, 1995

[46] Van Leer, B., "Towards the Ultimate Conservative Difference Scheme V. A Second Order Sequel to Godunov's Method", Journal of Computational Physics, vol. 32, pp. 101-136, 1979

[47] Hosseini, R., Rahimian, M.H., Mirzaei, M., "Performance of High-Accuracy Schemes in Inviscid Fluxes Calculation", unpublished paper, Mechanical Eng. Department, University of Tehran

[48] Hubbard, M. E., "Multidimensional Slope Limiters for MUSCL-Type Finite Volume Schemes on Unstructured Grids", Journal of Computational Physics, vol. 155, pp. 54-74, 1999

[49] Aftosmis, M., Datta, G., Tavares, T.S., "Behavior of Linear Reconstruction Techniques on Unstructured Grids", AIAA Journal, vol. 33, no. 11, 2038-2049, 1995

- [50] Chan, K. I., Ng, E.Y.K., "Higher-order Upwind Distribution Formula Scheme for Structured and Unstructured Adaptive Flow Solvers", International Journal of Computational Fluid Dynamics, vol. 17(1), pp. 61-73, 2003
- [51] Burg, O.E., "Higher Order Variable Extrapolation for Unstructured Finite Volume RANS Flow Solvers", AIAA-2005-4999
- [52] Rezgui, A., Cinella, P., Lerat, A., "Third-order Accurate Finite Volume Schemes for Euler Computations on Curvilinear Meshes", Computers & Fluids, vol. 30, pp. 875-901, 2001
- [53] Mavriplis, D.J., "Revisiting the Least-squares Procedure for Gradient Reconstruction on Unstructured Meshes", NASA/CR-2003-212683
- [54] Barth, T.J., Jespersen, D.C., "The Design and Application of Upwind Schemes on Unstructured Meshes", AIAA-89-0366, 1989
- [55] Barth, T.J., Frederickson, P.O., "Higher Order Solution of the Euler Equations on Unstructured Grids using Quadratic Reconstruction", AIAA-90-0013, 1990
- [56] Berger, M., Aftosmis, M., "Analysis of Slope Limiters on Irregular Grids", NAS-05-007
- [57] De Zeeuw D., and Powell K. G., "An Adaptive Cartesian Mesh Method for the Euler Equations", Journal of Computational Physics, vol.104, pp. 56-68, 1993
- [58] Şişman, T. Ç., "Parallel Processing of Three-Dimensional Navier-Stokes Equations for Compressible Flows", M. Sc. thesis, Mechanical Engineering Department, METU, 2005
- [59] Aksel, M. H., "Notes on Computational Fluid Dynamics and 2D Euler", Department of Mechanical Engineering, METU, 2004
- [60] Ni, R. H., "A Multiple-Grid Scheme for Solving the Euler Equations", AIAA

Journal, Vol. 20, pp. 1565-1571, 1982

[61] Özdemir, E. D., "Implementation of Rotation into a 2-D Euler Solver", M. Sc. thesis, Mechanical Engineering Department, METU, 2005

[62] Aksel, M. H., Eralp, O. C., "Gas Dynamics", Prentice Hall, 1997

[63] Rohde, A., "Eigenvalues and Eigenvectors of the Euler Equations in General Geometries", AIAA-2001-2609

[64] Sezal, İ. H., "Development of a Two Dimensional Euler Solver for Unstructured Grids", M. Sc. thesis, Mechanical Engineering Department, METU, 2001

[65] Amick, J. L., "Comparison of the Experimental Pressure Distribution on an NACA 0012 Profile at high Speeds with that calculated by the relaxation method", National Advisory Committee for Aeronautics, Technical note 2174, 1950

[66] Wu, Z. N., Li, K., "Anisotropic Cartesian grid method for steady inviscid shocked flow computation", International Journal for Numerical Methods in Fluids, vol. 41, pp. 1053-1084, 2003

APPENDIX A

CALCULATION OF RESIDUALS

The variables that have time dependency are expressed as residual terms. In order to reach an acceptable solution, convergence criteria should be employed. The ratio of the n^{th} residual term to the 1st term is the basis of the convergence criteria. The criteria are defined as follows: [61]

$$R_1^n = \frac{\sqrt{\sum_{\substack{I=1 \\ J=1}}^{I=NX-1 \\ J=NY-1}} [R^n(I, J, 1)]^2}{(NX-1)(NY-1)} \quad (\text{A.1})$$

$$R_2^n = \frac{\sqrt{\sum_{\substack{I=1 \\ J=1}}^{I=NX-1 \\ J=NY-1}} [R^n(I, J, 2)]^2}{(NX-1)(NY-1)} \quad (\text{A.2})$$

$$R_3^n = \frac{\sqrt{\sum_{\substack{I=1 \\ J=1}}^{I=NX-1 \\ J=NY-1}} [R^n(I, J, 3)]^2}{(NX-1)(NY-1)} \quad (\text{A.3})$$

$$R_4^n = \frac{\sqrt{\sum_{\substack{I=1 \\ J=1}}^{I=NX-1 \\ J=NY-1}} [R^n(I, J, 4)]^2}{(NX-1)(NY-1)} \quad (\text{A.4})$$

In above equations, R_1 represents the residual for the mass conservation. R_2 and R_3 represent x - and y -momentum conservations residuals, respectively. The last equation for R_4 corresponds to the residual for energy conservation.

Then, the ratios of the above residuals are given in log-scale as: [61]

$$RR_1 = \log\left(\frac{R_1^n}{R_1^1}\right) \quad (\text{A.5})$$

$$RR_2 = \log\left(\frac{R_2^n}{R_2^1}\right) \quad (\text{A.6})$$

$$RR_3 = \log\left(\frac{R_3^n}{R_3^1}\right) \quad (\text{A.7})$$

$$RR_4 = \log\left(\frac{R_4^n}{R_4^1}\right) \quad (\text{A.8})$$

In above equations, when the obtained values are smaller than the specified convergence criteria, solution is accepted to converge.